HEAVY ION-INDUCED SINGLE PARTICLE DISPLACEMENT DAMAGE IN SILICON

By

Elizabeth C. Auden

Dissertation

Submitted to the Faculty of the

Graduate School of Vanderbilt University

in partial fulfillment of the requirements

for the degree of

DOCTOR OF PHILOSOPHY

in

ELECTRICAL ENGINEERING

December, 2013

Nashville, Tennessee

Approved:

Professor Robert A. Weller

Professor Marcus H. Mendenhall

Professor Robert A. Reed

Professor Bridget R. Rogers

Professor Ronald D. Schrimpf

Dr. Joseph R. Srour

ACKNOWLEDGMENTS

I am grateful to my sponsors at NASA and the Defense Threat Reduction Agency for their financial support of my time at Vanderbilt.

I would like to thank my committee members for their insight and advice: Prof. Robert Weller, Prof. Ron Schrimpf, Prof. Marcus Mendenhall, Prof. Robert Reed, Dr. Joseph Srour, and Prof. Bridget Rogers. I would also like to thank faculty members of the Vanderbilt departments of Electrical Engineering & Computer Science and Physics for sharing their technical expertise with me. Prof. Dan Fleetwood and Prof. Soc Pantalides advised me on damage and defect formation in silicon. Prof. Tim Holman and Prof. Lloyd Massengill discussed the design and RC modeling of current-to-voltage converter ciruits with me, and Prof. Mitch Wilkes advised me on the appropriate use of median filters in data analysis. Finally, I would like to thank Mike McCurdy for his time on the Pelletron; Dr. Enxia Zhang for bonding devices; Phil Davis for guidance in the machine shop; Nick Hooten and Geoff Bennett for laser testing, TCAD tutorials, and looking at band diagrams; and Mike King for MRED collaboration.

Thanks to all the RER group students for the shared experience of graduate school, Mellow Mushroom pizza, and hot chicken at Hattie B's: Sarah, Stephanie, Cher, Farah, Karen, Geoff, Nick, Mike, Dave, Isaak, Jeff, and Zach.

Most of all, I would like to thank my family for their endless support: my husband Adam, my daughter Katie, my parents Annette and John White and Glenn and Linda Easterly, my aunt and uncle Lezette and Michael Thomason, and my grandparents Francis and Louise Armstrong and Tom Easterly. Thanks for all the child wrangling. Thanks to my cousin Anne Friedland for her poster design advice.

Finally, I would like to thank Prof. Mendenhall for sharing his mother's words of encouragement when measuring even a picoampere seemed like an impossible task: "There are no hard problems, only problems with many steps."

TABLE OF CONTENTS

LIST OF TABLES

LIST OF FIGURES

CHAPTER I

Introduction

Accumulated dipslacement damage is one of the long-term failure mechanisms to which satellite electronics are subjected in the harsh radiation environments of space. Satellite electronics are bombarded with energetic particles that displace atoms as they travel through materials, and permanent damage to the crystal lattice of semiconductors results in electrical degradation. The average amount of electrical damage per particle sustained by a device can be predicted from nonionizing energy deposition simulations for a given radiation environment. However, accurate prediction of the maximum amount of damage caused by a single particle has remained an outstanding problem of radiation effects since the complex relationship between phonons, lattice displacements and annealing has not yet been quantified in a model that links nonionizing energy deposition to stable, electrically active defects.

This work presents measurements and simulations of the electrical degradation in silicon diodes caused by damage from individual heavy ions. Low-current measurements of individual damage events provide insight into the relationship between atomic motion within an irradiated material and the electrically active defects that result. The relationship between nonionizing energy deposition and electrical degradation that immediately follows damage caused by individual ions can be understood with Shockley-Read-Hall (SRH) theory when electric field enhancement is taken into account. From an engineering standpoint, this result can be used to predict the maximum amount of electrical damage that a silicon device is likely to sustain from single particles in a given radiation environment.

Satellites encounter energetic particles that range from massless photons to the heavy nuclei elements of galactic cosmic rays (GCRs). The Van Allen belts surrounding the earth harbor populations of trapped protons and electrons [1]. Solar flares and coronal

mass ejections release transient populations of heavy ions, alpha particles, and high energy protons and electrons. While the likelihood of solar emissions increases and decreases with solar activity, the background population of GCRs is a constant threat. GCRs are heavy ions emitted by stellar processes. Energetic particles from the Van Allen belts, solar activity, and GCRs all increase the risk of accumulated radiation damage and transient electrical disruption in satellite electronics.

An incident particle loses energy to ionizing and nonionizing processes as it interacts with atoms in a target material. Ionizing energy deposition creates electron-hole pairs as an incident particle excites electrons from the valence band to the conduction band. Nonionizing energy is the fraction of incident energy lost to atomic displacements and phonon production [2]. Displacement damage is the resulting arrangement of stable defects in a semiconductor crystal lattice. A damage factor is defined as the average amount of electrical degradation per particle caused by displacement damage. For example, the particle damage factor may be calculated as the average increase in dark current density per incident particle [3], and the universal damage factor may be calculated as the average increase in thermal carrier generation per displacement damage dose deposited in a depletion region [4].

Damage factors can be calculated with nonionizing energy loss (NIEL). NIEL is a widely-used metric that represents the average amount of energy that an incident particle loses to atomic displacements [5]. Calculated values of NIEL, typically given in units of MeV-cm^2/g, are specific to the incident particle energy and species as well as the material and geometry of the target device. If the damage factor for one incident particle species and energy (e.g., 1 MeV neutrons) is known for a device, the damage factor for a second incident particle can be estimated from the ratio of NIEL values calculated for the two particles [6]. The appropriate use of NIEL can reduce the time and expense required for the beam testing during parts qualification.

While NIEL scales with the average amount of damage per particle, it does not indi-

cate the maximum amount of damage that a single particle can produce. Single particle displacement damage occurs when an individual particle creates a sufficient number of new defects to degrade or destroy a semiconductor device [7]. The maximum amount of electrical degradation caused by single particle displacement damage has been experimentally reported to be 20 to 30 times larger than the average amount of electrical degradation per particle [8], [9], [10]. The magnitude distribution of experimentally observed damage events does not match the magnitude distribution of the recoil spectrum calculated for silicon [8]. The difference between average damage event size and maximum event size introduces design problems in spaceflight electronics with low thresholds for acceptable leakage current, such as imaging sensors or low power electronics.

Pixels in charge-coupled devices (CCD), charge injection devices (CID) and active pixel sensors (APS) are the primary devices associated with single particle displacement damage in the literature since dark current, the current measured in a pixel in the absence of light, is a key electrical parameter sensitive to radiation-induced displacement damage [10], [11], [12]. For example, a CCD pixel may be expected to maintain its dark current below an acceptable threshold for a given operational lifetime based on the average increase in dark current per incident particle. A large damage event from a single particle could increase the pixel's dark current above this threshold, turning the device into a "hot pixel" well before the end of its anticipated operational lifetime. The dark current in a hot pixel is high enough that the pixel is always considered on, so that the imaging data for that pixel is corrupted.

Single particle displacement damage has also been reported in the literature for avalanche diodes [13], SDRAMs [14], HEMTs [15], and JFET diodes [16] exposed to radiation. A common feature of these devices is a vulnerability to increased leakage current when radiation particles create defects in reverse-biased depletion regions. Electric field enhancement has been suggested as a possible mechanism for large increases in pixel dark current when electric fields greater than or equal to 10^5 V/cm are present [9], [10], [12]. Defects op-

erating in fields of this magnitude exhibit field-enhanced emission resulting from reduced barriers to thermal carrier emission (the Poole-Frenkel effect) [17].

Chapter II presents the physics of atomic displacement, defect energy levels, and electric field-enhanced carrier generation necessary to calculate radiation-induced displacement damage from a single particle. A table of symbols used in Chapter II can be found in Appendix A. Chapter III demonstrates electrical degradation caused by single particle displacement damage with time series showing discrete, sustained increases in leakage current, or current steps, in ^{252}Cf-irradiated silicon JFET diodes. Chapter IV presents modeled distributions of current step magnitude that show good agreement with the magnitudes of current steps measured in irradiated JFET diodes. Radiation-induced defect density is obtained with Monte Carlo simulations of atomic displacements, and electric field effects are incorporated by modeling midgap defects as 1-D Coulomb potentials in the presence of electric field strengths obtained from TCAD simulations. The maximum magnitude of heavy ion-induced increases in current obtained from the expression for SRH generation are consistent with the largest current steps measured in ^{252}Cf-irradiated JFET diodes when electric field enhancement of defect emission rates, radiation-induced defect density, and the proximity of multiple depletion regions are taken into account.

CHAPTER II

Background

An incident particle traveling through a semiconductor material displaces lattice atoms through nonionizing processes such as Coulomb scattering, nuclear elastic collisions, and nuclear inelastic collisions [2]. Coulomb scattering occurs when a positively charged atomic nucleus is attracted or repelled by the charge of an incident particle. When an incident particle collides with an atomic nucleus, the combined kinetic energy of both particles is conserved during nuclear elastic collisions. Kinetic energy is not conserved in nuclear inelastic collisions that may involve the transfer of mass, such as fission or spallation. All three nonionizing processes are capable of displacing atoms from the semiconductor crystal lattice. The location from which a lattice atom has been displaced is a vacancy defect [18]. A displaced atom or collision by-product that comes to rest between lattice atoms is an interstitial defect, and isolated vacancy / interstitial pairs are called Frenkel defects or Frenkel pairs [18]. Fig. II.1 shows a cartoon of vacancy and silicon self-interstitial defect created by an incident particle [19].

Individual radiation particles that deposit less than 100 eV of non-ionizing energy typically result in Frenkel pairs [7]. When energetic particles deposit more than 100 eV of non-ionizing energy, a primary displaced atom (or primary knock-on atom, PKA) can dislodge secondary atoms as it travels through the material. Sufficiently energetic secondary displaced atoms can displace further atoms, resulting in a collection of point defects and defect clusters along the PKA's trajectory through the material. Vacancies and interstitials can form stable, electrically active defects by themselves or with doping and impurity atoms. For examples, two vacancies can form a stable divacancy defect [18], a vacancy and a phosophorus atom [20] or vacancy and arsenic atom [21] form the E-center defect [20], and a vacancy and an oxygen atom form the A-center defect [22]. As stable displacement

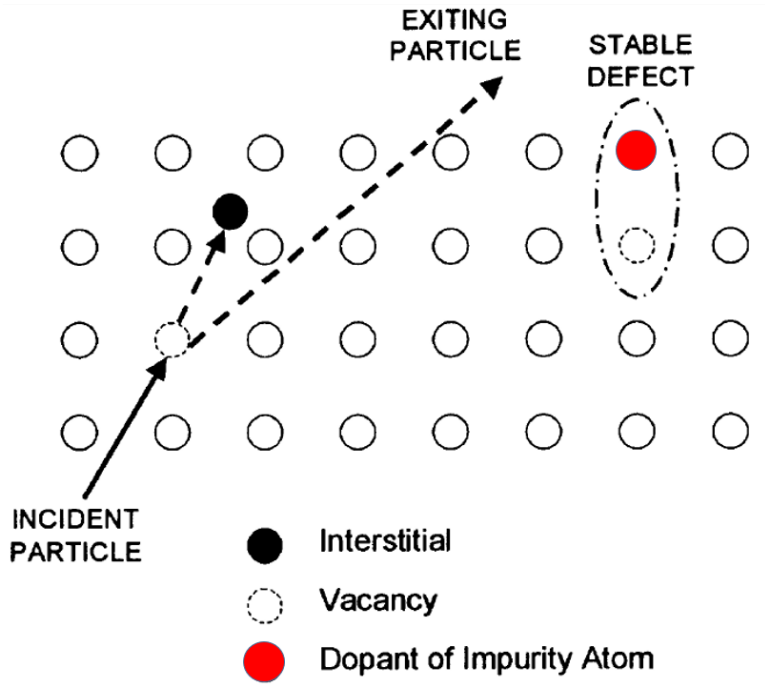

Figure II.1: Cartoon of a lattice vacancy and silicon self-interstitial defect caused by damage from an incident particle, after Marshall and Marshall, 1999.

defects accumulate, device performance suffers. Bipolar transistor gain, diode leakage current, and efficiency degradation in solar cells are device performance metrics adversely affected by increasing amounts of displacement damage [2].

For devices in which leakage current is a key parameter for device performance, such as imaging pixels and ultra-low leakage diodes, a single incident particle can create enough displacement damage to measurably degrade the device. Single particle displacement damage was first reported in the literature for avalanche diodes [13], but the phenomenon emerged as a concern for dark current in CCD and CID pixels in the 1980's [9], [10]. Burke and Summers noted that the largest observed damage events caused by single particles could not be explained with calculations of nuclear recoils [8]. Marshall *et al.* used extreme value statistics to satisfactorily predict the size distribution of damage events in the absence of high electric fields [23]. Srour and Hartmann identified electric field enhancement of defect emission rates as a possible explanantion for the difference in the ratio of the maximum observed damage size and the average observed damage size compared to the

ratio of the maximum calculated nuclear recoil energy and the average calculated nuclear recoil energy [9]. Bogaerts, Dierickx and Mertens were able to calculate the distribution of dark current increases for proton-irradiated APS pixels by applying electric field enhancement factors to distributions of elastic and inelastic nuclear recoils weighted by electric field [12].

As key device parameters shrink, single particle displacement damage will measurably degrade low power electronics and transistors with very small channel volumes. Non-silicon devices are also susceptible to single particle displacement damage; damage caused by individual heavy ions has been reported in AlGaN / GaN high electron mobility transistors (HEMTs) [15]. Section II.1 provides an overview of the devices reported for single particle displacement damage and the attempts to predict the maximum size of damage events, and Section II.2 describes the physics of reverse current contributed by radiation-induced defects with electric field-enhanced emission rates.

II.1 Devices Reported for Single Particle Displacement Damage

Avalanche Diodes

In 1965, Gereth *et al*. investigated the displacement damage induced by electrons and by individual neutrons in silicon avalanche diodes [13]. When an avalanche diode is biased in the breakdown region, a single carrier generated from a deep level defect causes an avalanche of electrons that can be measured as a voltage pulse. The pre-irradiation avalanche diodes exhibited pulse rates of less than 1 pulse per second. Pulse rates of post-irradiation diodes increased linearly with electron flux up to a flux of 10^{15} electrons cm^{-2} with a corresponding pulse rate of 1.3×10^{4} pulses/s. This linear increase was attributed to a constant rate which point defects were created with increasing flux. However, neutron irradiation resulted in a nonlinear increase in avalanche diode pulse rates, and this was attributed to the creation of defects clustered close enough together (within 100 Å) to enable tunneling between defect energy levels.

CCDs

In 1985, Srour and Hartmann demonstrated that CCD arrays sustained single particle displacement damage from 14 MeV neutrons [11]. The dark current of individual pixels increased by up to two orders of magnitude after single neutron strikes. The authors found that the largest increases in dark current were 20 times larger than the average dark current increase caused by a single damage event. This study recognized that individual radiation particles can increase dark current through the creation of midgap defects in device depletion region that give rise to thermal generation of carriers. Although the authors asserted in [11] that the magnitude of incremental increases in dark current depends on the number of new defects created rather than the arrangement of defects in clusters or as a set of isolated point defects, further investigation has shown that defect clustering strongly affects the magnitude of dark current increases [24], [25], [26].

In 1987 [8], Burke and Summers investigated the assumptions stated in [11] that the size of discrete amounts of electrical degradation, or damage events, scales linearly with the number of new defects while the arrangement of defects in clusters or as point defects is immaterial. These conditions imply that the damage distribution should be proportional to the nuclear recoil spectrum. The observed distribution of damage event sizes in [11] did not exhibit the same shape as the calculated nuclear recoil spectrum, nor did the ratio of maximum to average event sizes match the ratio of maximum to average nuclear recoil energy. The calculated maximum recoil size for neutrons interacting with silicon was 1.67 times the average nuclear recoil size, but the observed maximum damage event was 23 times larger than the average event size. In 1989, Srour and Hartmann suggested that electric field enhancement of defect emission rates could explain why the maximum to average damage event size observed in experimental data is higher than the ratio calculated from the nuclear recoil spectrum [9].

Charge Injection Device Imagers

In 1989, Marshall *et al.* used extreme value statistics to quantify the maximum dark

current increase resulting from damage events in proton-irradiated charge injection device (CID) imagers [10]. The authors reported that the average increase in dark current caused by individual particles scales with NIEL, but the magnitude of the largest individual increases does not scale with NIEL. A second conclusion was that the presence of an electric field higher than 10^5 Vcm^{-1} can result in larger increases in dark current than are predicted by SRH calculations when electric field effects are not taken into account. Electric field enhanced emission can stem from a large reverse bias or from device-specific geometry and metallization.

Active Pixel Sensors

In 2002, Bogaerts, Dierickx and Mertens presented a method for calculating the distribution of dark current increases observed in proton-irradiated active pixel sensors with high internal electric fields [12]. APS devices were irradiated with 10 MeV protons at fluences of 3×10^9 cm^2, 1×10^{10} cm^2, 3×10^{10} cm^2, 1×10^{11} cm^2 and 3×10^{11} cm^2. The reported damage factor of 3.65 nA cm^2 MeV^{-1} for these devices was calculated as the average increase in dark current per MeV of nonionizing energy deposited in the lattice. The size distribution of the measured increases in dark current observed in 1280×1024 pixels showed good agreement with a calculated distribution of dark current increases that incorporated electric field enhancement from both the Poole-Frenkel effect and multi-phonon tunneling. Following the methods described in [27] and [28], the authors used the distribution of electric field strengths present in the APS pixels to calculate a distribution of unitless enhancement factors as the ratio of thermal emission rates for a perfect midgap defect ($E_t = E_g/2$) in the presence of an electric field to zero-field emission rates [12]. The distribution of elastic and inelastic nuclear recoils was calculated for 10 MeV protons incident upon the APS pixels. This nuclear recoil distribution was applied to the damage factor and then weighted by enhancement factors corresponding to the distribution of electric fields present in the pixels.

SDRAMs

In 2008, Edmonds and Scheick provided an analysis of damage mechanisms in Hyundai 16×4 SDRAMs [14]. They concluded that micro-displacement damage, another term for single particle displacement damage, was the mechanism responsible for SDRAMs that failed to maintain their logic state between refresh intervals, a condition referred to as a "stuck bit." The SDRAMs were irradiated with protons at incident energies of 54 keV, 106 keV, and 203 keV as well as a range of heavy ion species and energies. Edmonds and Scheick proposed that micro-displacement damage events create generation centers in the reverse-biased depletion region shared by the transistor's drain and the capacitor inside the device. These generation centers emit thermally generated carriers that increase leakage current across the depletion region and discharge the SDRAM's capacitor. The number of stuck bits per incremental unit of fluence scaled with NIEL values calculated for the three proton energies in [14].

HEMTs

In 2011, Kuboyama *et al.* reported abrupt, single particle induced leakage current increases in AlGaN/GaN high electron mobility transistors (HEMTs) exposed to heavy ion radiation [15]. Drain and gate currents were monitored continuously as these devices were irradiated with 74 MeV neon, 147 MeV argon, 315 MeV krypton, and 443 MeV xenon as drain voltage was increased from 30 V to 150 V. During krypton irradiation, the authors observed several increases in drain leakage current that did not correspond to either an increase in drain voltage or to an increase in gate current. The average value of these abrupt increases in drain current was 187 μA. Following each abrupt increase, leakage current was observed to relax quickly to a stable value that was higher than the pre-increase level.

The abrupt increases in drain current reported for HEMTs are seven orders of magnitude higher than the discrete increases in leakage current for ^{252}Cf-irradiated JFET diodes described in Chapter III, but time series for the HEMT drain current and JFET diode reverse current show similar behavior. After each device incurs damage from an incident heavy ion strike, the initial abrupt increase in current relaxes (on the order of minutes) to a

stable value that is higher than the pre-strike leakage current.

II.2 Physics of Single Particle Displacement Damage

The silicon devices reported for single particle displacement damage share a common feature: device performance suffers when radiation-induced lattice damage increases the current flowing across a reverse-biased *pn*-junction. SRH theory describes the carrier recombination and generation processes that govern currents within device depletion regions [29], [30]. Device materials, depletion region geometry, defect characteristics, and electric field strength can be used to calculate the average frequency with which electrons and holes are generated and the average amount of time before they recombine. When carriers are generated more frequently than they recombine, the resulting current is referred to as leakage current, dark current, or reverse current. Reverse current is defined here as the leakage current measured in a reverse-biased diode [31].

Although there is a rich body of literature characterizing point defects, defect clusters, and defects that involve impurity atoms, this work concentrates on vacancy and interstitial defects. The average amount of electrical degradation per particle scales linearly with the average number of atomic displacements per particle [6]. Device damage factors can be predicted with NIEL values calculated from simulations of the vacancies and recoil atoms produced by incident ions [32], even though these vacancies and recoil atoms are mobile in the semiconductor and may anneal or form complex defect structures with silicon lattice defects or impurity atoms.

Although the amount of *stable* radiation-induced electrical degradation depends on both annealing time and temperature, the initial amount of electrical degradation observed immediately after an incident particle creates displacement damage can be understood with SRH generation. Just as simulations of the average number of vacancies and recoil atoms can be used to calculate NIEL values that predict the average amount of electrical degradation in a device, the size distribution of electrical degradation can be calculated by con-

sidering both the distribution of the number of vacancy and interstitial defects created by incident particles as well as the variation in thermal emission rates exhibited by these defects. The treatments of the effect of increased depletion region defect density on minority carrier lifetime and of electric field effects on generation lifetime are discussed in [33].

II.2.1 Shockley-Read-Hall Generation in Depletion Regions

SRH theory provides a statistical expression for the thermal recombination and generation of carriers subject to electron capture, electron emission, hole capture, and hole emission [29]. These four processes are illustrated in Fig. II.2. In indirect-gap materials, which are described by SRH theory, recombination occurs when a conduction band electron recombines with a valence band hole at the defect's energy level E_t. Generation processes cause the defect to emit electrons to the conduction band energy level E_c and holes to the valence band energy level E_v. In electron capture, a conduction band electron becomes trapped at the defect's energy level. Hole capture describes the emission of an electron trapped by the defect to the valence band, where the electron recombines with a hole. Electron emission occurs when an electron trapped by the defect is emitted to the conduction band, and hole emission occurs when the defect traps a valence band electron and creates a valence band hole. A semiconductor free from defects has no electron states located between the valence and conduction bands (the bandgap). The midway point between the valence and conduction bands is referred to as midgap.

Doping levels, bias conditions, defects, and temperature constrain the balance equation for recombination and generation processes. The SRH equation for the net recombination-generation rate U is

$$U = \frac{\sigma_n \sigma_p v_{th} N_t n_i}{\sigma_n e^{(E_t - E_i)/kT} + \sigma_p e^{(E_i - E_t)/kT}} \tag{II.1}$$

where σ_n is the capture cross-section for electrons (a measure of a defect's effectiveness at electron capture), σ_p is the capture cross-section for holes, v_{th} is the thermal velocity of electrons, N_t is the defect density, n_i is the intrinsic concentration of carriers in undoped

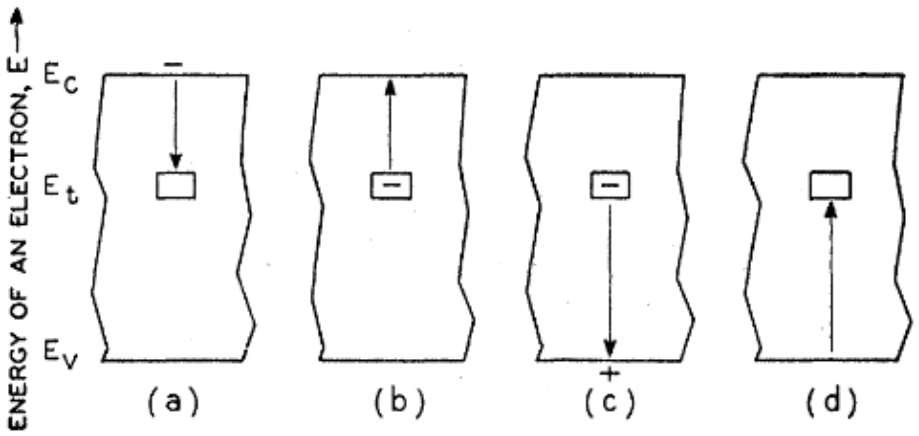

Figure II.2: Cartoon of electron capture, electron emission, hole capture, and hole emission, after Shockley and Read, 1952.

silicon, E_t is the defect's energy level, E_i is the intrinsic Fermi level, k is Boltzmann's constant, and T is temperature [34].

Defects with energy levels near the conduction band or valence band are considered to be shallow traps that primarily capture and emit either electrons or holes [34]. Deep level defects with energy levels near midgap are localized energy states called recombination-generation centers that are effective at the capture and emission of both electrons and holes. The proximity of a defect's energy level E_t to the intrinsic Fermi level E_i has an exponential effect on the defect's carrier generation rate. Fig. II.3 compares the recombination rate to the generation rate for different energy levels [34]. As a defect's energy level gets further from the intrinsic Fermi level and closer to the conduction or valence bands, the generation rate plummets while the recombination rate plateaus. Midgap defects are more effective at SRH generation than shallow traps.

The recombination generation rate U in II.1 is negative when the joint population of mobile electrons and holes np is less than ${n_i}^2$, the intrinsic carrier concentration of both electrons and holes in undoped silicon [29]. This condition occurs in the depletion region of a *pn*-junction that has been swept of its mobile carriers. The bias-dependent expression

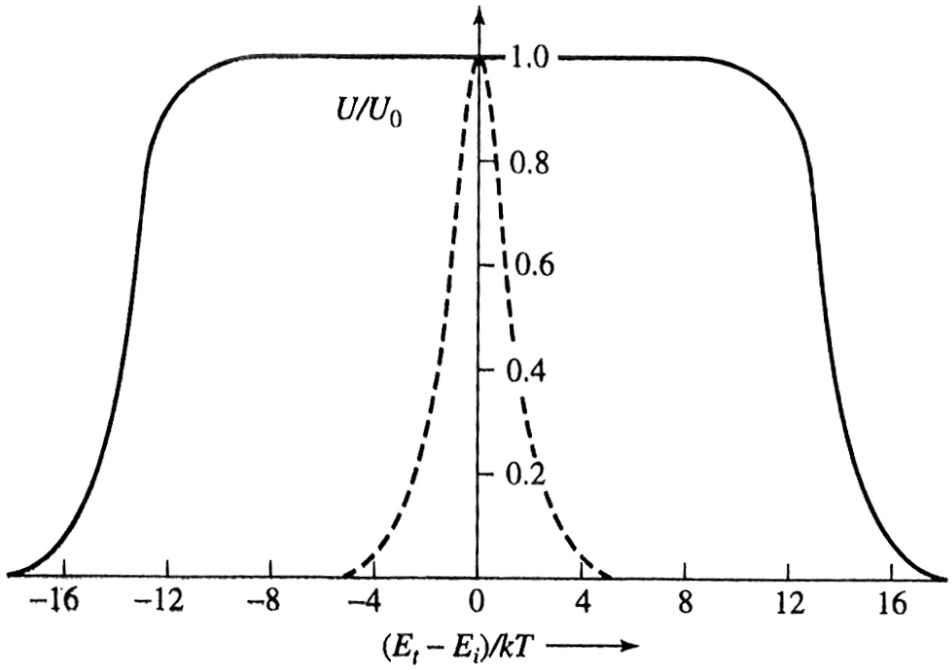

Figure II.3: Recombination and generation rates as a defect's energy level E_t moves away from intrinsic Fermi level E_i, after Muller, Kamins and Chan, 2003.

for the width of the depletion region x_d is

$$x_d = \left[\frac{2\varepsilon_{Si}}{q} \left(\frac{1}{N_A} + \frac{1}{N_D} \right) (\phi_i - V_a) \right]^{1/2} \tag{II.2}$$

where ε_{Si} is the permittivity of silicon, q is the charge of an electron, N_A is the acceptor doping level on the p-type side of the pn-junction, N_D is the donor doping level on the n-type side of the junction, and V_a is the voltage applied across the junction [34]. The built-in junction voltage ϕ_i is calculated in [34] as

$$\phi_i = \frac{kT}{q} ln \frac{N_A N_D}{{n_i}^2}. \tag{II.3}$$

The depletion region expands with the magnitude of applied reverse bias. The volume of the device that undergoes net thermal generation of carriers described by SRH theory can be calculated as the product of the junction area A and the depletion region width x_d.

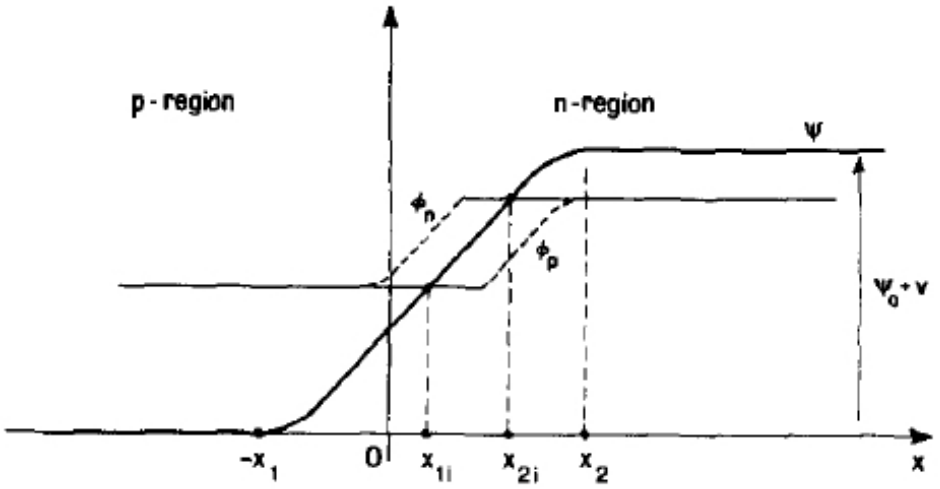

Figure II.4: The generation region width x_i and depletion region width x_d with respect to quasi-Fermi levels ϕ_n and ϕ_p and the electric potential Ψ, after Calzolari and Graffi, 1972.

In 1972, Calzolari and Graffi noted that the electron-hole pair emission rate exceeds the carrier capture rate when generation-recombination centers are located within a volume inside the depletion region called the generation region [35]. The generation region starts where the electric potential equals the hole quasi-Fermi level, and it ends where the electric potential equals the electron quasi-Fermi level as shown in Fig. II.4. Inside the generation region, the electron quasi-Fermi level is higher than the conduction band, and the hole quasi-Fermi level is lower than the valence band. The electron population n and the hole population p are both much lower than the intrinsic carrier concentration n_i. Since there are so few mobile carriers under these conditions, carrier generation is the restorative process rather than carrier recombination. When the electric potential at the pn-junction is between the hole and electron quasi-Fermi levels, the equation[1] for the generation region width x_i is

$$x_i = x_d - \left[\sqrt{\frac{2\varepsilon_{Si}kT}{q^2}}\left(\sqrt{\frac{1}{N_A}ln\frac{N_A}{n_i}} + \sqrt{\frac{1}{N_D}ln\frac{N_D}{n_i}}\right)\right] \tag{II.4}$$

Fig. II.5 compares the electron and hole populations, the depletion region widths, and

[1]The expression for generation width given by equation (13) in [35] incorrectly shows that the right hand term inside the parenthetical expression is subtracted rather than added. A full derivation of equation II.4 above is provided in Appendix F.

the generation region widths calculated for a symmetrical *pn*-junction ($N_{A,D}$ = 10^{16} cm^3) reverse-biased at 0 V, -4 V, -8 V, and -12 V. Electron populations are represented as thick dashed lines in Fig. II.5, and hole populations are shown as thick solid lines. Generation region widths are shown as thin solid arrows superimposed on the thin dashed arrows representing depletion region widths.

When the junction is grounded, the depletion region width x_d is 0.43 μm due to the built-in junction voltage of 0.72 V, but the generation region width x_i is 0 μm. The product of the electron and hole populations *pn* is always greater than n_i^2, so there is no net generation. At a reverse bias of -4 V, x_i is 0.34 μm, approximately 60% of of x_d. Generation is the dominant restorative force inside the the region bounded by x_i, so the magnitude of the net current is greater than zero. The ratio of the generation region width to the depletion region width increases with the magnitude of reverse bias. When the *pn*-junction is reverse-biased at 8 V, x_i is 71% of x_d, and at a reverse bias -12 V, x_i is 76% of x_d. As the reverse bias magnitude increases, so does the volume of the device in which radiation-induced damage contributes to reverse current through SRH generation. Because of uncertainties in junction grading and depletion region geometry, the generation region width x_i is frequently approximated as the depletion region width x_d in reverse current calculations when the reverse bias magnitude is greater than zero [34]. This approximation is used for modeling current step distributions in Chapter IV.

II.2.2 Minority Carrier Lifetime and Increased Defect Density

The minority carrier lifetimes for electrons (τ_{n0}) and holes (τ_{p0}) represent the average amount of time that carriers will exist before recombining [34]. Minority carrier lifetimes are calculated in [34] from SRH theory as

$$\tau_{n0,p0} = (v_{th}\sigma_{n,p}N_t)^{-1}. \tag{II.5}$$

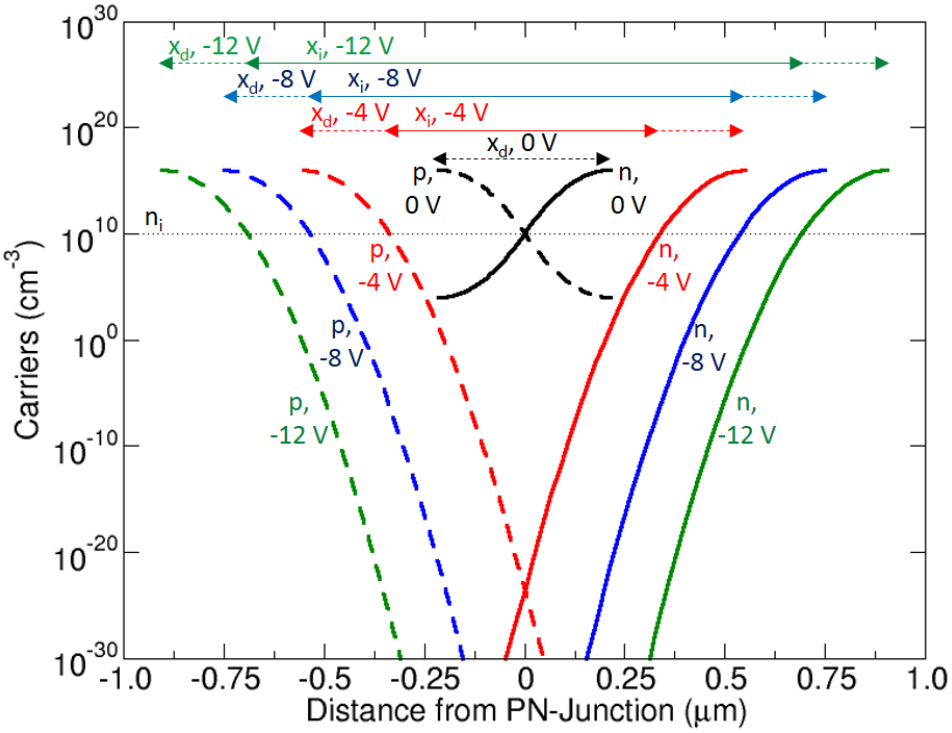

Figure II.5: Electron and hole populations, depletion region widths, and generation region widths in a symmetrical *pn*-junction ($N_{A,D}$=10^{16} cm^{-3}) biased at 0 V, -4 V, -8 V, and -12 V.

Silicon vacancies and self-interstitial defects have energy levels near midgap. In [36], the authors report that vacancies have an energy level of $E_v + 0.47$ eV and a capture cross-section values of $\sigma_{n,p} = 9\times10^{-16}$ cm^2 for both electrons and holes. Self-interstitial defects are reported to have an energy level of $E_c - 0.44$ eV, an electron capture cross-section of $\sigma_n = 9.2\times10^{-15}$ cm^2, and a hole capture cross-section of $\sigma_p = 9.1\times10^{-14}$ cm^2 [36].

Vacancy and interstitial point defects are not stable, and they are mobile within the silicon lattice[19]. The majority of isolated vacancy and interstitial pairs (Frenkel defects) anneal within 1 ms of their creation [19]. Vacancies that remain after this short-term annealing period form stable, relatively immobile defects such as divacancies [18], E-centers (vacancy plus phosphorus [20] or vacancy plus arsenic [21]), A-centers (vacancy plus oxygen [22]), and complex clusters [19]. Divacancies and E-centers are both near-midgap recombination-generation centers that have been reported for DLTS measurements of ^{252}Cf-irradiated silicon diodes [37]. Interstitial silicon atoms can displace boron atoms

from the lattice of p-type silicon, and this changes the local doping dynamics while creating interstial boron defects [38].

Although vacancy and interstitial defects are unstable on the timescale of milliseconds, this does not preclude the use of reported values for their capture cross-sections and energy levels along with simulated values of radiation-induced populations in the SRH generation expression for calculations of modeled current step sizes that are consistent with the size distribution of measured current steps. Since NIEL values have been used to successfully predict damage factors with calculations that include the number of radiation-induced vacancies and recoil atoms while excluding stable defects and annealing from consideration [32], vacancy and interstitial defects have been chosen to model current steps.

Since generation dominates over recombination when the number of mobile carriers is less than ${n_i}^2$ inside depletion regions, the pre-irradiation defect density is considered here to be the number of recombination-generation centers N in a depletion region divided by the volume of that depletion region, or $N_t = N/Ax_d$. Radiation-induced displacement damage increases the number of defects throughout the device, but only defects inside the depletion region contribute to SRH generation. The post-irradiation expressions for τ'_{n0} and τ'_{p0} attributed to vacancy and interstitial defects are given by (II.6) and (II.7).

$$\tau'_{n0}{}^{-1} = \left(\frac{1}{v_{th}\sigma_{n,vac}\frac{N_{vac}+N'_{vac}}{Ax_d}} \right)^{-1} + \left(\frac{1}{v_{th}\sigma_{n,int}\frac{N_{int}+N'_{int}}{Ax_d}} \right)^{-1} \tag{II.6}$$

$$\tau'_{p0}{}^{-1} = \left(\frac{1}{v_{th}\sigma_{p,vac}\frac{N_{vac}+N'_{vac}}{Ax_d}} \right)^{-1} + \left(\frac{1}{v_{th}\sigma_{p,int}\frac{N_{int}+N'_{int}}{Ax_d}} \right)^{-1} \tag{II.7}$$

where N'_{vac} is the number of new vacancies created in the depletion region, and N'_{int} is the number of new interstitials inside the depletion region.

II.2.3 Generation Lifetime and Electric Field-Enhanced Emission

The generation lifetime associated with a defect represents the relative frequency of carrier emission. As the generation lifetime decreases, the defect emission rate increases. The term trap will be used to indicate localized energy states in the following discussion of carrier trapping and emission. The expression for the pre-irradiation generation lifetime τ_{g0} in (II.8) incorporates the minority carrier lifetimes for electrons and holes, τ_{n0} and τ_{p0} [31].

$$\tau_{g0} = \tau_{n0} e^{(E_i - E_t)/kT} + \tau_{p0} e^{(E_t - E_i)/kT} \tag{II.8}$$

In the absence of an electric field, if E_t is greater than the intrinsic Fermi level E_i, the trap is more effective at emitting electrons to the conduction band E_c than it is at emitting holes to the valence band E_v. Conversely, the trap is more effective at emitting holes to the valence band than electrons to the conduction band if the trap level is lower than the intrinsic Fermi level. In a zero field region, the localized energy states closest to the intrinsic Fermi level are the most effective generation centers.

The presence of an electric field reduces the amount of thermal energy required for carrier emission from a trap, and this field-enhanced emission is known as the Poole-Frenkel effect [17]. Treatments of the Poole-Frenkel effect with respect to electron emission to the conduction band are provided for different potentials and defects in [28], [27], and [39]. Following the method of [9], midgap defects are treated as 1-D Coulomb potentials for the calculation of electric field enhancement through the Poole-Frenkel effect.

Fig. II.6 shows an energy band diagram for a *pn*-junction that contains two traps modeled as 1-D Coulomb potentials[2]. Both traps have energy level E_t. The first trap exists in the zero-field, quasi-neutral region of the semiconductor. The thermal activation energy needed to emit an electron from E_t to E_c is labeled $E^0_{act,n}$. The thermal activation energy needed to emit an electron from the valence band to the trap level, otherwise known as hole emission from E_t to E_v, is labeled as $E^0_{act,p}$. In a zero field region, the electron activation

[2]This band diagram is published in [33] showing only the trap in the *pn*-junction depletion region.

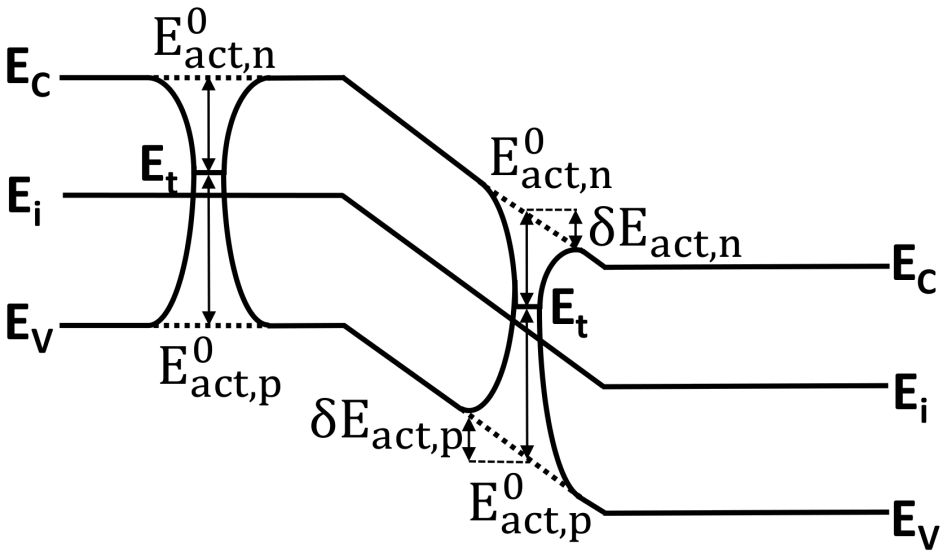

Figure II.6: Energy band diagram showing two defects modeled as 1-D Coulomb potentials. The presence of an electric field distorts the Coulomb potential so that the barrier heights for both electron emission from the trap to the conduction band ($E^0{}_{act,n}$) and hole emission from the trap to the valence band ($E^0{}_{act,p}$) are lowered by $\delta E_{act,n} = \delta E_{act,p}$.

energy is described by II.9, and the hole activation energy is described by II.10.

$$E^0{}_{act,n} = E_c - E_t \tag{II.9}$$

$$E^0{}_{act,p} = E_t - E_v. \tag{II.10}$$

The second trap shown in Fig. II.6 exists in the *pn*-junction's depletion region where the electric field strength is $\mathcal{E}$. The electric field lowers the Coulomb barrier with respect to the conduction band on one side of the trap. The thermal activation energy $E_{act,n}$ needed to emit an electron from E_t to E_c becomes $E_c - (E_t - \delta E_{act,n})$. The electric field also lowers the Coulomb barrier with respect to the valence band, so the thermal activation energy $E_{act,p}$ needed to emit a hole from E_t to E_v is $(E_t - \delta E_{act,p}) - E_v$.

A 1-D Coulomb potential in an electric field $\mathcal{E}$ can be modeled as

$$V(r) = \frac{-q^2}{4\pi\varepsilon_{Si}} - \mathcal{E}rcos(\theta) \tag{II.11}$$

where r is the distance between the electron and the ionized trap, and θ is the angle between r and the direction of the electric field [28]. The maximum reduction in Coulomb barrier height is calculated by evaluating the potential $V(r)$ at distance r_{max} where $\frac{\delta V}{\delta r}$ is equal to 0 and θ is set to 0°[28]. The reduction in Coulomb barrier height $\delta E_{act,n,p}$ for electron and hole emission is calculated with II.12 [9].

$$\delta E_{act,n,p} = \sqrt{\frac{q\mathcal{E}}{\pi\varepsilon_{Si}}} \tag{II.12}$$

The Coulomb barriers for both electron and hole emission are reduced by $\delta E_{act,n,p}$. Two effective trap levels emerge at levels $E_t + \delta E_{act,n}$ for electron emission and $E_t - \delta E_{act,p}$ for hole emission.

As the electric field $\mathcal{E}$ increases, the trap at E_t becomes more effective at both electron and hole emission compared to a trap at level E_t in a zero-field region. The pre-irradiation generation lifetime equation from (II.8) becomes

$$\tau_{g0}(\mathcal{E}) = \tau_{n0} e^{(E_i-(E_t+\delta E_{act,n}))/kT} + \tau_{p0} e^{((E_t-\delta E_{act,p})-E_i)/kT}. \tag{II.13}$$

Fig. II.7 shows the divergence of electron and hole trap levels for 1-D Coulomb potential models of interstitial and vacancy defects as electric field increases. The zero field trap levels for interstitial and vacancy defects used in Fig. II.7 are taken from [36]. At electric fields less than 10^3 V/cm, interstitials are more effective at electron emission than hole emission since E_t is greater than E_i, and vacancies are more effective at hole emission than electron emission since E_t is less than E_i. The divergence of electron and hole trap levels is clear once the electric field reaches 10^4 V/cm.

When the electric field is 10^5 V/cm, a field strength commonly present in the depletion regions of reverse-biased *pn*-junctions, the interstitial defect is even more effective at electron emission than it was at lower electric fields since the effective E_t value for electrons is closer to the conduction band, but it has also become more effective at hole emission

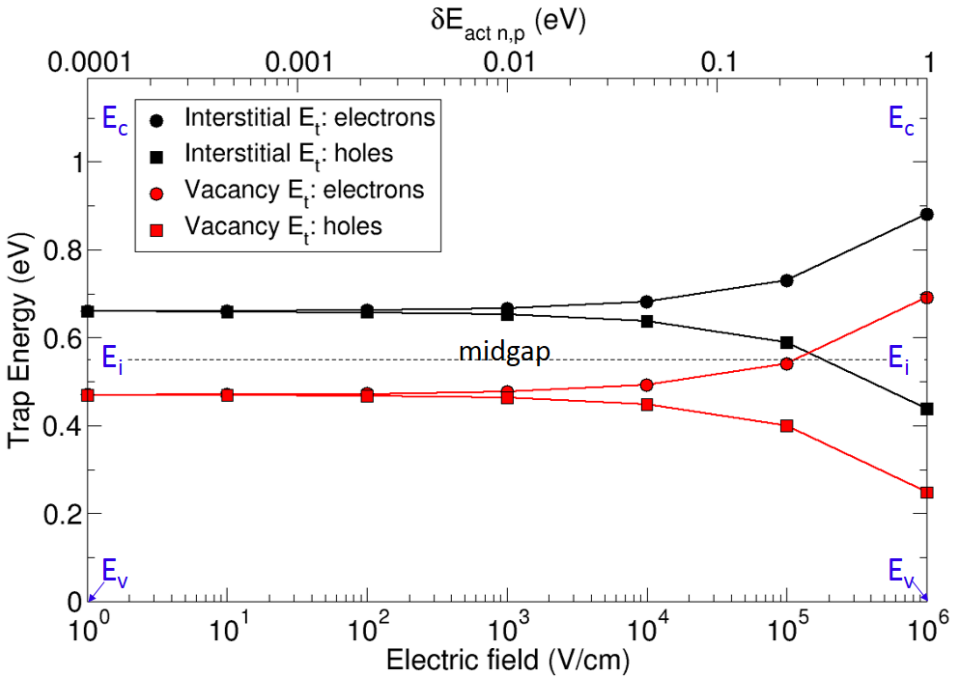

Figure II.7: Effective trap levels for electrons and holes vs. electric field strength shown for silicon vacancy and self-interstitial defects modeled as 1-D Coulomb potentials, after Auden *et al.*, 2013. Zero field trap levels E_t for vacancies and interstitials are taken from Lazanu and Lazanu, 2006.

since the effective E_t value for holes is now close to E_i. The exponential term modifying the minority carrier lifetime for interstitial hole emission in (II.13) is closer to unity than it is in the zero-field generation lifetime expression, so generation lifetime is reduced and the interstitial carrier emission rate is increased. Similarly, the vacancy defect has become more effective at hole emission compared to lower electric field conditions since its effective E_t value for holes is closer to the valence band, and the effective E_t value for electrons is close to E_i.

In zero field regions, generation lifetime is minimized when the exponential terms for both carriers in (II.8) are close to unity. In high electric field regions, the generation lifetime expressed in (II.13) is minimized when the exponential term for one carrier is close to unity and the exponential term for the other carrier is less than unity.

Once new defects are introduced through displacement damage, the expression for generation lifetime incorporates the post-irradiation minority carrier lifetimes $\tau'_{n,p}$ that have been modified by increased defect density as in (II.6) and (II.7). The post-irradiation generation lifetime $\tau_g(\mathcal{E})$ is expressed as

$$\tau_g(\mathcal{E}) = \tau'_{n0} e^{(E_i-(E_t+\delta E_{act,n}))/kT} + \tau'_{p0} e^{((E_t-\delta E_{act,p})-E_i)/kT}. \tag{II.14}$$

II.2.4 Current Steps Caused by Radiation-Induced Damage

Reverse current is composed of the diffusion current that arises in the diode's quasi-neutral regions and the generation current created in the depletion region [40]. The ideal diode equation given in II.15 describes the bias-dependent current I that results from electron injection from the depletion region into the p-type side of the quasi-neutral region and from hole injection into the n-type side of the quasi-neutral region:

$$I = qA\left(\sqrt{\frac{D_p}{\tau_p}}\frac{n_i^2}{N_D} + \sqrt{\frac{D_n}{\tau_n}}\frac{n_i^2}{N_A}\right)\left(e^{qV_a/kT} - 1\right) \tag{II.15}$$

where D_n and D_p are the diffusion coefficients of holes and electrons [34].

In a reverse-biased diode, current calculated with the ideal diode equation approaches zero, so SRH generation current in the depletion region makes the dominant contribution to total reverse current. Radiation-induced defects incease the number of electrons and holes generated in the depletion region of a reverse-biased *pn*-junction, and these carriers contribute to the total reverse current measured across a diode. Assuming that the doping profile and bias conditions applied to a diode are held constant, the maximum reverse current I_R is inversely proportional to the generation lifetime τ_g, and I_R can be calculated with II.16 [31][3].

$$I_R = \frac{qn_iAx_d}{\tau_g} \tag{II.16}$$

Single particle displacement damage increases the density of vacancy and interstitial defects, consequently decreasing the generation lifetime. In [3], the incremental increase in generation current density following displacement damage is calculated based on the difference of ${\tau_g}^{-1}$ and ${\tau_{g0}}^{-1}$. The same method is used here to calculate the incremental increase in reverse current ΔI_R, taking into account the electric field-induced reductions in thermal activation energy included in $\tau_g(\mathcal{E})$ and $\tau_{g0}(\mathcal{E})$. If I_{R0} is the pre-irradiation reverse current and I_R is the post-irradiation reverse currve, then ΔI_R can be calculated as

$$\Delta I_R = I_R - I_{R0} = qn_iAx_d\left(\frac{1}{\tau_g(\mathcal{E})} - \frac{1}{\tau_{g0}(\mathcal{E})}\right). \tag{II.17}$$

Although defects in the quasi-neutral regions can increase diffusion current by decreasing the minority carrier lifetimes in these regions, the relative contribution to total reverse current made by depletion region generation current dominates over diffusion current in

[3] In 1957, Sah, Noyce, and Shockley stated the expression for reverse current as $J_RA = \frac{qWn_iA}{2\tau_0}$, where J_R is reverse current density (equal to I_R/A) and W is the depletion region width denoted by x_d in this work [41]. The 1982 paper by Schroder corrects the expression for reverse current for the case when the hole and electron minority carrier lifetimes are not equal (for instance, because their capture cross-sections differ) so that the generation lifetime τ_0 is the appropriate denominator rather than $2\tau_0$ [31].

silicon diodes [34]. Diffusion current density is calculated as

$$J_{diff} = qn_i^2 \left(\frac{D_p}{N_d \sqrt{D_p \tau_p}} + \frac{D_n}{N_a \sqrt{D_n \tau_n}} \right) (e^{qV_a/kT} - 1) \tag{II.18}$$

where D_n and D_p are diffusion coefficients [34]. Diffusion current density is approximately 0.2% of the zero-field generation current density calculated for a comparable number of defects at room temperature. Although diffusion current varies with applied bias, it is not subject to electric field enhancement. The contribution of diffusion current is therefore neglected in this treatment of radiation-induced current step sizes.

Fig. II.8 shows the calculated increase in reverse current as a function of electric field strength and the number of radiation-induced defects. For each number of new defects listed on the *x*-axis, half the defects are characterized as vacancies and half are characterized as interstitials using energy levels and capture cross-sections reported in [36]. The device volume sensitive to defects that contribute to SRH generation is nominally assumed to be 10 μm^3.

Fig. II.8 shows that the size of a current step depends on both the number of new radiation-induced defects created in the depletion region and the strength of the electric field where the defects have been created. (It is assumed that electric field strength plays no role in the defect creation process itself; only the effect of field strength on defect emission rates is considered.) For a given electric field strength, step size varies linearly with the number of new defects. For a given number of defects, step size increases by a factor of 1.5 when electric field strength is increased by three orders of magnitude from 1 V/cm to 10^3 V/cm. At this field strength, the Coulomb barrier is lowered by 0.007 eV, or 1.5% of the energy difference between the conduction band and the trap level. However, step size increases by more than a factor of 10 when electric field strength is increased from 10^3 V/cm to 10^5 V/cm and the Poole-Frenkel effect lowers the Coulomb barrier by 0.07 eV, or 15% of the energy difference between the conduction band and the trap level.

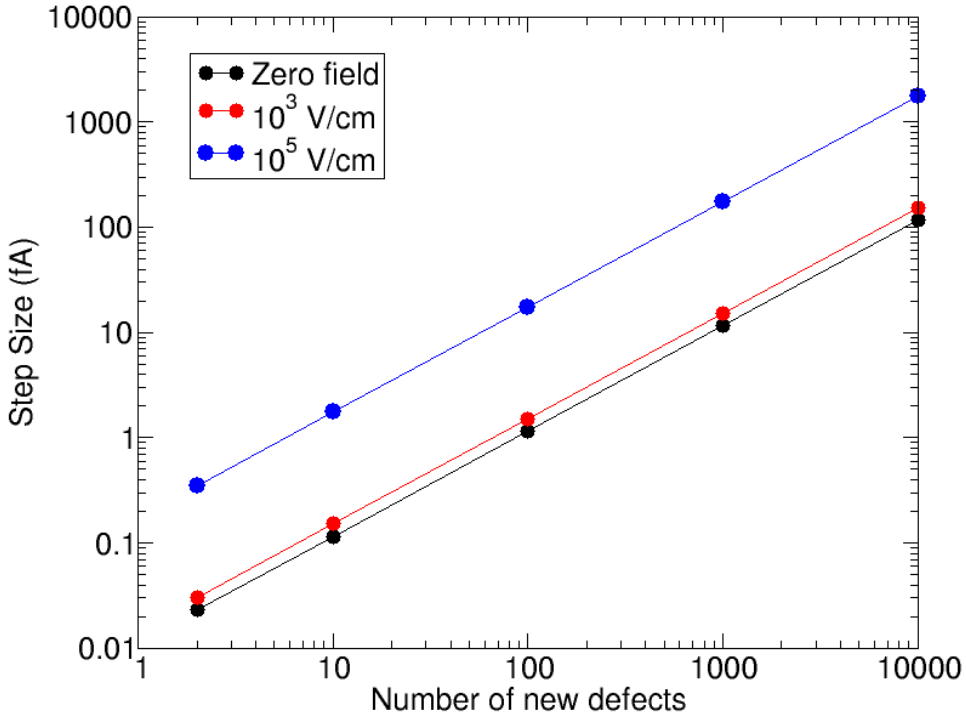

Figure II.8: Reverse current step size as a function of the number of new defects created in generation region and the electric field strength present where the defects are created. The volume of the generation region is nominally assumed to be 10 μm^3.

Electric field effects must be included in the expression for the generation lifetime in depletion regions where high electric fields are present. The size distribution of current steps induced by single particle displacement damage is underestimated if zero field defect energy levels are used in calculations of SRH generation. Current steps modeled using Monte Carlo simulations of increased vacancy and interstitial defects are compared with current steps measured in ^{252}Cf-irradiated diodes in section IV.2.3.

CHAPTER III

Measuring Single Particle Displacement Damage

This chapter presents *in situ* measurements of discrete changes in diode reverse current as a method for investigating electrical effects caused by single particle displacement damage. Fully characterized silicon diodes were irradiated with ^{241}Am and ^{252}Cf to compare the increases in reverse current caused by alpha particles and heavy ions. A low noise amplification (LNA) circuit has been constructed to measure both transient and permanent changes in reverse current that occur in the femtoampere and picoampere regimes. A current pulse occurs when an alpha particle or fission fragment strikes the diode's depletion region, creating an ionization event that deposits charge on the timescale of hundreds of picoseconds [42]. A current step is a discrete increase in reverse current associated with displacement damage that is sustained for minutes or hours. Examples of steps and pulses are presented in Section III.3. Section III.4 provides a full analysis of current steps associated with single particle displacement damage, including average and maximum step sizes, frequency of steps, and cross-sections of step size distributions.

Measurements of current steps observed in ^{252}Cf-irradiated JFET diodes with floating drains have been published in [16], and [33] compares measurements of current steps observed in JFET diodes with floating drains and grounded drains.

III.1 Device Characterization

Discrete increases in reverse current can be measured in irradiated diodes when individual particles create electrically active defects in depletion regions. Characterization of device materials and depletion region geometry provides insight into the number of defects that an incident particle is capable of creating inside a depletion region. The thickness of overlayer materials and silicon will influence where knock-on atoms are displaced and how far they travel within a device before evolving into stable displacement damage defects. Silicon

doping levels, the dimensions of doped regions, and device bias determine the dimensions and positions of depletion regions and the strength of their electric fields. Accurate models of electric field strengths within a depletion region are key to calculating the contributions to SRH generation made by depletion region defects. Data from laser testing is used to identify electrically active regions sensitive to ionizing and nonionizing radiation.

III.1.1 Device Materials

The devices used in this work are PAD1 series *n*-channel JFET diodes manufactured by Vishay / Siliconix [43]. The PAD1 diodes are packaged in TO-18 metal canisters which have been delidded with no damage to the chip or pins (see Appendix C for decapsulation details). Device areas were established with scanning electron microscope (SEM) images, and material thicknesses and doping profiles were obtained from the manufacturer [44]. Fig. III.1 shows a cartoon of the PAD1 diode materials, layer thicknesses, and doping levels. Each device has a *p*-type silicon substrate doped with 10^{16} cm^{-3} boron atoms. An *n*-type epitaxial layer of 10^{16} cm^{-3} arsenic atoms is grown on the substrate, and this layer has an area of 70 μm by 50 μm with a thickness of 4 μm. A *p*+ gate region approximately 2 μm thick with an area of 6 μm by 64 μm and an average doping profile of 10^{17} cm^{-3} boron atoms is diffused into the epitaxial layer. The source and drain collection regions are formed by *n*+ diffusions of 10^{17} cm^{-3} arsenic atoms diffused into the epitaxial layer on either side of the gate. The surface of the device is protected by two overlayers, 0.5 μm of SiO_2 under 1.0 μm of Si_3N_4.

Dispersive-energy x-ray spectroscopy can be used to identify materials present on the device surface. Fig. III.2 shows an SEM image of a JFET diode with the drain pad unbonded. Materials within the area encapsulated by the pink rectangle are analyzed with x-ray spectroscopy. Figs. III.3 (a), (b), and (c) show that nitrogen and oxygen are present along with silicon in the device shown in Fig. III.2. These elements correspond to the silicon nitride and silicon dioxide overlayers. Figs. III.3 (d), (e), and (f) show that the bond

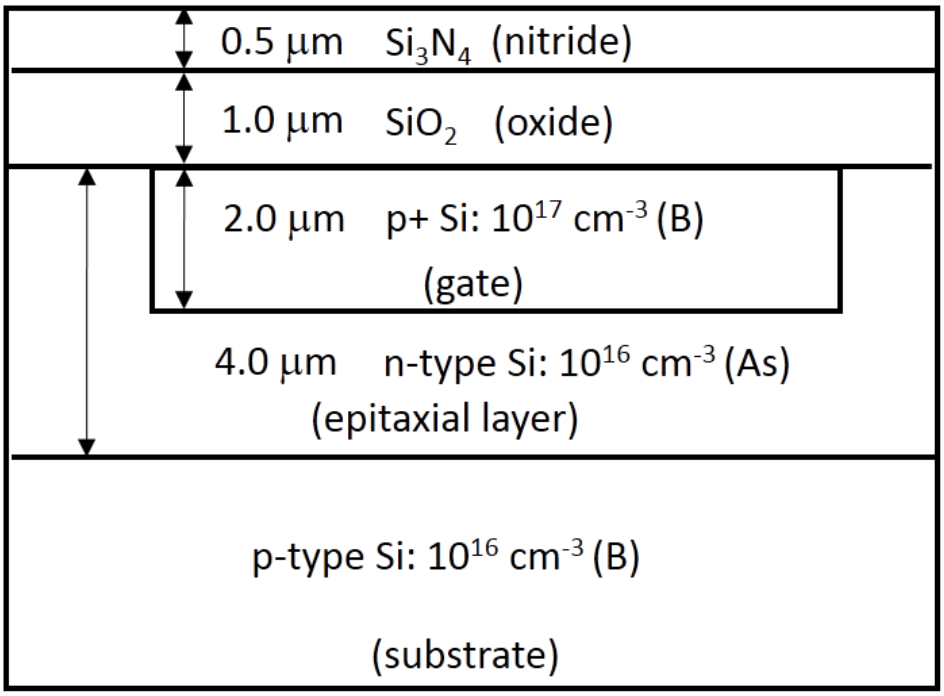

Figure III.1: Materials, doping, and layer thicknesses of a PAD1 JFET diode.

pads are aluminum, the bond wires are gold, and a trace amount of nickel from the diode can has fallen on the surface of the device.

III.1.2 Identification of Regions Sensitive to Radiation

Although these devices are fabricated as JFETs, they are bonded to operate as diodes. The source acts as the cathode, the gate acts as the anode, and the drain is left unbonded during the manufacturing process. Fig. III.4 shows an optical view of a PAD1 diode with the drain pad unbonded. The *p*+ gate overlaps the *p*-type subtrate, so the application of bias to the substrate also biases the gate. Under reverse bias, the gate / channel depletion region extends down to meet the epitaxial / substrate depletion region. The channel between the gate and the substrate is completely pinched off, so leakage current is kept extremely low since all carriers stem from SRH generation in the depletion regions. For the JFET diodes used in this work, the drain pad was bonded to the source pad to maximize the device area sensitive to ionization events and displacement damage. Fig. III.5 shows an optical

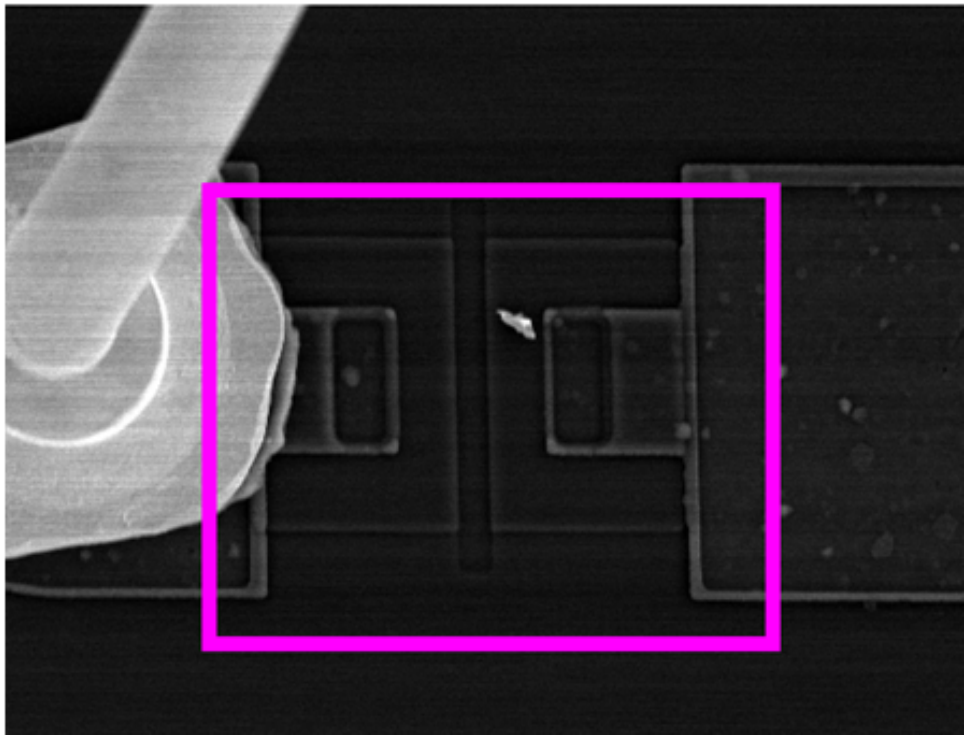

Figure III.2: Scanning electron microscope image of PAD1 JFET diode. X-ray analysis was used to determine the elements present within the area inside the pink rectangle.

view of a JFET diode with the drain bonded to the source. The JFET diodes exhibit a pre-irradiation leakage current magnitude of 15 fA with the gate biased at -12 V and the source grounded with the drain pad floating. Pre-irradiation leakage current is 30 fA when the diode is reverse-biased at 12 V with source and drain pads both grounded. The standard deviation σ of pre-irradiation reverse current measured every 150 ms for 24 h is 1.5 fA.

Two-photon absorption laser testing can be used to identify regions in a device that are sensitive to ionizing radiation. In this technique, a silicon device is irradiated with photons with energies less than the bandgap of silicon. Electrons within the device that absorb two-photons simultaneously are excited from the valence band to the conduction band, and these excited carriers can be collected as current [45]. The peak current maps in Fig. III.6 and Fig. III.7 show surface views of device regions where charge generated by two-photon absorption is collected by the source contact (and by the drain contact bonded to the source pad). The relative amount of charge generated at a given position is represented by a color

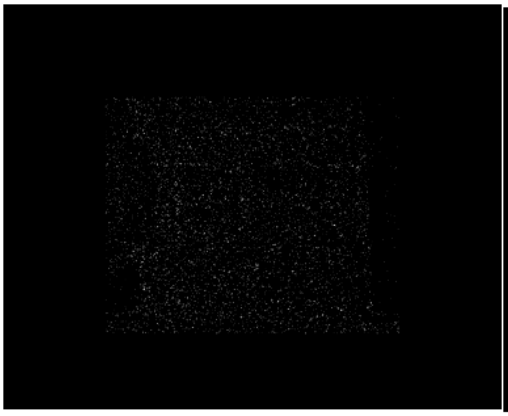

(a) Nitrogen

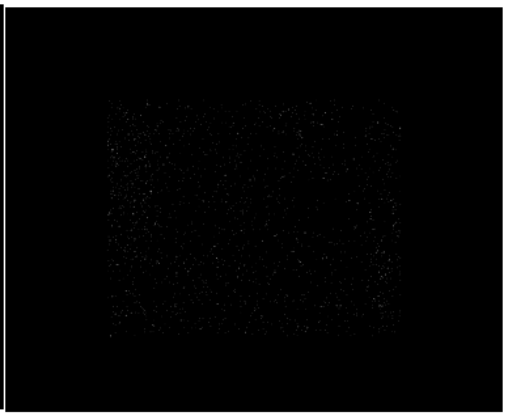

(b) Oxygen

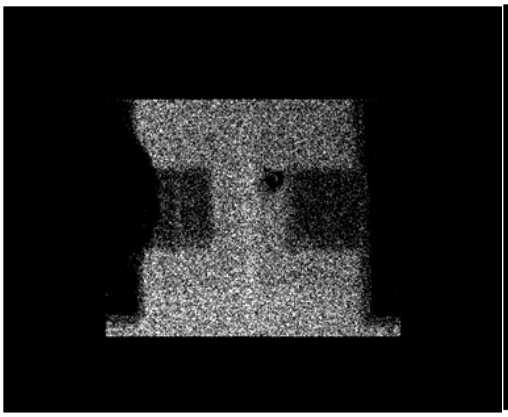

(c) Silicon

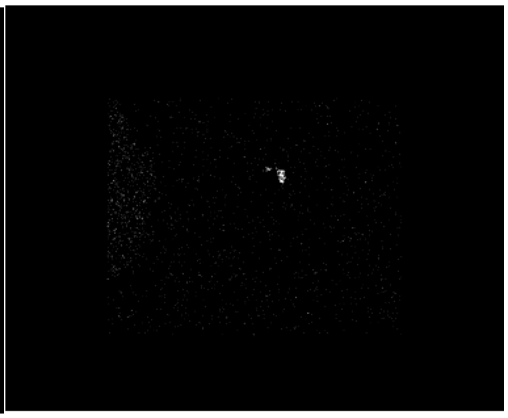

(d) Nickel

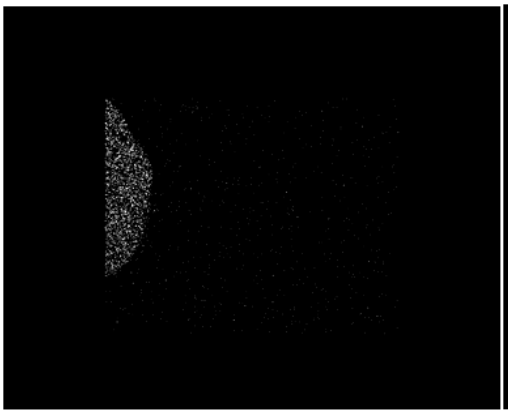

(e) Gold

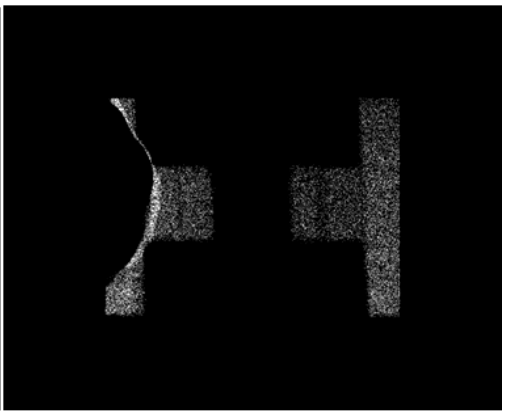

(f) Aluminum

Figure III.3: Dispersive-energy x-ray spectroscopy analysis of elements present in a PAD1 JFET diode.

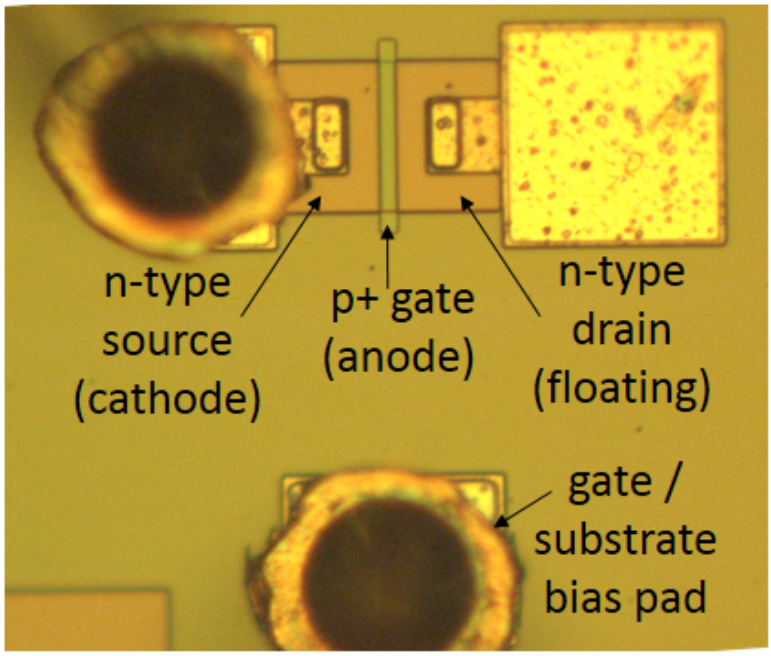

Figure III.4: Optical view of PAD1 JFET diode as manufactured with unbonded drain pad. The region between the gate and the drain is floating.

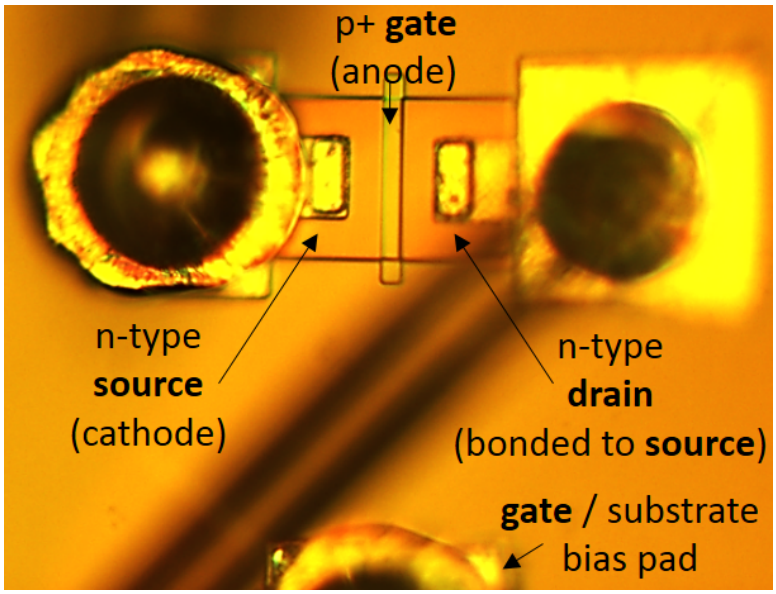

Figure III.5: Optical view of PAD1 JFET diode with the drain pad bonded to the source pad, after Auden *et al.*, 2013. The bias applied to the region between the gate and the drain is equal to the bias applied to the region between the gate and the source.

scale from red (high) to blue (low). Since charge generated by ionization is collected from a region symmetrical about the gate, charge generated by SRH generation in this region will also be collected. Therefore, the peak current map shows device regions that are sensitive to both ionization events and fluctuations in reverse current caused by displacement damage.

Fig. III.6 shows a peak current map for a PAD1 diode reverse-biased at -4 V with drain floating as shown in Fig. III.4. Peak current is highest on the source (cathode) side of the device and around the gate (anode). The region on the drain side of the device shows very little peak current. Although electrons are excited by two-photon absorption in this region, they are not collected as current since the drain pad is unbonded and the region between drain and gate is electrically floating. Only the regions bounded by the gate / epitaxial depletion region and the source side of the epitaxial / substrate depletion region are sensitive to ionizing radiation. It should also be noted that SRH generation and recombination processes from defects created in the electrically floating drain side depletion region will create zero net current, so the unbonded drain side is not sensitive to displacement damage caused by nonionizing radiation, either.

Fig. III.7 shows a normalized peak current map generated by two-photon absorption in a PAD1 diode with the drain pad bonded to the source pad as shown in Fig. III.5. Peak current is symmetrical on both sides of the gate. The regions bounded by the gate / epitaxial depletion region and both the source and drain epitaxial / substrate depletion regions are sensitive to ionizing radiation. Carriers generated through SRH generation in the gate / epitaxial depletion regions as well as the source and drain epitaxial / substrate depletion regions will be collected as current, so Fig. III.7 also indicates that both the drain and source regions are sensitive to displacement damage created by nonionizing radiation.

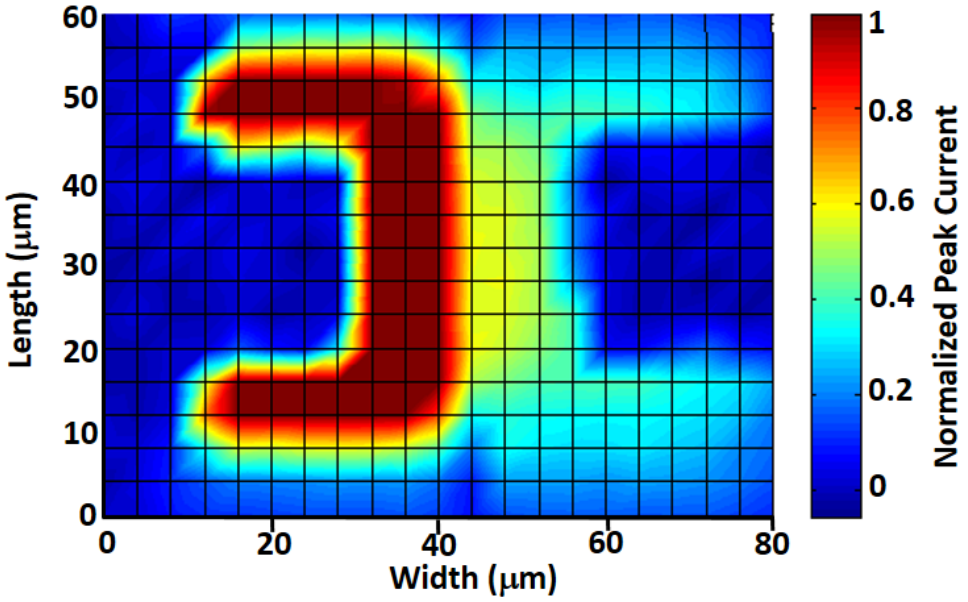

Figure III.6: Laser testing: normalized peak current in JFET diode with drain unbonded. The source is grounded, the gate is biased at -4 V, and the drain is floating.

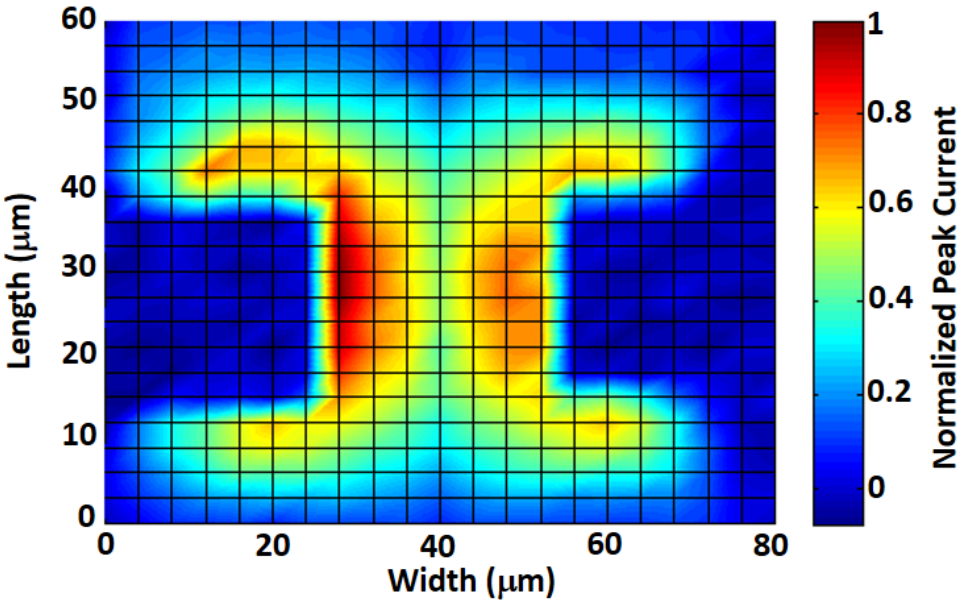

Figure III.7: Laser testing: normalized peak current in JFET diode with the drain pad bonded to the source pad. Drain and source are grounded.

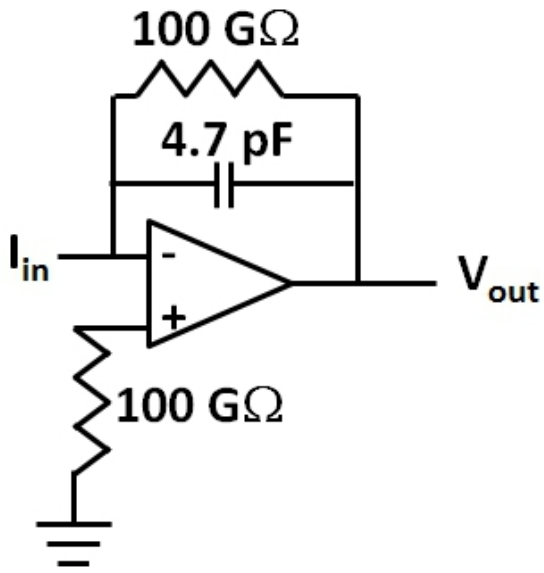

Figure III.8: Circuit diagram of current-to-voltage converter, after Auden *et al.*, 2012.

III.2 Reverse Current Measurement Circuit

III.2.1 Current-to-Voltage Converter Design

A low noise amplification circuit was built to measure diode currents in the range of -60 pA to +60 pA using a current-to-voltage converter. The converter consists of a 100 GΩ resistor connected between an LMC6001 op amp's negative input and output terminals while the positive input terminal is grounded. The output of an ideal op amp will change as needed to maintain a zero voltage differential between the op amp's input terminals when there is an external feedback loop [46]. The current-to-voltage converter's output is equal to the voltage drop across the 100 GΩ resistor. The converter's output voltage changes in response to the input current which, in this case, is the reverse current of a diode. The input reverse current I_R is obtained from the expression $I_R = \frac{V_{out}}{10^{11}\Omega}$. An input current with magnitude 10 fA is measured as an output voltage of 1 mV at the op amp's output terminal. A 4.7 pF capacitor is connected in parallel with the 100 GΩ resistor, so the current-to-voltage converter integrates current pulses at a rate set by the RC time constant of 0.47 s. A circuit diagram is shown in Fig. III.8 [47].

Several steps were taken to minimize circuit noise and leakage. The LMC6001 op amp is rated with an input offset current of less than 5 fA [48]. Guard rings encircle the op amp's positive and negative input terminals, and the positive input terminal is connected to ground via the 100 GΩ resistor to minimize bias current [47]. The op amp is held in a low-leakage socket made from gold-plated discrete component jacks [49]. All components are soldered in air to PTFE-coated wire. The circuit is enclosed in a diecast aluminum box to reduce electromagnetic noise.

The current-to-voltage converter's output voltage was read every 150 ms with an Agilent 34970A data acquisition unit. The 34970A was also used to bias the PAD1 diode at -12 V. A BK 1790 DC power supply provided the op amp supply voltages with V_{S+} equal to +6 V and V_{S-} equal to -6 V. BNC connectors mounted on the diecast aluminum box relayed the input voltages for V_{S+}, V_{S-}, and V_A as well as the output voltage signal V_{Out}.

III.2.2 Frequency Response

The frequency response of the current-to-voltage converter can be used to predict how the time-dependent output voltage will change with input current. The shape of the frequency response can be used to differentiate ionization events associated with particle strikes from stray noise. Two signals of interest are ionization events (in which transient electron-hole pairs are created on a timescale of hundreds of picoseconds [42]) and abrupt current steps (in which the creation of new defects permanently increases reverse current). The frequency response of the circuit shown in Fig. III.8 can be calculated from an s-domain transfer function equal to the total circuit impedance:

$$H(s) = \frac{V_{out}}{I_R} = \frac{\frac{-1}{C}}{s + \frac{1}{RC}} \tag{III.1}$$

where s is the complex frequency $\sigma + j\omega$, C is the value of the circuit's capacitor, and R is the value of the circuit's resistor.

The time response of the circuit's output voltage can be calculated by taking the inverse

Laplace transform of the transfer function multiplied by the s-domain expression for a signal that represents a change in reverse current. The circuit's time response to ionization events can be modeled as the product of total charge deposition Q and the delta function $\delta(t)$ as in equation III.2 . The Laplace transform for $\delta(t)$ is 1.

$$\Delta V_{out}(t) = \frac{-Q_{max}}{C} e^{\frac{-t}{RC}} \tag{III.2}$$

The maximum charge Q_{max} deposited by an ionizing particle with incident energy E_i can be calculated as

$$\Delta Q_{max} = \frac{qE_i}{E_{eh}} \tag{III.3}$$

where E_{eh} is the energy required to create an electron-hole pair in silicon, 3.6 eV [50]. Q_{max} values for typical ^{252}Cf decay products are 0.26 pC for 5.9 MeV alpha particles, 4.9 pC for 106 MeV Cd ions, and 3.6 pC for 80 MeV Nd ions. The size of the capacitor used in the converter circuit dictates both the magnitude of the output voltage pulse and how long the pulse takes to decay. Since Q_{max} values associated with typical ^{252}Cf decay products are on the order of 1 pC, a capacitor value between 1 and 10 pF allows ionization events to be recognized as voltage pulses with magnitudes of tens to hundreds of mV that decay on a timescale of seconds. Fig. III.9 shows the magnitude of the output voltage response for a 5.9 MeV alpha particle that deposits 0.26 pC and for a 106 MeV Cd ion that deposits 4.9 pC.

Abrupt current steps caused by displacement damage can be modeled as the magnitude of discrete reverse current increase ΔI_R multiplied by the unit step $u(t)$. The Laplace transform for $u(t)$ is $\frac{1}{s}$, and the time-dependent output voltage behavior following an abrupt current step is calculated in equation III.4.

$$\Delta V_{out}(t) = \Delta I_R R(e^{\frac{-t}{RC}} - 1) \tag{III.4}$$

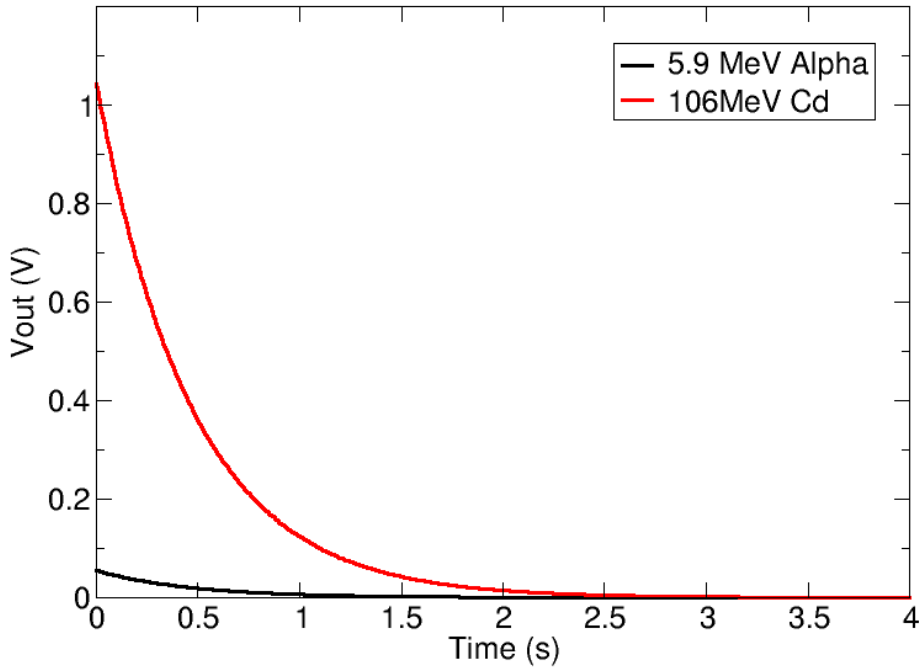

Figure III.9: Output voltage time response for ionization events modeled with the delta function $\delta(t)$.

Fig. III.10 shows the behavior of output voltage magnitude following an abrupt current step of 1 pA.

III.3 Device Irradiation

Although neutrons and protons are frequently used for displacement damage studies (e.g., [13], [8], [9]), heavy ions are ideal incident particles for investigating single particle displacement damage since they create more displacement damage per particle than nucleons. PAD1 diodes were irradiated with a 0.9 μCi ^{252}Cf radiation source that has an active area of 0.25 cm^2. The ^{252}Cf isotope undergoes alpha decay in 96.9% of decays, so the source produces a stream of 5.9 MeV alpha particles [51]. Spontaneous fission comprises the other 3.1% of decays. Fission decay results in the emission of two fission fragments (one light fragment and one heavy fragment), so the expected branching ratio of a ^{252}Cf radiation source is 16 alpha particles to 1 fission fragment emitted in 4π steradians.

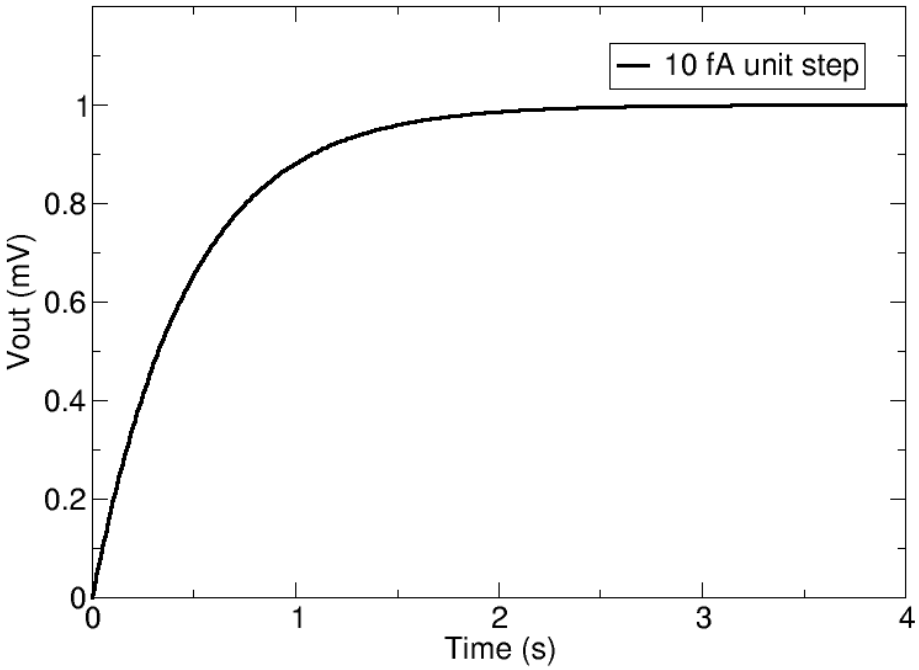

Figure III.10: Output voltage time response for abrupt current step modeled with the unit step $u(t)$.

Fig. III.11 shows the ^{252}Cf isotope's percentage yield of light and heavy fission fragments. The branching ratio of light fission fragments (with masses peaking at 106 a.m.u.) is equal to that of heavy fission fragments (with masses peaking at 140 a.m.u.) [52]. A typical heavy fission fragment emitted by a ^{252}Cf source is 80 MeV Nd, and 106 MeV Cd is a typical light fission fragment [53]. The ^{252}Cf isotope's fission decays also produce neutrons with an average energy of 2.1 MeV [54].

Because ^{252}Cf emits alpha particles and neutrons as well as heavy ions, diodes were also irradiated with a 0.1 μCi ^{241}Am alpha source to differentiate displacement damage effects caused by alpha particles from those caused by heavy ions. The ^{241}Am source emits 5.5 MeV alpha particles [55]. A comparison of reverse current time series for ^{241}Am and ^{252}Cf-irradiated diodes allows one to determine whether damage induced from alpha particles results in measurable, discrete increases in reverse current.

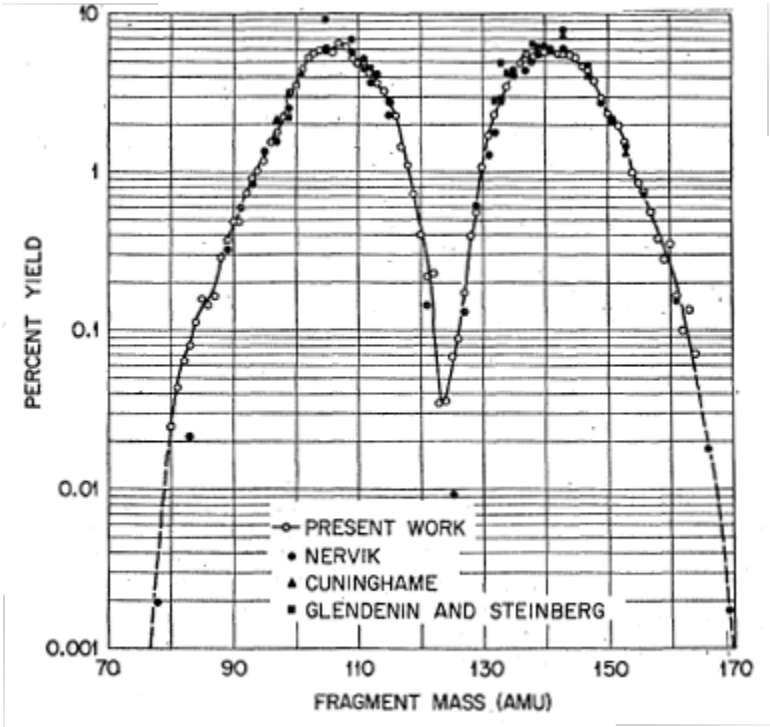

Figure III.11: Yield of ^{252}Cf fission fragments. The double peak indicates a 1:1 branching ratio of light and heavy fission fragments (after Schmitt, Kiker, and Williams, 1965)

III.3.1 Alpha Particle and Heavy Ion Irradiation in Air

To compare the damage produced by the ^{252}Cf source's fission fragments to that produced by alpha particles, diodes reverse-biased at -12 V were irradiated at room temperature with the ^{241}Am source and then the ^{252}Cf source at a distance of 2 mm in air from the surface of the diode's active area. Diode reverse current was monitored for 24 hours before the ^{241}Am source was introduced ("pre-irradiation"), for 24 hours during exposure to the ^{241}Am source ("^{241}Am"), and for a further 24 h after the ^{241}Am source was removed ("post-^{241}Am"). Next, reverse current was monitored for 24 hours while the diodes were exposed to the ^{252}Cf source ("^{252}Cf") and, finally, for 24 hours once the ^{252}Cf source was removed ("post-^{252}Cf"). Fig. III.12 shows the pre-irradiation, ^{241}Am irradiation, post-^{241}Am, ^{252}Cf irradiation, and post-^{252}Cf reverse current for a PAD1 diode irradiated in air.

The reverse current increased by 60 fA during 24 hours of ^{241}Am irradiation. No measurable, discrete increases in reverse current were observed during this period of irradiation

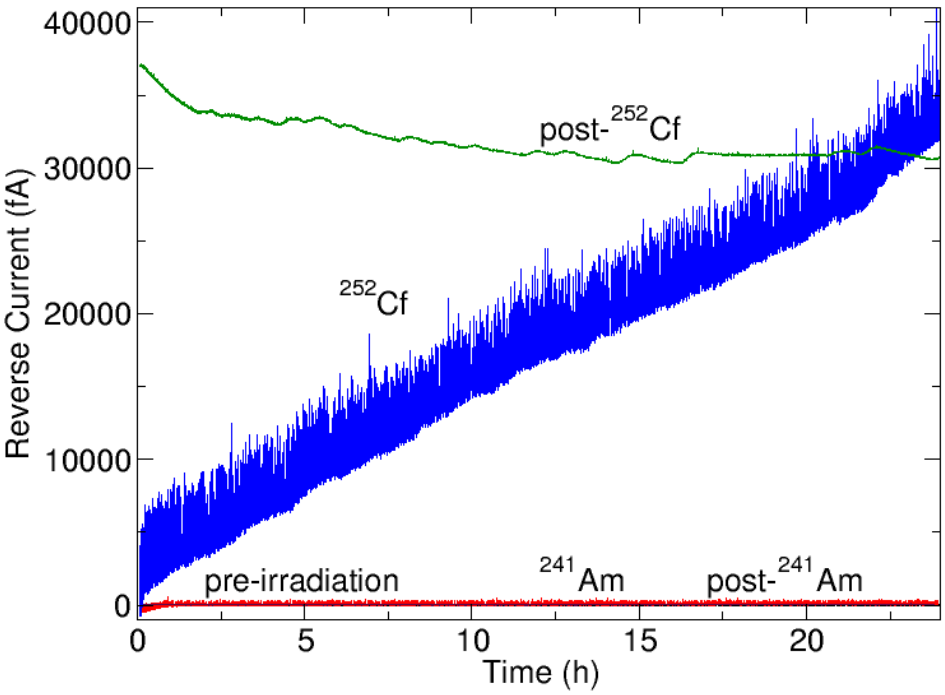

Figure III.12: Reverse current time series for PAD1 diode exposed to ^{241}Am and ^{252}Cf irradiation conditions for 24 h, after Auden *et al.*, 2012.

with alpha particles. The pre-irradiation, ^{241}Am irradiation and post-^{241}Am reverse current results are indistinguishable in Fig. III.12. During irradiation with the ^{252}Cf source, reverse current increased by 35 pA over 24 h. The noisy appearance of the ^{252}Cf data series on this timescale stems from transient current spikes caused by ion strikes approximately every 10 s. On a timescale of seconds, the ^{252}Cf data series can be resolved as individual current transients that correspond to alpha particles and fission fragments.

At a distance of 2 mm in air between radiation source and diode surface, the flux of all ^{252}Cf decay products incident upon the diode's active area is 6.6×10^4 particles/cm^2-s. This means that an average of 3.3 particles (or 0.2 fission fragments) strike the diode's active area every second. Because of the circuit's 0.47 s RC time constant, this rate of particle strikes is too high for current behavior to fully recover after each ionization event. Recovery time is defined as the amount of time required for the circuit's output voltage to return to the pre-strike level (1.5 fA, or 1 σ), assuming that no displacement damage has

Incident Energy (MeV)	Particle	Maximum Current Pulse Height (fA)	Recovery Time (s)
5.9	α	560	2.8
80	Nd	7600	4.0
106	Cd	10000	4.1

Table III.1: Ionization events: charge deposition and recovery time, after Auden *et al.*, 2012.

occurred. For instance, Table III.1 shows that the expected reverse current recovery time for an alpha particle-induced ionization event can last up to 2.8 s.

III.3.2 Heavy Ion Irradiation in Vacuum

To better observe single particle effects, the ^{252}Cf irradiation was repeated at a distance of 2 cm under vacuum to reduce the incident flux to 160 particles/cm^2-s. This flux corresponds to a strike rate of 0.008 particles/s (0.0005 fission fragments/s) incident upon the diode's active area, which is sufficient to allow the circuit response to fully recover between ionization events. The increased distance between source and diode reduced the rate of particle strikes, and the vacuum conditions eliminated energy loss due to collisions with air.

Fig. III.13 shows the reverse current vs. time for a PAD1 diode with drain floating irradiated with ^{252}Cf for 118 h in a vacuum chamber. The vacuum chamber was held at a mild vacuum pressure of 16 mbar. The flux of ^{252}Cf decay particles incident upon the diode's active area was 160 particles/cm^2-s. The diode was biased at -12 V, as with the "in-air" experiment. These irradiation conditions were repeated for two additional diodes with drain floating, and the relevant time series are shown in Figs. III.14 and III.15. Figs. III.16, III.17, and III.18 show reverse current time series for three ^{252}Cf-irradiated diodes with the drain grounded. The reverse current time series for the diode labeled "Drain Floating #1" is used to describe typical current behavior observed in all six irradiated diodes. A full comparison of current steps and pulses observed in diodes with drains floating grounded is presented in Section III.4.

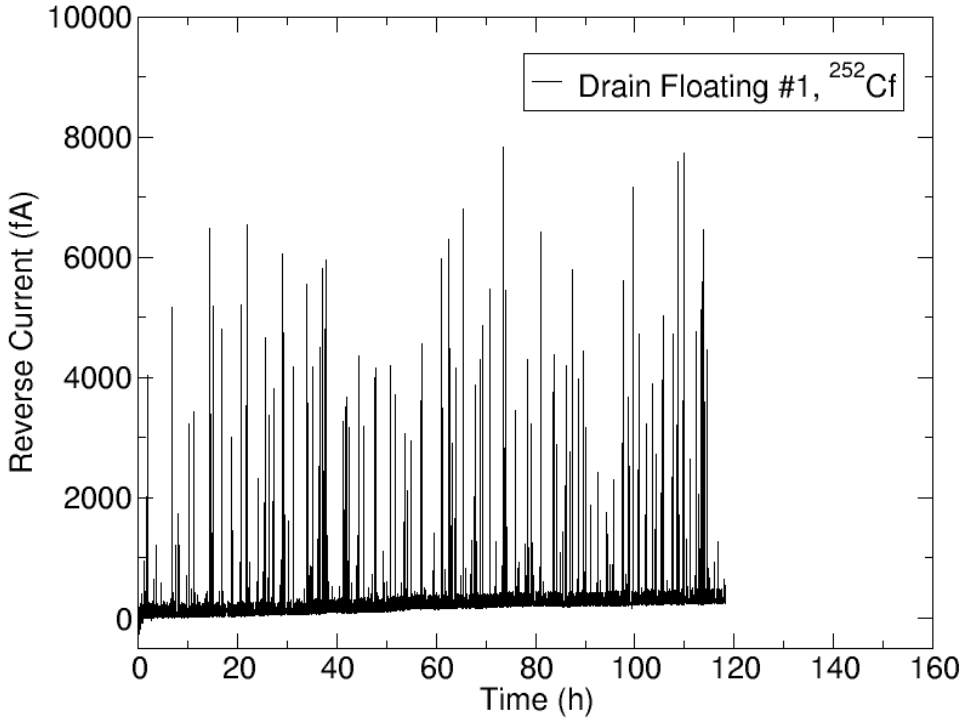

Figure III.13: 118 hours of a reverse current time series for a PAD1 diode labeled "Drain Floating #1" irradiated with ^{252}Cf under vacuum, after Auden *et al.*, 2012. Drain pad is unbonded.

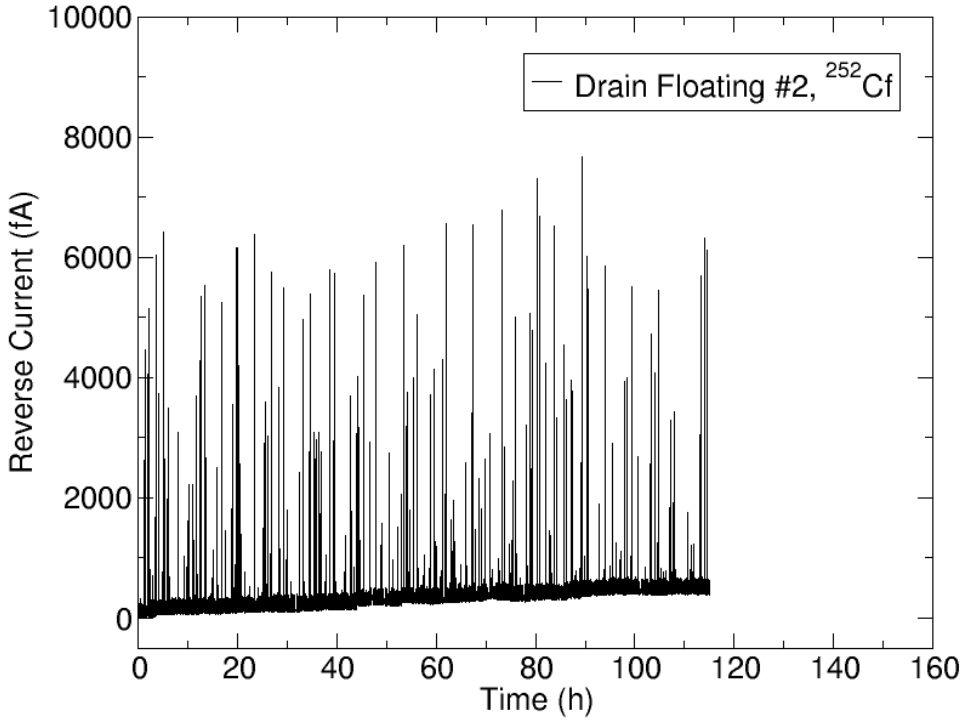

Figure III.14: 117 hours of a reverse current time series for a PAD1 diode labeled “Drain Floating #2” irradiated with ^{252}Cf under vacuum. Drain pad is unbonded.

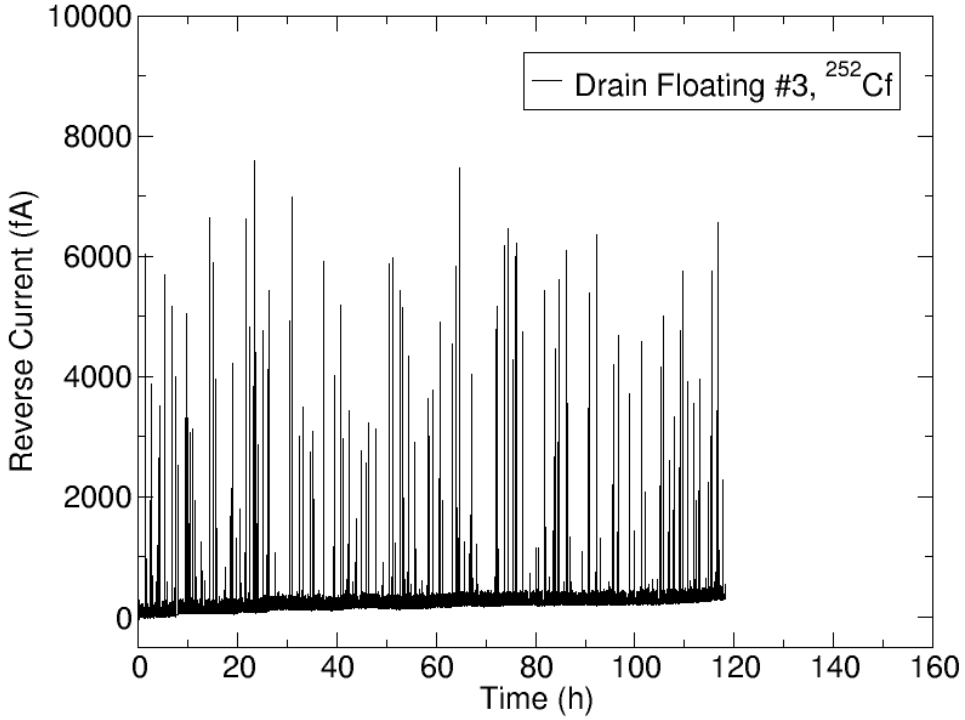

Figure III.15: 118 hours of a reverse current time series for a PAD1 diode labeled “Drain Floating #3” irradiated with ^{252}Cf under vacuum. Drain pad is unbonded.

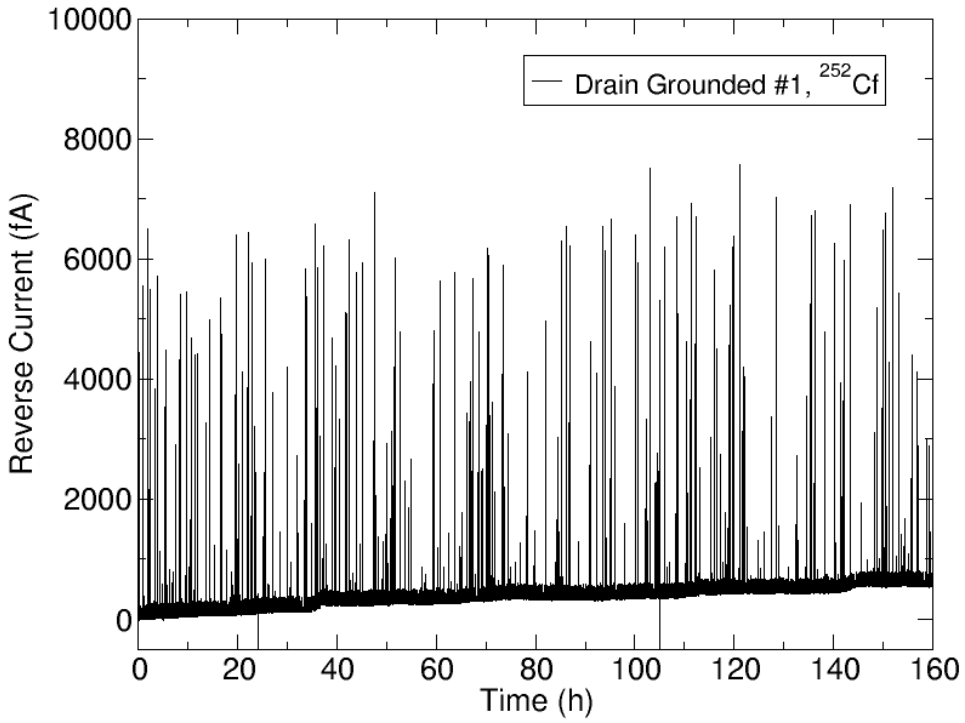

Figure III.16: 160 hours of a reverse current time series for a PAD1 diode labeled "Drain Grounded #1" irradiated with ^{252}Cf under vacuum. Drain pad is bonded to source pad. Note: the ^{252}Cf source was placed 4 cm from the diode's active area for this irradiation cycle.

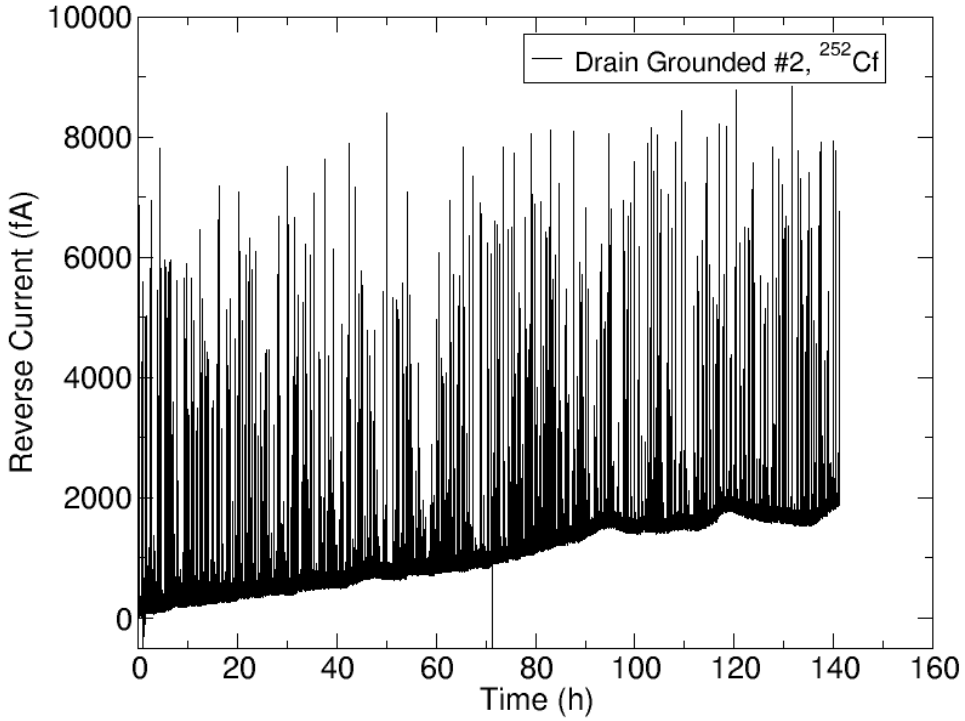

Figure III.17: 141 hours of a reverse current time series for a PAD1 diode labeled "Drain Grounded #2" irradiated with ^{252}Cf under vacuum. Drain pad is bonded to source pad.

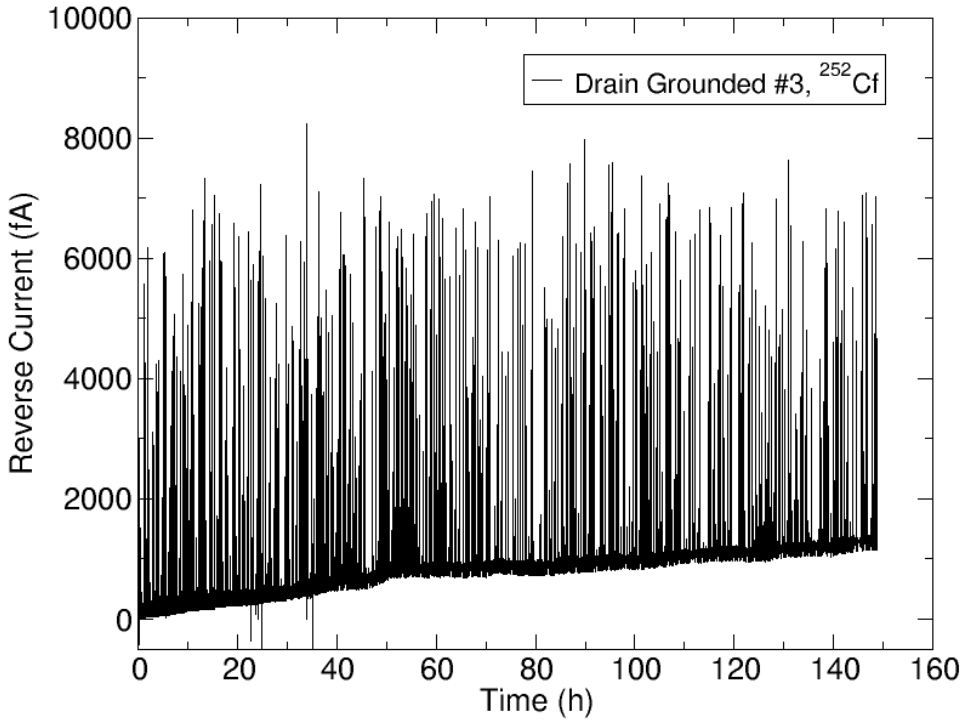

Figure III.18: 148 hours of a reverse current time series for a PAD1 diode labeled "Drain Grounded #3" irradiated with ^{252}Cf under vacuum. Drain pad is bonded to source pad.

Reverse current increased by 243 fA during 118 h of irradiation for the first of three diodes irradiated with the drain floating. The time series shown in Fig. III.13 can be examined in much greater detail than the time series shown in Fig. III.12 since the diode is positioned 10 times further from the ^{252}Cf source's active area, so more time elapses between particle strikes. Current pulses from individual fission fragments can be seen in the times series shown Fig. III.13. The average time between fission fragment strikes is $\tilde{0}$.6 h. Since radioactive decay is a Poisson process, one expects apparent clusters of events (e.g. the hour around t=42 h, probability of at least 3 events = 0.23) as well as intervals of up to several times the mean life with no decay events (as with the hour around t=20 h, probability = 0.19).

Figs. III.19, III.20, and III.21 each show a 1 h interval of the reduced-flux results shown in Fig. III.13. During each interval, at least one discrete, sustained increase (or step) in reverse current is apparent following a fission fragment ionization event. A current step is defined here as a discrete increase between sequential data points that is greater than 1.5 fA. This increase must be sustained for at least 500 data points (approximately 75 s) to differentiate this long term current step behavior from the short-lived current pulses that identify ionization events. The top panels in Figs. III.19 III.21 show reverse current on a scale of 0 to 5000 fA so that the fission fragment ionization events are obvious. The bottom panel of each figure shows reverse current on a 50 fA scale so that current steps of 5 fA or more are clearly visible.

The top panel of Fig. III.19 shows a single current pulse of 3200 fA that occurs at t = 10.2 h. Table III.1 states that the maximum current pulse caused by a 5.9 MeV alpha particle is 560 fA for this circuit. Therefore, one may conclude that the current pulse at t = 10.2 h is caused by a fission fragment. In addition, this current pulse is the only ionization event that is conclusively caused by a fission fragment between hours 10 and 11 of irradiation.

The bottom panel of Fig. III.19 shows that a 15 fA step coincides with the 3200 fA

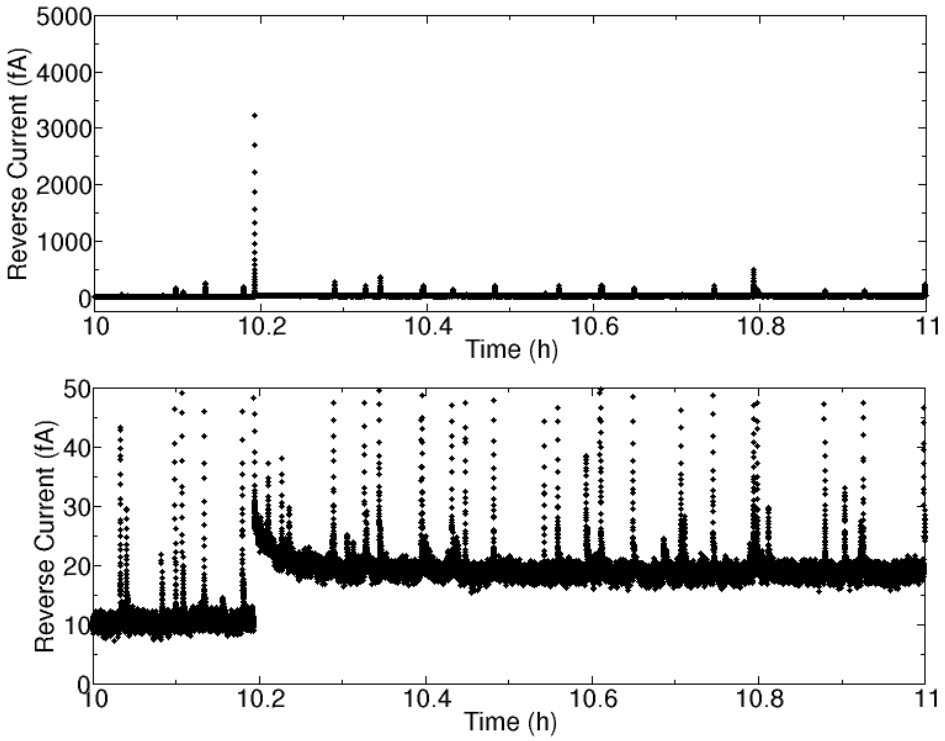

Figure III.19: Reverse current time series showing fission fragment-induced ionization event and discrete increase of 15 fA in reverse current at t=10.2 h, after Auden *et al.*, 2012.

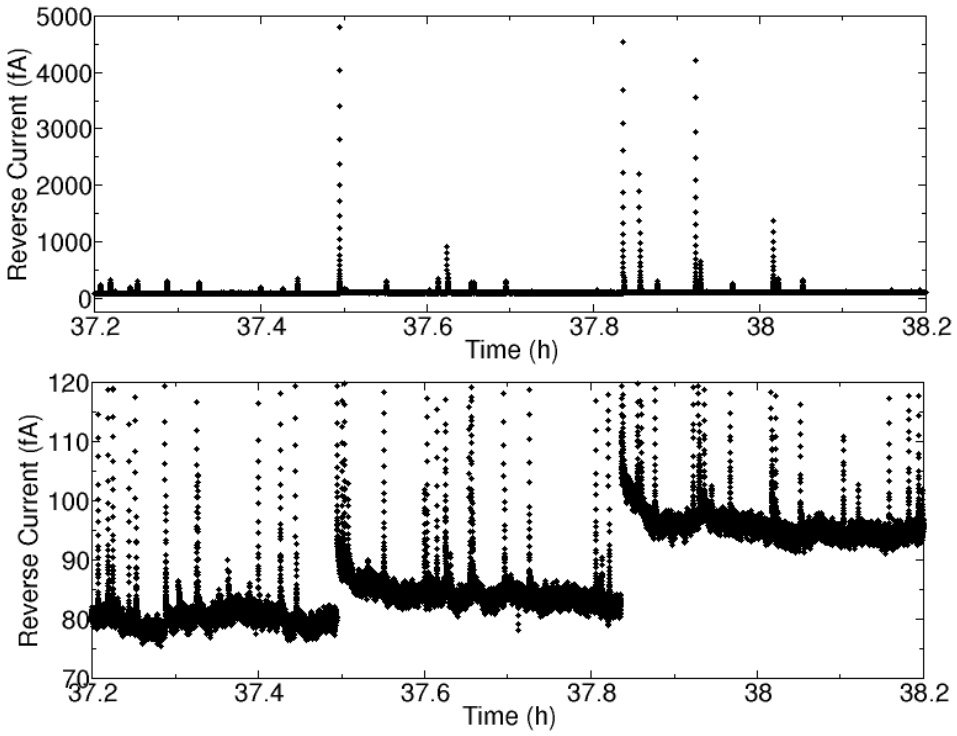

Figure III.20: Time series showing fission fragment-induced ionization event and corresponding 6 fA discrete increase in reverse current at t=37.5 h. A second discrete increase of 20 fA with corresponding fission fragment induced ionization event is visible at t=37.85 h, after Auden *et al.*, 2012.

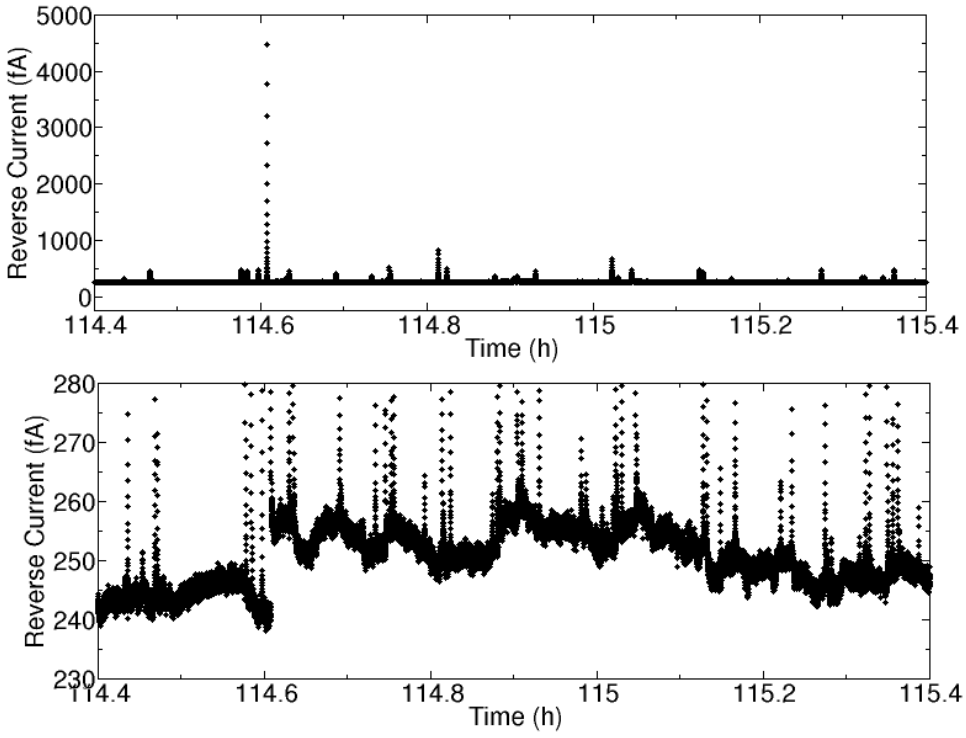

Figure III.21: Time series showing fission fragment-induced ionization event and corresponding 12 fA discrete increase in reverse current at t=114.6 h, after Auden *et al.*, 2012.

pulse. After the initial 15 fA step, reverse current decreases over a few minutes between t=10.2 h and t=10.25 h to a sustained increase of 9 fA. Although this relaxation interval is too long to attribute to the circuit's frequency response, it is consistent with short-term annealing on the timescale of 10^2 s described in [56].

The top panel of Fig. III.20 shows six current pulses that are large enough to identify as fission fragment-induced ionization events. The bottom panel shows two current steps, one at t=37.5 h and one at t=37.85 h. These two current steps coincide with the two largest current pulses shown in the top panel. The other four large current pulses are not associated with current steps. The initial current step at t=37.5 h is 6 fA with a brief relaxation interval to a sustained increase of 4 fA. The 20 fA current step at t=37.85 h exhibits a pronounced relaxation interval as the net increase in reverse current is reduced to 15 fA. Fig. III.20 demonstrates that while current steps may occur in close temporal proximity to each other, not all fission fragment strikes cause discrete, sustained increases in reverse current.

Fig. III.21 displays a similar pattern to Fig. III.19; there is one current pulse associated with a fission fragment strike that coincides with a 12 fA current step at t=114.6 h. However, there is no clearly visible relaxation interval following the current step in the bottom panel of Fig. III.21. After 114 h of irradiation, the reverse current noise floor has increased to 240 fA, so the time series is noisy compared to the stable reverse current shown in Fig. III.19.

III.4 Analysis of Discrete Changes in Reverse Current

III.4.1 Identifying Current Pulses and Steps

Current pulses and steps similar to the examples shown in Figs. III.19 - III.21 can be identified with an algorithm that searches for exponentially decaying current spikes and abrupt, sustained increases in reverse current levels between particle strikes. Fig. III.22 shows the same time interval between hours 10 and 11 of irradiation as Fig. III.19 for a ^{252}Cf-irradiated dioe with drain floating. The y-axis is plotted on a log scale so that both current pulses and steps are clearly visible. The raw reverse current time series is shown in black. The dataset highlighted in red in Fig. III.22 represents the reverse current after applying a 500-point median filter to smooth the data. The filter replaces each raw reverse current reading with the median of all data points within a 75 s window centered on that reading. This filter suppresses the short-term behavior of current pulses while retaining the long-term behavior of current steps.

The current pulses marked with green circles in Fig. III.22 are identified in the raw reverse current data when two conditions are met. First, reverse current increases by at least 10 fA (or 4σ, where σ is the 1.5 fA standard deviation of pre-irradiation reverse current measured for 24 h) between readings $i-1$ and i. Second, the reverse current reading at $i+1$ has decreased to within $\pm 25\%$ of the value predicted by Equation III.2. If both of these conditions are met, a current pulse is recorded as the difference between reading i and reading $i-1$. Note that only current pulses 10 fA or larger are identified by this algorithm,

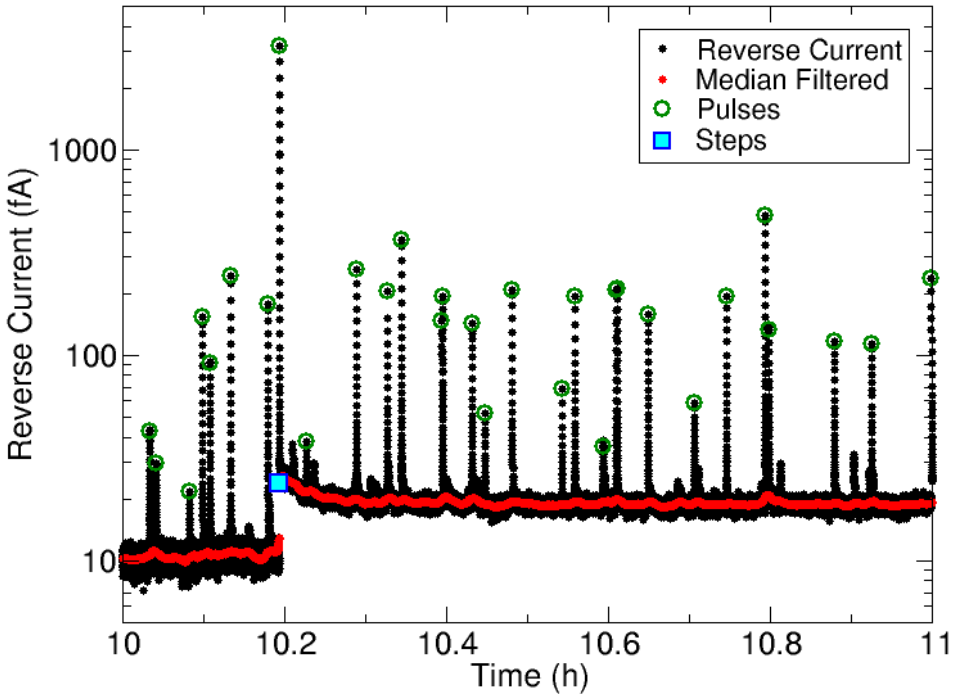

Figure III.22: One hour of reverse current time series (raw and median-filtered) for a ^{252}Cf -irradiated PAD1 diode under vacuum, after Auden *et al.*, 2012.

so pulses under this size limit are not marked with green circles in Fig. III.22. Since the current-to-voltage converter's output voltage is read every 150 ms, the measured pulse size may be as low as 75% of the actual current pulse caused by an ionization event, using the time-dependent voltage response for current pulses given in III.2.

The blue square denotes the current step identified at t = 10.2 h. Current steps are identified using the median-filtered reverse current data, since the short-term behavior is suppressed. A current step is identified when the median filtered reverse current value at reading i is more than 1.5 fA higher than the median filtered reverse current value at reading $i-1$. This algorithm only identifies steps larger than 1.5 fA, and it records the initial step size rather than the more stable step size that ensues following the relaxation interval of a few minutes.

III.4.2 Characterization of Current Steps and Pulses

Tables III.2 and III.3 compare the current pulses and steps identified in reverse current time series for six ^{252}Cf-irradiated diodes. The column labeled "Ion Threshold" in Table III.2 lists the current pulse heights used as thresholds to distinguish current pulses associated with heavy ions from those associated alpha particles in each time series. The ion thresholds range from 238 fA to 276 fA. Instead of using a common ion threshold for all six time series, the threshold for each time series was chosen to keep the ratio of particle strikes identified as heavy ions to those identified as alpha particles as close as possible to the 16:1 branching ratio expected for ^{252}Cf calculated in Section III.3 from decay process statistics reported in [51].

Although the observed current steps were temporally correlated only with current pulses an order of magnitude higher than the listed ion thresholds, establishing the number of heavy ion strikes is important for calculating damage factors and total fluence. Table III.2 also lists the total number of pulses identified as heavy ions ("Number of Incident Ions") and the fluence of heavy ions incident upon the surface area of each diode's depletion regions. Fluence is calculated as the total number of current pulses identified as heavy ions strikes divided by the cross-sectional area of the diode's depletion regions (3700 μm^2 for diodes with drain grounded and 2100 μm^2 for diodes with drain floating). Calculated fluence varies with the cross-sectional area of the depletion regions sensitive to ionization events, the distance between the ^{252}Cf source's active area and the diode's surface, and the total irradiation time.

Table III.3 lists information pertinent to long term increases in reverse current caused by displacement damage. The total increase in current listed for each irradiated diode is divided by the corresponding number of incident ions listed in Table III.2 to calculate the damage factors in the second column. The damage factor DF for the ^{252}Cf irradiated diodes is defined here as

$$DF = \frac{\Delta I_R}{N} \tag{III.5}$$

Diode	Ion Threshold (fA)	Number of Incident Ions	Fluence (cm^{-2})
Drain floating #1	280	235	1.1×10^7
Drain floating #2	280	294	1.4×10^7
Drain floating #3	257	228	1.1×10^7
Drain grounded #1	251	436	1.2×10^7
Drain grounded #2	273	1512	4.1×10^7
Drain grounded #3	239	1115	3.0×10^7

Table III.2: Ion threshold used to distinuguish heavy ions from alpha particles, number of current pulses associated with ion strikes, and fluence of incident ions for six ^{252}Cf-irradiated diodes.

Diode	Total Current Increase (fA)	Damage Factor (fA)	Number of Steps	Max. Step (fA)	Avg. Step (fA)	P(Step)
Drain floating #1	242	1.0	42	23.4	12.0	17.9%
Drain floating #2	417	1.4	48	81.8	19.6	16.3%
Drain floating #3	292	1.3	44	61.0	13.5	19.3%
Drain grounded #1	605	1.4	73	64.3	17.8	16.7%
Drain grounded #2	1826	1.2	140	90.4	22.7	9.3%
Drain grounded #3	1160	1.0	100	73.1	20.3	9.0%

Table III.3: Total current increase, damage factor, number of identified steps, maximum step size, average step size, and probability that an ion resulted in a measurable step for six ^{252}Cf-irradiated diodes.

where ΔI_R is the total change in reverse current during irradiation and N is the number of particles incident upon the diode's sensitive area [37]. Table III.3 also lists the number of identified steps larger than 1.5 fA, the maximum and average step sizes for each diode, and the probability that a heavy ion strike will produce a measurable current step. This probability is calculated as the number of steps divided by the number of incident ions. The probability that an incident ions will result in electrically active damage measured as a current step ranges from 16.3% to 19.3% for four diodes, but the probability of an ion producing a step is 9.3% and 9.0% in the two diodes labeled "Drain Grounded #2" and "Drain Grounded #3." These two diodes exhibited the highest total increase in reverse current, so a possible explanation for the lower probabilities of ion strikes resulting in a measurable step is that the increased noise floor may have obscured small steps so that the calculated ratio of measured steps to incident ions was too small.

As stated in Section III.3.1, the ^{241}Am-irradiated diode's reverse current increased by

60 fA after exposure to 3.2×10^4 incident alpha particles. Its damage factor is 1.9×10^{-3} fA/alpha particle. When the same diode was irradiated with ^{252}Cf in air, the reverse current magnitude increased by 35 pA after the device was struck by approximately 2×10^4 fission fragments (or 3×10^5 alpha particles). Its damage factor is 2 fA/fission fragment. Reverse current increased by 243 fA when the diode was struck by 2.0×10^2 incident fission fragments (or 3.3×10^3 alpha particles) for the diode irradiated with ^{252}Cf under vacuum as shown in Fig. III.13. Its damage factor is 1.0 fA/fission fragment. The ^{252}Cf-induced damage factors are of the same order as the damage coefficient (0.8 fAunit of fluence) reported for a ^{252}Cf irradiated diode in [37]. The average step size values listed in Table III.3, which corresponds to the average sizes of only those current steps identified by the algorithm, are 10 to 20 times bigger than the listed damage factors.

Table III.3 indicates that "Drain Grounded #2", the diode struck by the most ions during irradiation (1512 ions), exhibited both the largest total increase in reverse current at 1826 fA and the largest individual current step at 190 fA. "Drain Floating #1", which had the second lowest number of ion strikes at 235 ions, had both the smallest total increase in reverse current at 242 fA and the smallest current step at 23 fA. The average measured step size ranged from 12 fA to 23 fA for each of the reverse current time series. "Drain Grounded #2" had the largest average step size, and "Drain Floating #1" had the smallest average step size. This suggests a loose correlation between the largest observed step size and the number of ion strikes; the more ions that pass through a radiation-sensitive volume of a depletion region, the larger the maximum measured current step is likely to be. However, "Drain Floating #3" was struck by the smallest number of incident ions (228), but it exhibited a maximum current step of 61 fA, which is three times higher than the maximum current step of "Drain Floating #1".

The plot of step size versus pulse size shown in Fig. III.23 demonstrates that all current steps that are greater than 1.5 fA are associated with current pulses of a size consistent with fission fragment-induced ionization events. Fig. III.23 was generated by taking each iden-

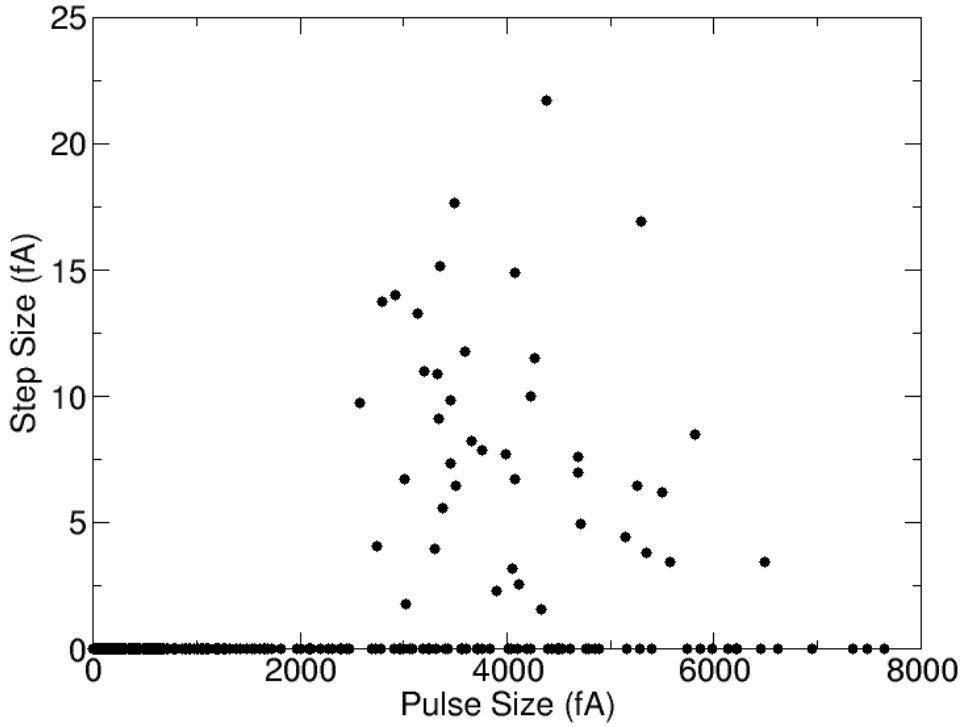

Figure III.23: Step size vs. pulse size for the reverse current time series for the diode labeled "Drain Floating #1" shown in Fig. III.13, after Auden *et al.*, 2012.

tified pulse's timestamp, finding the corresponding median-filtered reverse current reading, and subtracting the previous reading. All differences less than or equal to 1σ, or 1.5 fA, were assigned a step size of 0 fA. No alpha particles, in fact, no fission fragments associated with current pulses less than 2590 fA, corresponded to steps greater than 1.5 fA.

The five largest pulse sizes did not correspond to identified current steps, either. Pulse size was used in this analysis to separate fission fragment strikes from alpha particle strikes, since the LET of a particle, hence its energy deposition, is a very well defined function of the incoming ion species and energy. On the other hand, current steps are a result of atomic collisions. Ionization and atomic collisions are intrinsically uncorrelated, and the distribution of energy deposition caused by atomic collision events is very large. The result is that it is possible to have a wide range of damage production events, manifested as increases in reverse current, without a corresponding range of pulse heights.

Fig. III.24 shows the distribution of step sizes over time. After 118 h of radiation

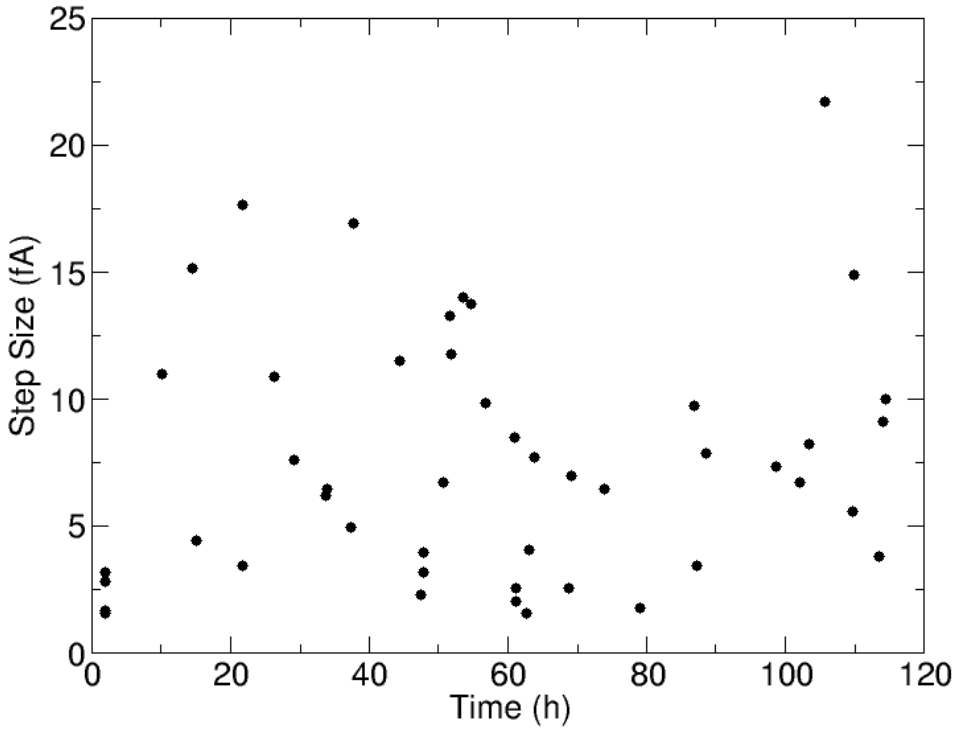

Figure III.24: Step size vs. time for the reverse current time series for the diode labeled "Drain Floating #1" shown in Fig. III.13, after Auden *et al.*, 2012.

exposure, the range of current step sizes remains constant across this period of irradiation. The largest current steps occur throughout the ^{252}Cf irradiation cycle even though the most damage has accrued at the end of the cycle. At a fluence of 7.0×10^7 particles/cm^2 (4.1×10^6 fission fragments/cm^2), the damage that can be created by individual particles is steady over time. The largest current steps do not cluster at the beginning of the irradiation cycle when little damage has occurred, nor do they cluster at the end of the irradiation cycle when the most damage has occurred.

Fig. III.25 shows an integral cross-section of heavy ion-induced current steps measured in the reverse current time series corresponding to six ^{252}Cf-irradiated JFET diodes shown in Figs. III.13 - III.18. The three datasets labeled "Drain Floating #1", "Drain Floating #2" and "Drain Floating #3" represent current step sizes in diodes with the drain unbonded, so the gate / epitaxial depletion region, gate / channel depletion region, and half of the epitaxial / substrate depletion region are sensitive to displacement damage. The integral

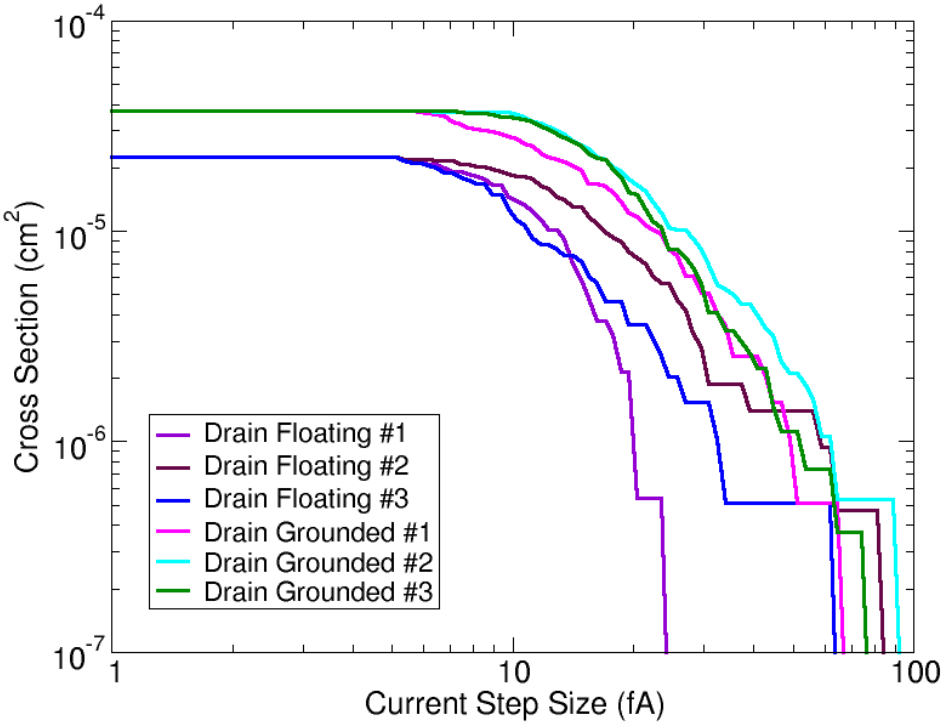

Figure III.25: Integral cross-section of current step sizes for six ^{252}Cf-irradiated JFET diodes. Three diodes were irradiated with the drain floating as in Fig. III.4, and three were irradiated with the drain grounded as in Fig. III.5.

cross-sections for these diodes cross the *y*-axis at 2100 μm^2, the sensitive cross-sectional area of the depletion regions. The three datasets labeled "Drain Grounded #1", "Drain Grounded #2" and "Drain Grounded #3" correspond to current steps measured in diodes with the drain pad bonded to the source pad. The gate / epitaxial depletion region, gate / channel depletion region, and the whole epitaxial / substrate depletion region are sensitive to displacement damage, so the integral cross-sections for these diodes cross the *y*-axis at 3700 μm^2, the cross-sectional area of the full substrate / epitaxial depletion regions. Current steps measuring at least 1.5 fA were binned by size for each diode, and the number of counts in each bin was divided by the corresponding fluence value from Table III.2. The shape of the size distribution of all six irradiated diodes is similar whether the drain is floating or grounded, so the size distribution does not depend on either the incident ion fluence or volume of the depletion region sensitive to the nonionizing radation.

Fig. III.26 shows a histogram of step sizes for all six irradiated diodes. The largest observed current step is visible at 91 fA, but most current steps cluster between 10 fA and 30 fA. The histogram also highlights useful information about the smallest observed current steps. Although the minimum current step that can be differentiated from background noise by the current-to-voltage converter is 1.5 fA, only one current step has been measured at 5 fA or less. The minimum current steps caused by damage from heavy ions are measured in the range of 6 fA to 10 fA. These current steps are assumed to be associated with heavy ions rather than alpha particles since the steps temporally correspond to pulse sizes too large to be alpha particles, as was shown in Fig. III.24. In addition, the reverse current time series measured during ^{241}Am irradiation (see Fig. III.12) exhibited no measurable current steps even though a thousand times more alpha particles struck the diode's active area during the ^{241}Am irradiation compared to the six ^{252}Cf irradiations analyzed in this section.

The integral cross-section of current pulse sizes for the six ^{252}Cf-irradiated diodes is shown in Fig. III.27. All six datasets show a sharp knee around 350 fA that is associated with the transition from pulses caused by alpha partices to the pulses caused by heavy ions. Once again, the integral cross-section datasets that correspond to "Drain Grounded" diodes cross the y-axis at 3700 μm^2, the cross-sectional area of the epitaxial / substrate depletion region under the drain, gate, and source regions. The datasets that correspond to "Drain Floating" diodes cross the y-axis at 2100 μm^2, the cross-sectional area of the epitaxial / substrate depletion region under the source and gate regions only. The division between current pulses associated with alpha particles and those associated with heavy ions is repeated in the histogram of pulse sizes shown in Fig. III.28. Most of the counts correspond to pulse sizes of less than 400 fA, and these pulses are attributed to alpha particles. The distribution of pulses sizes between 400 fA and 7200 fA are associated with the spectrum of light and heavy fission fragments emitted from ^{252}Cf.

Figs. III.29 and III.30 show post-irradiation current-voltage sweeps for the three diodes

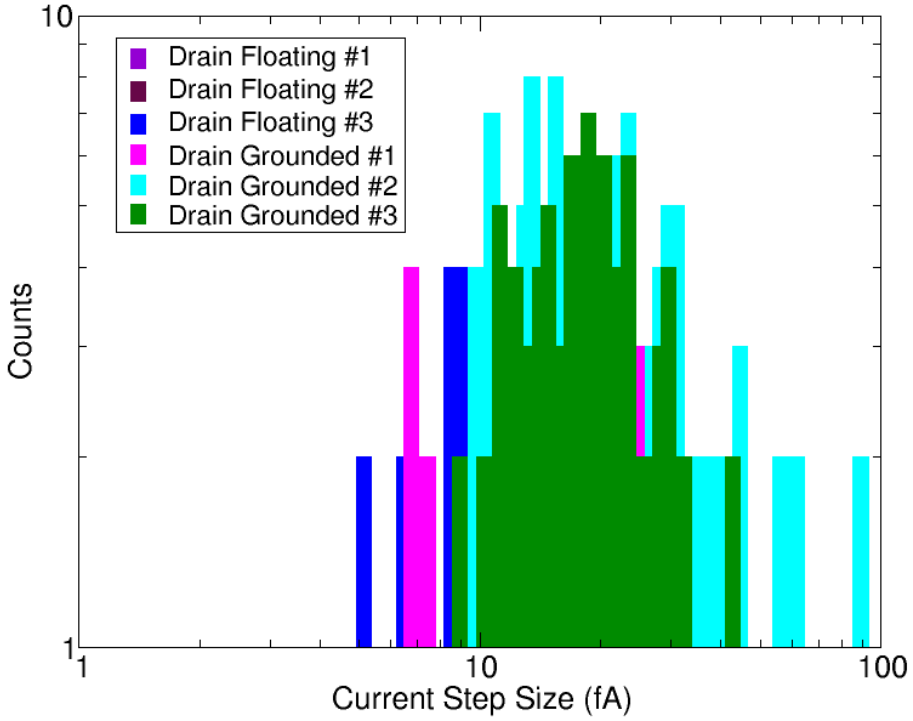

Figure III.26: Histogram of current step sizes for six ^{252}Cf-irradiated JFET diodes. Three diodes were irradiated with the drain floating as in Fig. III.4, and three were irradiated with the drain grounded as in Fig. III.5.

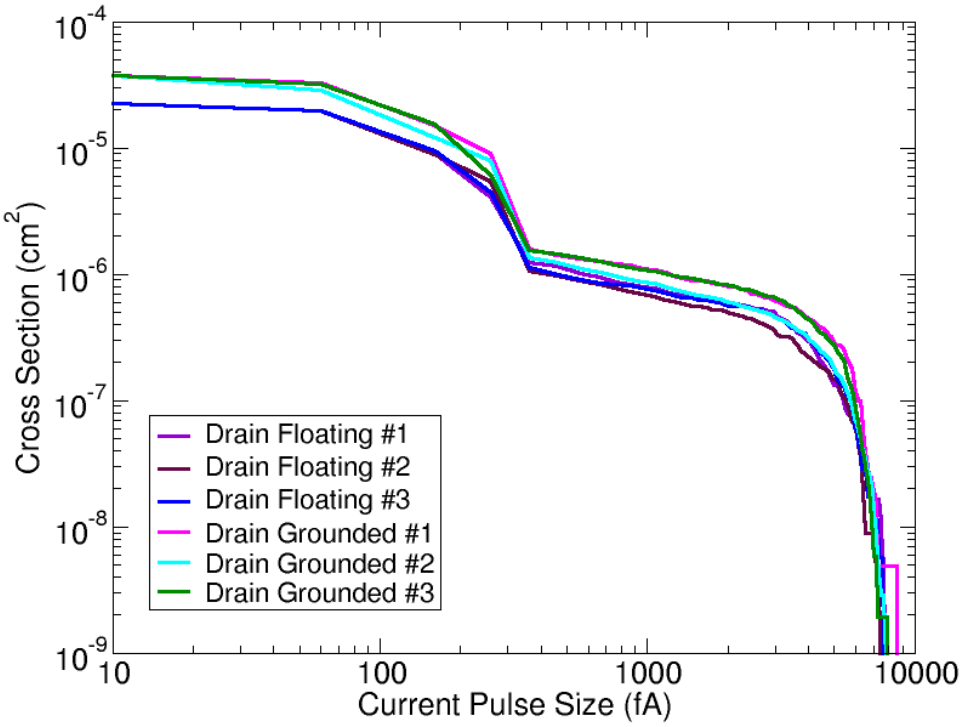

Figure III.27: Integral cross-section of current pulse sizes for six ^{252}Cf-irradiated JFET diodes. Three diodes were irradiated with the drain floating as in Fig. III.4, and three were irradiated with the drain grounded as in Fig. III.5.

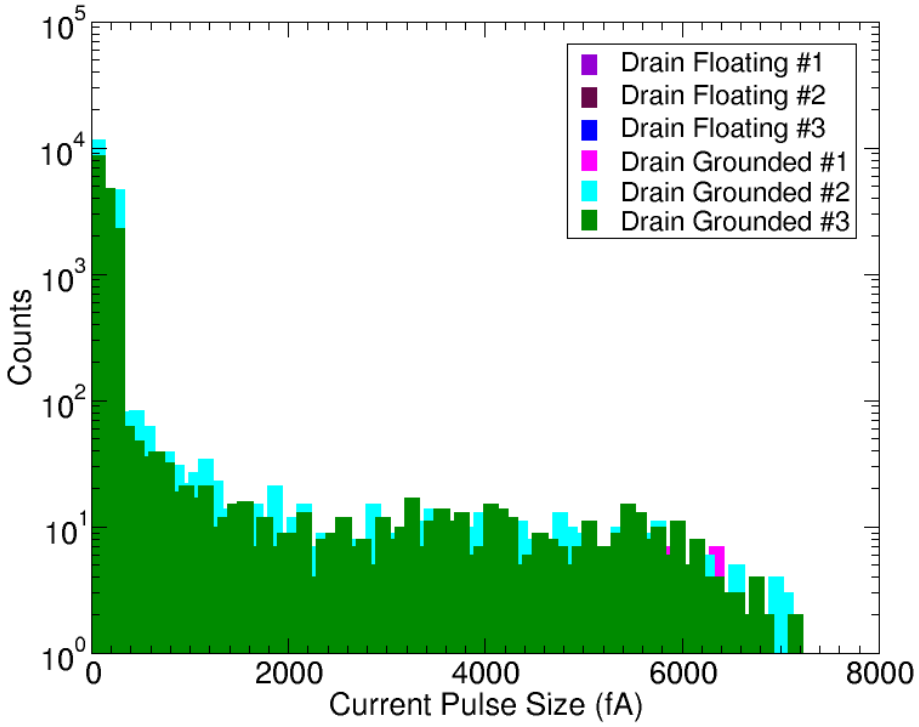

Figure III.28: Histogram of current pulse sizes for six ^{252}Cf-irradiated JFET diodes. Three diodes were irradiated with the drain floating as in Fig. III.4, and three were irradiated with the drain grounded as in Fig. III.5.

with drains grounded. The sweeps shown in Fig. III.29 were performed immediately after irradiation ended, and the sweeps shown in Fig. III.30 were performed 72 h later. All three diodes exhibit little reduction in reverse current magnitude after 72 h. Diodes 1 and 3 respectively exhibit a 2.8% and 3.5% reduction in reverse current magnitude after 3 days. Diode 2, the device that sustained the most ion strikes (1512 ions) and the largest increase in reverse current (1.8 pA), exhibited a 22% reduction in reverse current magnitude after 3 days. Although the annealing of displacement damage is expected to reduce the damage-induced change in reverse current by a factor of 5 in the first hour after damage occurs [4], the diodes reported in this work were irradiated for 5 to 7 days. Displacement damage caused by initial ion strikes had annealed for several days once exposure to the radiation source was stopped, and damage from the final ion strikes had annealed for several minutes. Reductions in reverse current magnitude on the order of 25% or less are reasonable for an irradiated device that has already undergone an annealing period of a few days [4].

While Figs. III.29 and III.30 demonstrate the minor amount of annealing that occurs over a 3 day period following irradiation, the plots of current *vs.* voltage also show as the magnitude of reverse bias is increased, depletion regions expand to encompass more damage-induced generation centers that contribute to reverse current. Electric field strength also increases with reverse bias, so depletion region generation centers become more effective at thermal carrier generation.

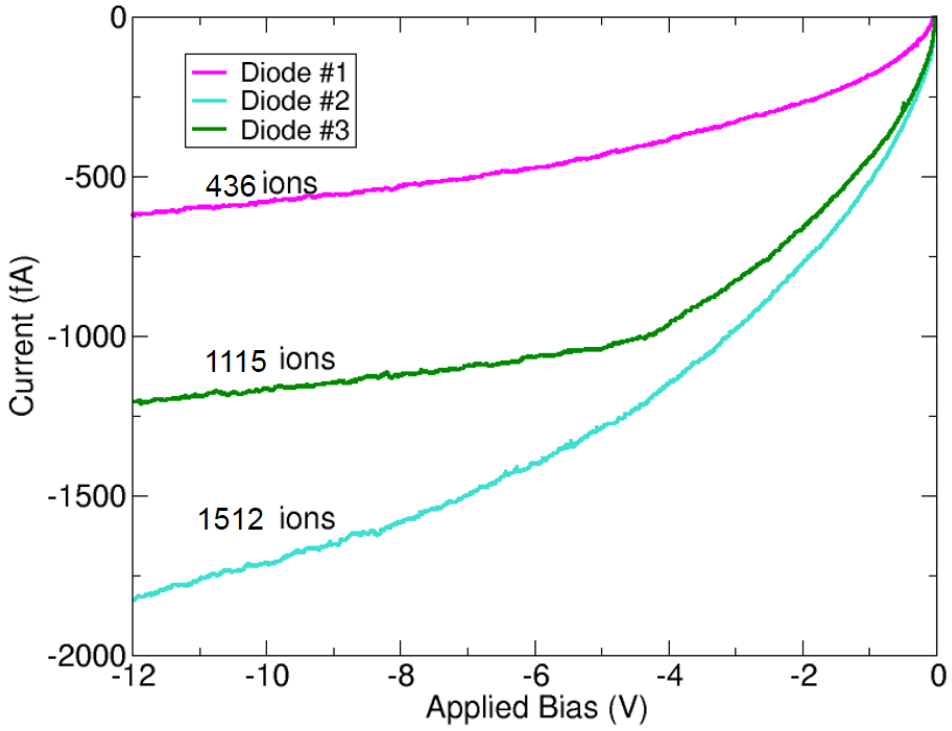

Figure III.29: Post-irradiation IV sweeps of ^{252}Cf-irradiated JFET diodes with drain grounded taken at room temperature (nominally 20° C) approximately 10 m after exposure to the ^{252}Cf source was stopped, after Auden *et al.*, 2013.

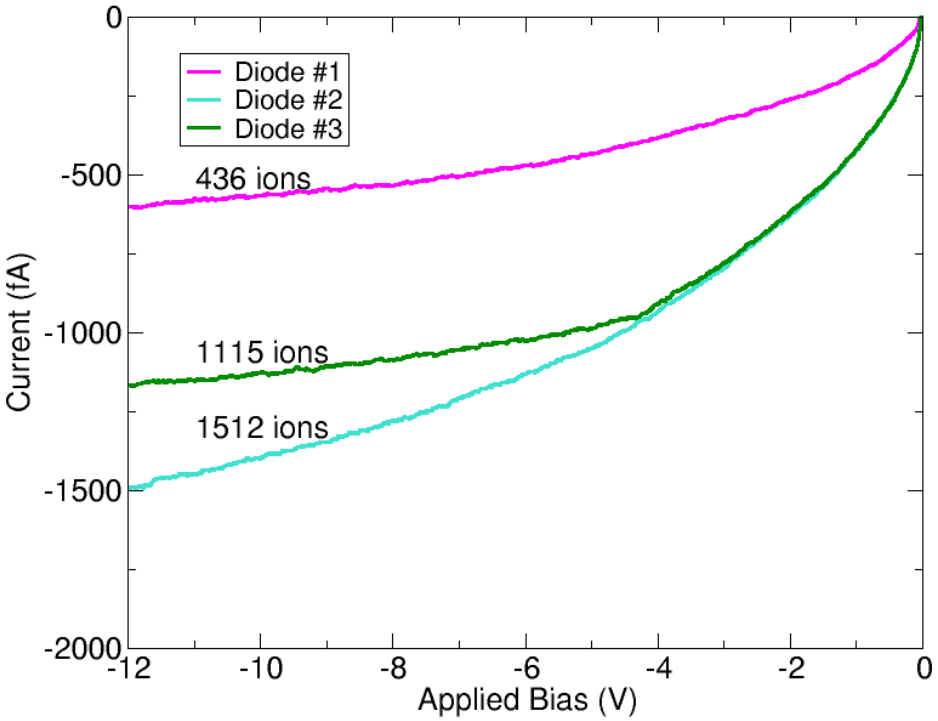

Figure III.30: Post-irradiation IV sweeps for three JFET diodes with drain grounded. For these sweeps, current voltage characteristics were swept three days after irradiation.

CHAPTER IV

Modeling Single Particle Displacement Damage

The reverse current time series and analyses presented in Chapter III demonstrate that discrete, sustained increases in reverse current can be observed when a reverse-biased diode's depletion region is struck by a single fission fragment. The average increase in reverse current per incident particle can be calculated with simulations of nonionizing energy loss, and this metric can be used to estimate the operational lifetime of a device operating in a given radiation environment. The radiation-induced electrical response of various irradiated devices has been shown to scale with NIEL [32], [57]. For example, NIEL values calculated with the Stopping Range of Ions in Matter (SRIM) code can be used to predict the average increase in dark current sustained by pixels in a CCD or CID array. Sections IV.1.1 and IV.1.2 discuss two methods for estimating experimental damage factors: comparing NIEL ratios for two incident particles and species and calculating the universal damage factor.

Calculating the average amount of electrical degradation per particle is of limited utility in determining another damage metric, the maximum amount of electrical degradation caused by a single particle. The ratio of the average increase in dark current associated with two different incident particle species or energies has no bearing on the ratio of the maximum individual increases in dark current associated with those different particles. For instance, the size of discrete increases in dark current that result in hot pixels does not correlate with NIEL [10]. Single particle displacement damage studies have shown differences between the ratios of maximum recoil energy to average recoil energy (obtained from calculations) and the maximum size of the resulting electrical effects to the average size of the electrical effects (obtained experimentally) [8], [9], [10]. Modeling the size distribution of current steps indicates the likelihood that a device will incur unacceptable degradation from a single particle strike, but it requires information about the arrangement

of device material layers, depletion region geometry, and electric field strength along with nonionizing energy simulations.

This chapter presents simulations of both the average amount of electrical degradation per incident particle observed in ^{252}Cf-irradiated JFET diodes (published in [16]) and the maximum amount of electrical degradation per incident particle (published in [33]).

IV.1 Modeling the Average Increase in Reverse Current

IV.1.1 NIEL

NIEL describes the nonionizing energy lost to the creation of phonons and vacancy / interstitial pairs as an incident radiation particle creates a wake of atomic displacements [19]. NIEL is calculated as

$$NIEL = \frac{N}{A} \int L[T(\Theta)] T(\Theta) \frac{d\sigma(\Theta)}{d\Omega} d\Omega \tag{IV.1}$$

where N is Avogadro's number, A is the target material's atomic weight, Θ is the recoil angle, $[T(\Theta)]$ is the recoil energy, $L[T(\Theta)]$ is the Lindhard partition fraction of total energy lost to nonionizing processes, and $d\sigma(\Theta)/d\Omega$ is the differential cross-section that an incident particle recoils into an incremental solid angle $d\Omega$ [6], [58]. As with linear energy transfer (LET), the metric used to estimate energy loss to ionizing processes, NIEL is calculated in units of MeV-cm^2 g^{-1}. NIEL estimates the average rate of displacement damage sustained for a given particle species and energy, so values calculated with SRIM can be used to estimate the overall increase in reverse current that a diode will sustain from displacement damage caused by a given fluence of radiation particles.

NIEL correlates well with experimental damage factors [6]. In [19], Marshall and Marshall note that the ratio of damage factors measured for different particle species and energies can be compared to the NIEL ratios of those particle species without a scaling factor. Fig. IV.1 shows the ratio of experimental damage factors calculated for the diode irradiated with ^{252}Cf labeled "Drain Floating #3" (damage factor = 1.2 fA / fission frag-

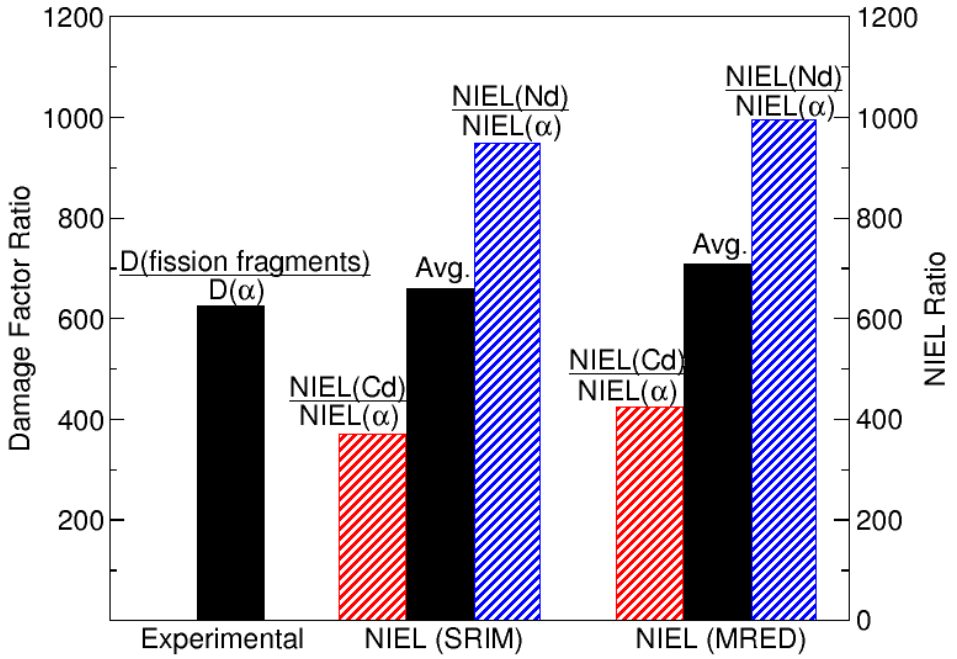

Figure IV.1: Ratio of damage factors (ΔI_R per incident fission fragment for a ^{252}Cf-irradiated diode to (ΔI_R per incident alpha particle for a ^{241}Am-irradiated diode) compared to the ratio of NIEL(106 MeV Cd) to NIEL(5.9 MeV α) as well as the ratio of NIEL(80 MeV Nd) to NIEL(5.9 MeV α), after Auden *et al.*, 2012.

ment) and the ^{241}Am-irradiated diode (1.9×10^{-3} fA / alpha particle). This ratio is labeled "fission fragments / α." The experimental damage factor ratio is compared to the ratio of NIEL(106 MeV Cd) with NIEL(5.9 MeV α). It is also compared to the ratio of NIEL(80 MeV Nd) with NIEL(5.9 MeV α).

The averages of the NIEL ratios for Cd to alpha particles and Nd to alpha particles are also shown in Fig. IV.1 as bars labeled "Avg." since, as Fig. III.11 shows, ^{252}Cf emits equal numbers of light and heavy fission fragments. NIEL was calculated with SRIM using the method described by Messenger *et al.* in [32] and also with the Monte Carlo Radiative Energy Deposition (MRED) code using the nonionizing energy deposition rate described by Weller *et al.* in [59]. MRED is a radiation transport code based on Geant4 particle physics libraries [60], [61]. Both the MRED and SRIM simulations were performed with a device structure modeled as a simple silicon wafer. The depletion region was modeled as

a 1 μ m thick sensitive volume with an area of 5000 μm^2 located 1 μm under the surface of the silicon.

The ratio of experimental damage factors is within 12% of the average NIEL ratio calculated using MRED, and it is within 6% of the average NIEL ratio calculated using SRIM. Even though the largest measured current step was 18 times larger than the average increase in reverse current indicated by the fission fragment damage factor, the ratio of NIEL associated with fission fragments to NIEL associated with alpha particles is in good agreement with the ratio of damage factors associated with fission fragments and alpha particles. All six ^{252}Cf-irradiated diodes exhibited damage factors within 0.1 fA to 0.2 fA of the damage factor used in Fig. IV.1, so NIEL can calculate the average increase in reverse current per ion independent of the displacement-damage sensitive volume of the depletion region that varies as the drain is grounded or left floating.

As the ratio of experimental damage factors indicates, the average fission fragment associated with ^{252}Cf decays causes $\tilde{6}$30 times more damage than the average alpha particle. ^{252}Cf fission decays produce 2 fission fragments [51] and an average of 3.5 neutrons (average energy of 2.1 MeV) [62]. MRED simulations show that the cross-section for depositing a given amount of energy in atomic displacements is six orders of magnitude smaller for 2.1 MeV neutrons than it is for fission fragments. The electrical effects of neutron-induced displacement damage are thus insignificant compared to fission fragment-induced damage in ^{252}Cf-irradiated silicon.

However, because NIEL calculates the average nonionizing energy lost as a particle travels through a given material, it does not indicate the amount of damage caused by the rare particle that deposits excessive nonionizing energy. For instance, the largest single particle damage events reported in [10] did not scale with NIEL. Furthermore, since NIEL calculations focus on the creation of vacancy interstitial pairs and do not include information about the effect of local electric field strength on defect emission rates, NIEL does not provide information about the maximum size of displacement damage-induced current

steps when high electric fields are present.

IV.1.2 Universal Damage Factor

In 2000, Srour and Lo presented the universal damage factor as a means of comparing the average amount of electrical damage per particle independently of device type and incident particle [4]. The universal damage factor K_{dark} is defined as the increase in the thermal carrier generation rate per unit of displacement damage dose D_d in a depletion region, where displacement damage dose can be calculated as fluence$\times$NIEL.

The value of K_{dark} for the JFET diodes with drains floating and grounded is approximately 4×10^7 carriers cm^{-3} s^{-1} per particle cm^{-2}. Fig. IV.2 shows this value of K_{dark} as a red circle plotted on a graph of $K_{dark}\times$NIEL vs. NIEL along with 42 other irradiated devices reported in reported in [4], and it is in good agreement with the heavy ion irradiated devices in this figure. The K_{dark} values calculated for the diodes in this work used the MRED NIEL values calculated for Fig. IV.1.

Universal damage factor values for the original 42 silicon devices reported in [4] were calculated for dark current data normalized to 1 week post-irradiation. As stated in Section III.4.2, the diodes in this work were irradiated for 5 to 7 days, so the accumulated heavy ion-induced displacement damage had already annealed for a period of several minutes to several days. Therefore, no further normalization for annealing was applied to the reverse current data used to calculate the universal damage factors for the diodes reported in this work that are represented by the red circle in Fig. IV.2.

IV.2 Modeling the Maximum Discrete Increase in Reverse Current

The good agreement shown between published K_{dark} values for devices irradiated with heavy ions and the K_{dark} values calculated with MRED values of NIEL for the ^{252}Cf-irradiated diodes investigated in this work show that MRED simulations of nonionizing energy deposition can correctly predict the average increase in reverse current per incident ion. This result is underscored with the agreement shown between the ratios of experimen-

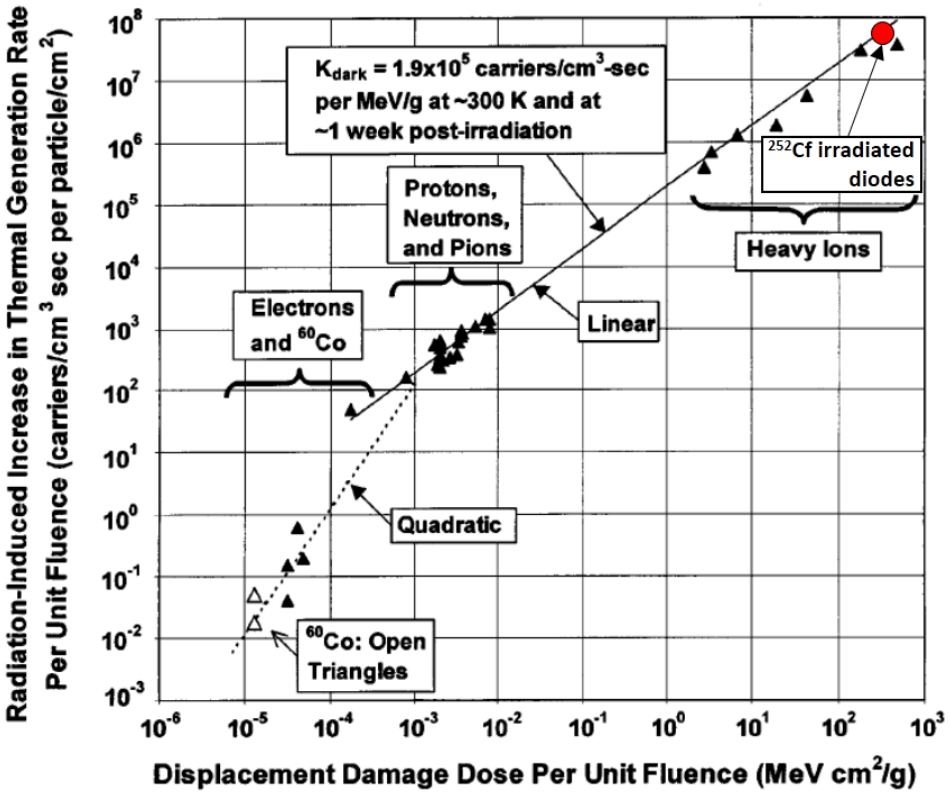

Figure IV.2: $K_{dark}\times$NIEL vs. NIEL for devices irradiated with photons, electrons, protons, and heavy ions, after Srour and Lo, 2000. The K_{dark} value calculated for ^{252}Cf-irradiated JFET diodes is shown as the red circle.

tal damage factors for ^{241}Am and ^{252}Cf-irradiated diodes and NIEL ratios for heavy ions and alpha particles calculated with both SRIM and MRED. MRED can predict the size of the average damage event, and the remainder of this chapter will show that MRED can also predict the size distribution of damage events.

In Section III.4.2, the size distributions of heavy ion-induced current steps in ^{252}Cf-irradiated JFET diodes showed that the maximum current steps measured for each diode are 2 to 4 times larger than the average measured current steps, and the maximum measured steps are 23 to 82 times larger than the corresponding damage factors. Calculations of NIEL and the universal damage factor K_{dark} in Section IV.1 estimate values for the average increase in reverse current per particle that show good agreement with experimental values. This section uses MRED and TCAD simulations to model the expected size distribution of current steps in ^{252}Cf-irradiated diodes. MRED simulations of nonionizing energy deposition and atomic displacements are used to calculate the radiation-induced increase in defect density that reduces minority carrier lifetime. TCAD simulations of electric field strengths within the depletion regions are used to calculate reductions in the Coulomb barrier height that enhance defect emission rates and decrease generation lifetime.

IV.2.1 MRED Simulations of Increased Defect Density for Minority Carrier Lifetime

MRED simulations of nonionizing energy deposition can be used to predict the average amount of damage caused by incident particles as shown in Section IV.1.1. However, MRED can be used to calculate additional physical parameters, such as the number of secondary displacements caused by the incident particle and subsequent knock-on atoms. MRED can track the isotopes of atoms that have been displaced within a structure, and it can also calculate the distance between displacements. Figs. IV.4 and IV.3 show the JFET diode structure (with drain floating and grounded, respectively) simulated with MRED. Depletion regions are shown as solid blocks, and material layers are represented with a

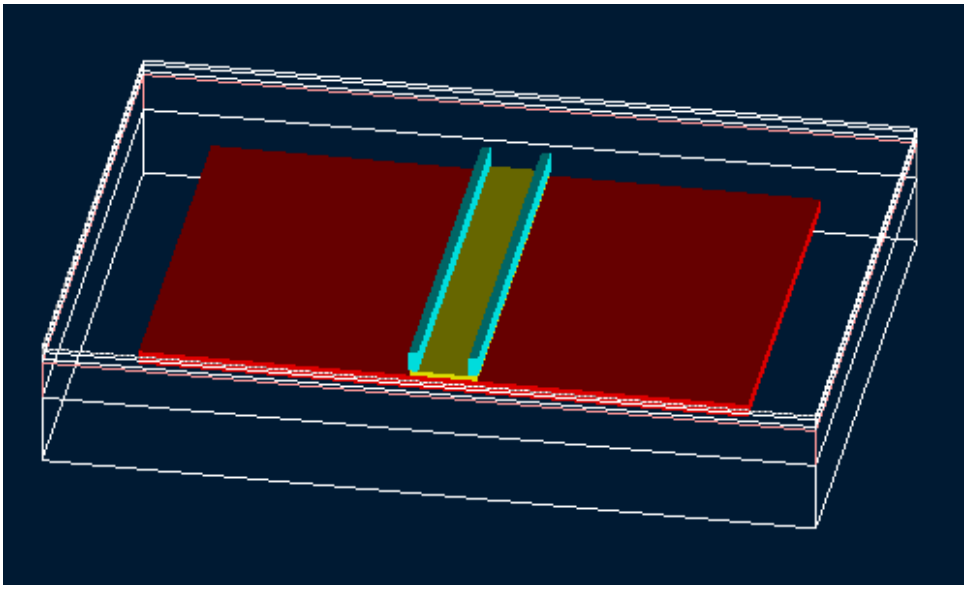

Figure IV.3: MRED model of JFET diode with drain grounded, after Auden *et al.*, 2013. Material layers are shown as wireframes, and depletion regions are shown as solid colors.

wireframe structure.

Figs. IV.5 and IV.6 show an integral cross-section and a histogram of nonionizing energy deposition by four different particle species and energies in the sensitive volumes represented by the red, yellow, and cyan shading in the model of a JFET diode with drain grounded shown in Fig. IV.3. The datasets in Figs. IV.5 and IV.6 represent typical emission byproducts of ^{252}Cf: 80 MeV Nd, 106 MeV Cd, 5.9 MeV alpha particles, and 2.0 MeV neutrons [53], [54]. The cross-section values on the y-axis indicate the likelihood that an incident particle will deposit energy equal to or exceeding the corresponding amount of energy shown on the x-axis [63], and for small values of deposited energy asymptotically approach the device's geometric area. Figs. IV.7 and IV.8 pertain to nonionizing energy deposition by ^{252}Cf emission products when the diode is floating (as shown in Fig. IV.4) so that the epitaxial / substrate depletion region is roughly half the volume it is when the drain is grounded.

As discussed in Section I, experimental damage factors scale linearly with NIEL, even though NIEL incorporates atomic displacements without accounting for complex defect

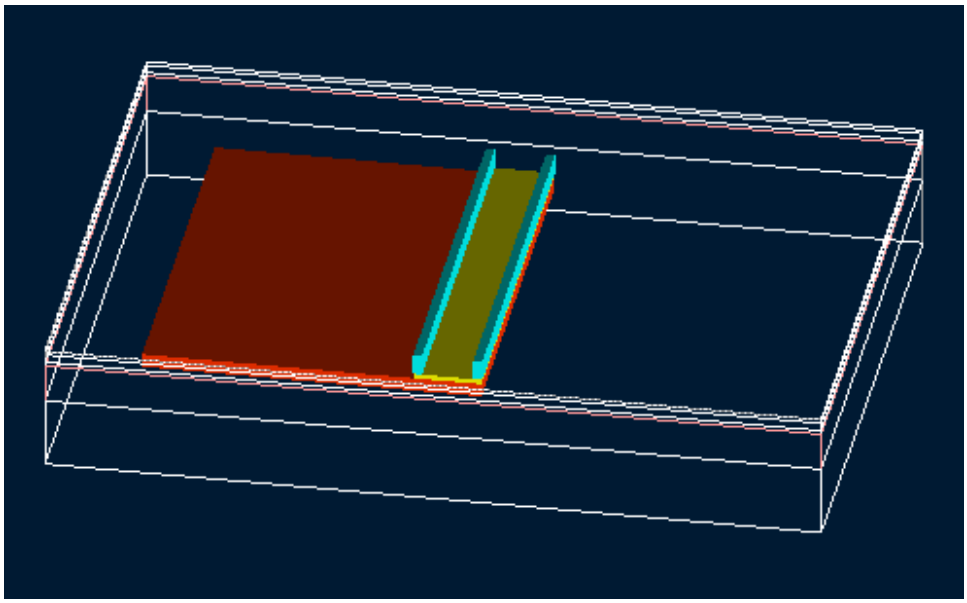

Figure IV.4: MRED model of JFET diode with drain floating. Material layers are shown as wireframes, and depletion regions are shown as solid colors.

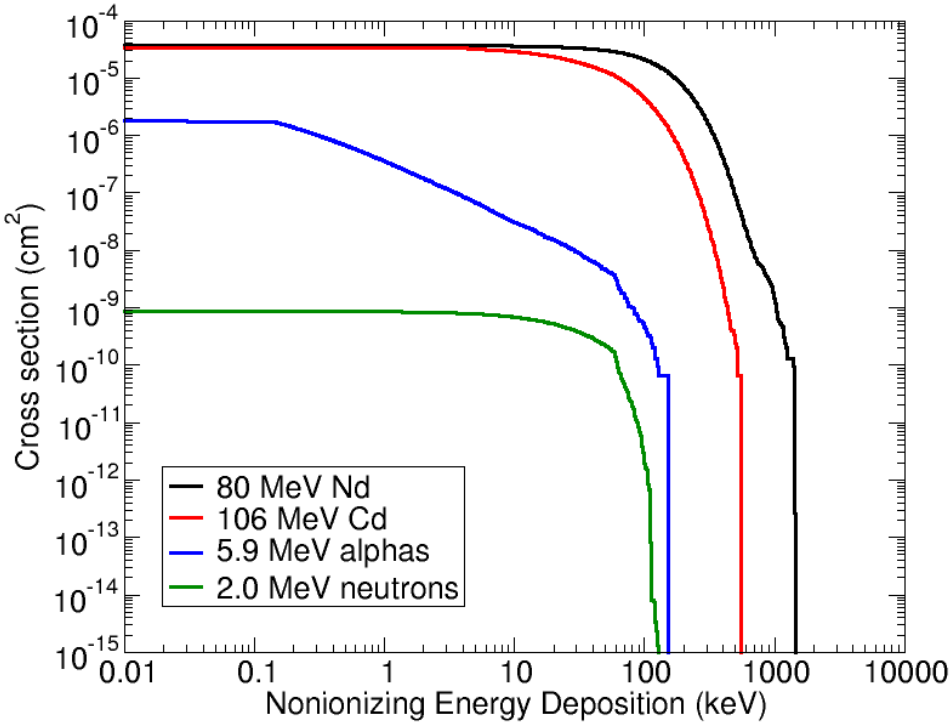

Figure IV.5: Integral cross-section of nonionizing energy deposited by typical ^{252}Cf fission fragments, alpha particles, and neutrons in a JFET diode with drain grounded.

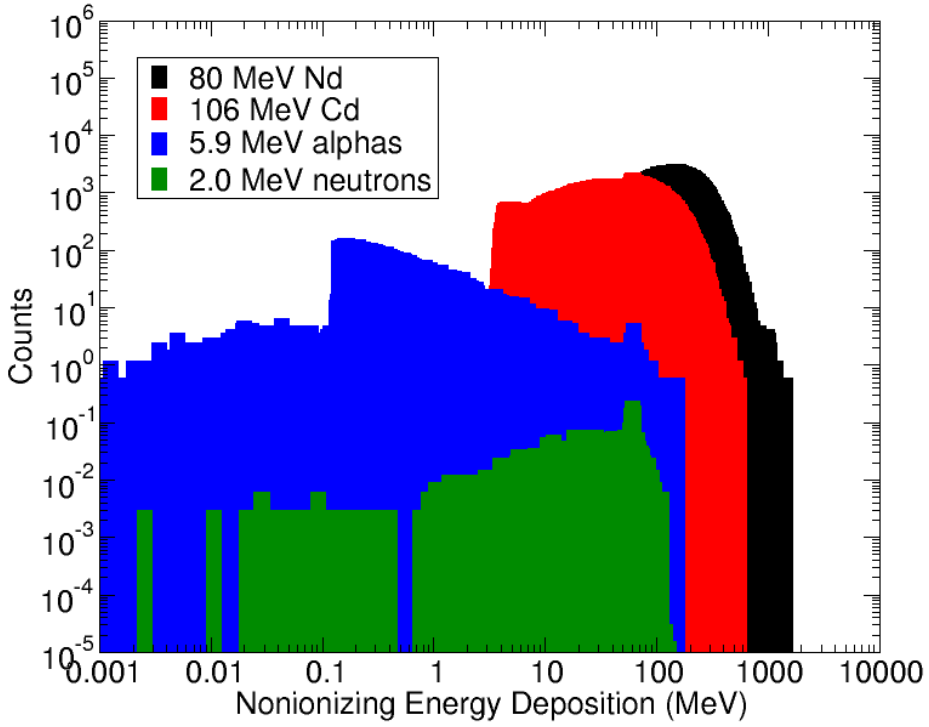

Figure IV.6: Histogram of nonionizing energy deposited by typical ^{252}Cf fission fragments, alpha particles, and neutrons in a JFET diode with drain grounded.

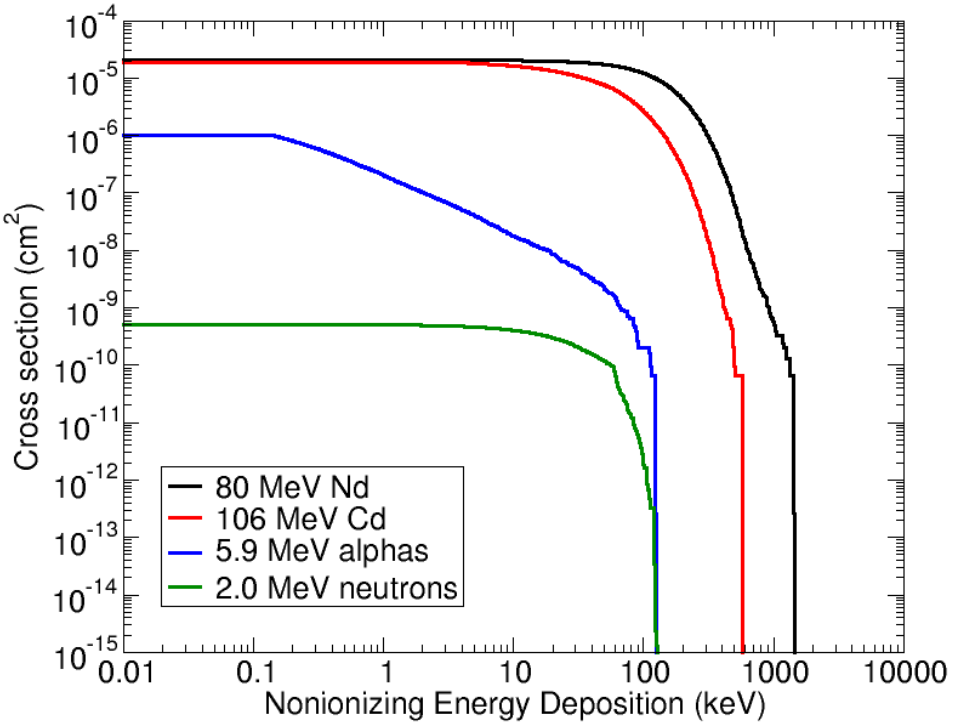

Figure IV.7: Integral cross-section of nonionizing energy deposited by typical ^{252}Cf fission fragments, alpha particles, and neutrons in a JFET diode with drain floating.

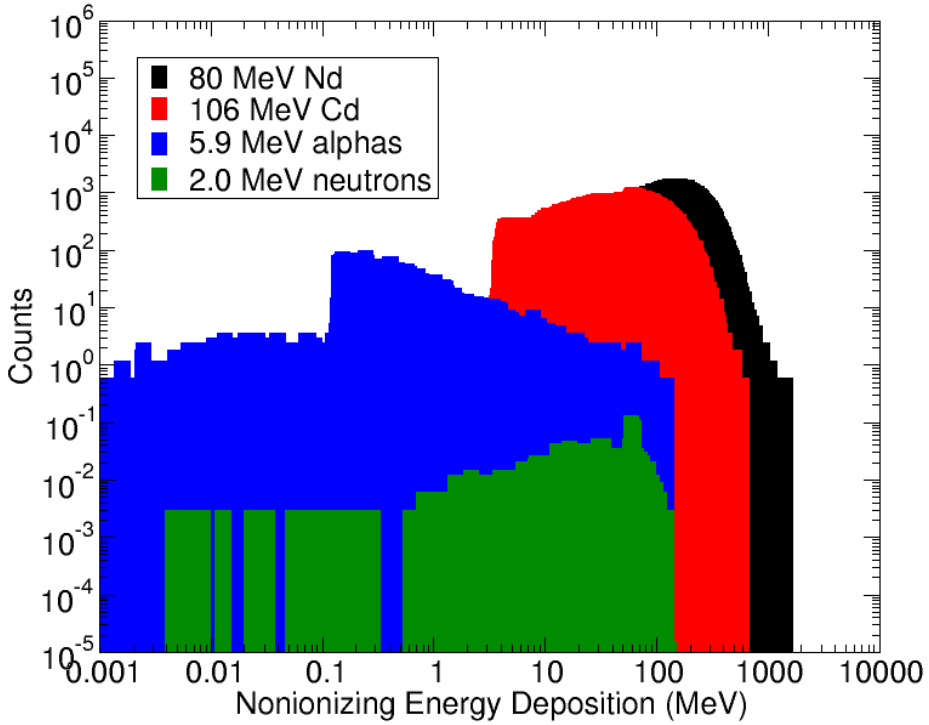

Figure IV.8: Histogram of nonionizing energy deposited by typical ^{252}Cf fission fragments, alpha particles, and neutrons in a JFET diode with drain floating.

structures or time-dependent annealing. The method reported in [32] for calculating NIEL from TRIM simulations finds the average numbers of vacancies and recoil atoms produced by incident particles. In this work, the numbers of vacancies and knock-on atoms that stop inside depletion regions are modeled using MRED. Knock-on atoms are atoms that have been displaced from the semiconductor lattice by incident particles or by other displaced atoms that traverse the material before stopping.

MRED can track the trajectories of all knock-on atoms displaced by each incident particle along with nonionizing energy deposition. If a knock-on atom is displaced from a location within a device depletion region, then the location of displacement is counted as a vacancy. If a knock-on atom (primary, secondary, tertiary, and so forth) stops inside a device depletion region, that stopped atom is counted as an interstitial. The total number of vacancies and interstitials created by one incident particle are substituted for N'_{vac} and N'_{int} in the equations for minority carrier lifetime (II.6) and generation lifetime (II.7). The av-

erage displacement evergy for single vacancy production has been reported as 21 eV [64], although the authors comment that a lower threshold of 12-13 eV as reported in [65] may be more appropriate for the multiple close-proximity atomic displacements that result in defect clusters. Recent molecular dynamics simulations have calculated an average displacement energy of 6.25 eV per atom in localized, highly disordered regions [66]. However, NIEL calculations that successfully predict the average amount of displacement damage-induced electrical degradation [6], [32] use 21 eV as the threshold energy for atomic displacements in silicon, so the 21 eV displacement threshold is also used here for the MRED simulations that use the modified Kinchin-Pease expression [67] in binary collision calculations.

Fig. IV.9 shows the number of interstitials as a function of nonionizing energy deposited by 80 MeV Nd and 106 MeV Cd, two typical light and heavy fission fragments emitted by ^{252}Cf [53], in the depletion regions of the MRED device structure shown in Fig. IV.3. Interstitial production scales linearly with nonionizing energy deposition; both 80 MeV Nd and 106 MeV Cd ions produce ˜1600 interstitials per MeV of nonionizing energy. Fig. IV.10 shows that vacancy production exhibits the same linear relationship with nonionizing energy of ˜1600 vacancies per MeV. The number of atomic displacements varies with the collison processes involved. For example, the damage cascade following a nuclear recoil will involve more secondary knock-on atoms than the damage caused by Rutherford scattering [2], and MRED simulations incorporate these processes.

The numbers of vacancies and interstitials *that contribute to reverse current* also vary with trajectory of the incident particle as it traverses the device. An incident ion that strikes the device at normal incidence in the gate region will displace atoms as it travels through the device, and all vacancies and interstitials produced in the gate / epitaxial depletion region, gate / channel depletion region, and epitaxial / substrate depletion region will contribute to N'_{vac} and N'_{int}. An incident ion that strikes the device at normal incidence between the source and the gate may displace a similar number of atoms as it travels through the quasi-neutral region into the epitaxial / substrate depletion region, but only the vacancies and interstitials

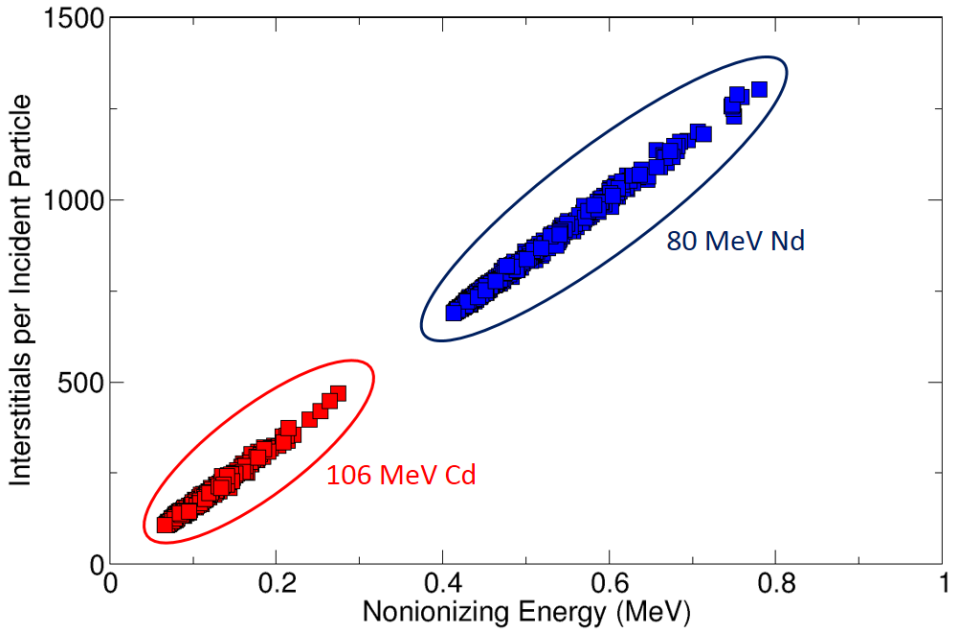

Figure IV.9: Interstitials vs. nonionizing energy deposition in depletion regions shown in Fig. IV.3 from MRED simulations of 80 MeV Nd and 106 MeV Cd ions, typical light and heavy ^{252}Cf fission fragments, after Auden *et al.*, 2013. Interstitials are modeled as knock-on atoms that stop inside a depletion region.

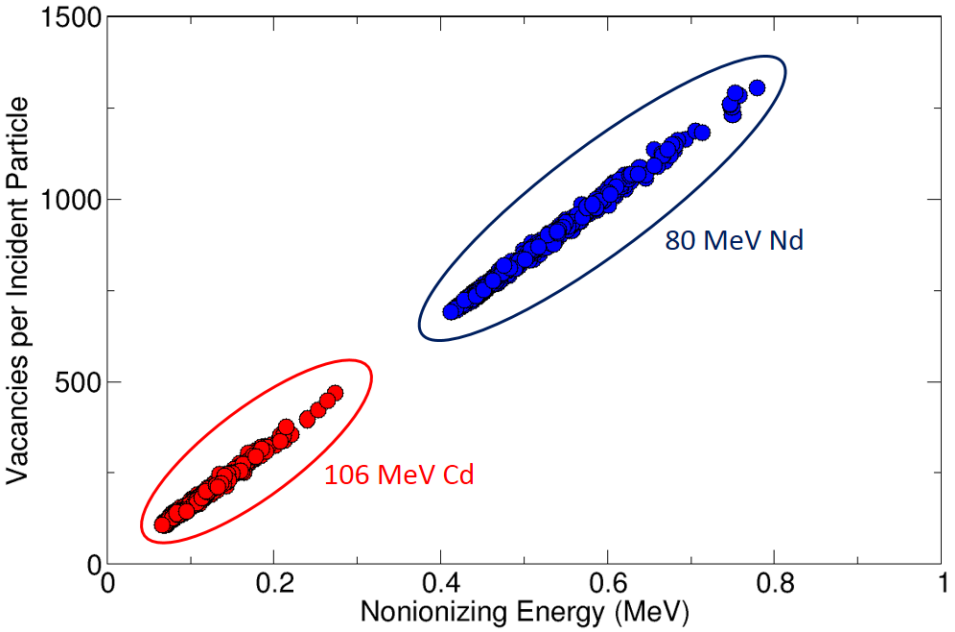

Figure IV.10: Vacancies vs. nonionizing energy deposition in depletion regions shown in Fig. IV.3 from MRED simulations of 80 MeV Nd and 106 MeV Cd ions, typical light and heavy ^{252}Cf fission fragments, after Auden *et al.*, 2013. Vacancies are modeled as the locations where knock-on atoms are displaced from the lattice.

produced in the epitaxial / substrate region will contribute to N'_{vac} and N'_{int}. Increased defect density depends on both collision processes and depletion region geometry.

Fig. IV.11 shows a cartoon of the depletion regions surrounding the $p+$ gate of the JFET diode modeled as the MRED structure in Fig. IV.4. In both figures, the gate / epitaxial depletion region is represented in cyan, the gate / channel depletion region is represented in yellow, and the epitaxial / substrate depletion region is represented in red. White areas in Fig. IV.11 represent quasi-neutral regions. Existing pre-irradiation defects are shown as unfilled circles, and new defects introduced by a single incident particle are represented as filled circles. Both the pre-irradiation and post-irradiation defects inside all three depletion regions contribute to reverse current through thermal carrier generation. As discussed in Section II.2.4, defects located in quasi-neutral regions are not included in calculations of reverse current since the contribution of radiation-induced increases in diffusion current are very small compared to depletion region generation current at room temperature [34].

IV.2.2 TCAD Simulations of Electric Fields for Generation Lifetime

In [9], [10], and [68], the authors reported that more generation current is produced by single particle displacement damage in portions of the depletion region exhibiting electric field strengths equal to 10^5 V/cm or higher compared to low electric field volumes within the depletion region. Deep-level defects created in high electric field regions exhibit higher thermal emission rates than the same defect structures in low electric field regions [27], [28]. Electric field-enhanced thermal emission mechanisms, such as phonon-assisted tunneling and the Poole-Frenkel effect, have been used to explain extreme device responses to single-particle effects [9]. Srour and Hartmann describe displacement damage enhancement as the enhanced thermal emission rates that contribute to the size of the current steps produced by extreme damage events in high electric field regions [9].

TCAD simulations were used to obtain the electric field distributions in the diodes discussed in the previous section. The device is modeled with the PAD1 JFET diode materials

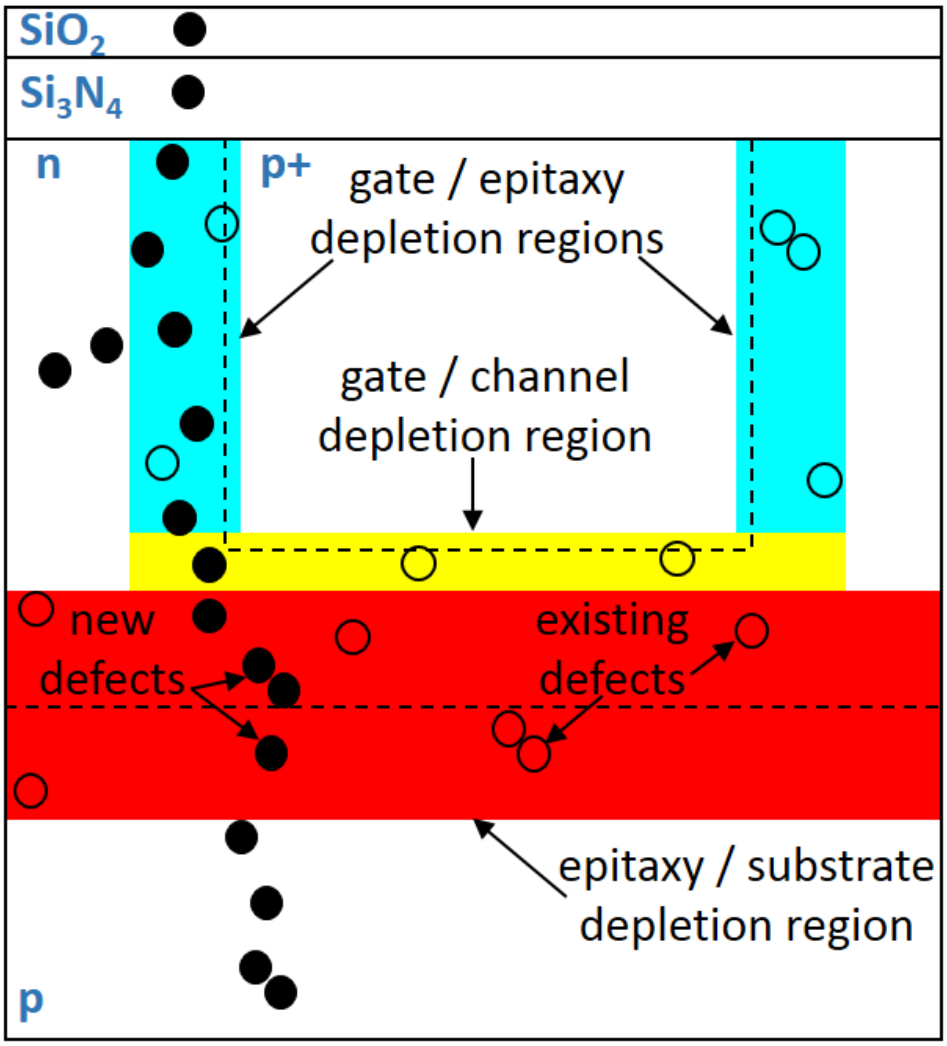

Figure IV.11: Cartoon of depletion regions around the gate of a reverse-biased JFET diode, after Auden *et al.*, 2013. Pre-irradiation defects are shown as unfilled circles, and new defects introduced by a radiation particle are shown as filled circles. Only the defects within depletion regions contribute to reverse current.

and doping parameters described in Section III.1.1. The *p*-type gate and *p*-type substrate are biased at -12 V with the *n*+ source grounded. Fig. IV.12 shows the electric field magnitude as a function of position when the *n*+ drain is floating, and Fig. IV.13 shows the electric field magnitude as a function of position when the drain is grounded. Both TCAD electric field plots are shown next to the peak current maps obtained with laser testing data (described in Section III.1.2) to compare the field strength of radiation-sensitive depletion regions.

Fig. IV.12 and Fig. IV.13 show that the electric field strength is at least 7×10^4 Vcm throughout most of the gate / epitaxial, gate / channel, and epitaxial / substrate depletion regions. The Poole-Frenkel effect contributes to enhanced emission rates in these regions by lowering the Coulomb barrier of defect activation energy [28], so that less thermal energy is required for a defect to emit an electron to the conduction band or a hole to the valence band. Both figures also show that the electric field in the gate epitaxial depletion region reaches 2×10^5V/cm.

IV.2.3 Size Distribution of Modeled Current Steps

Fig. IV.14 shows an integral cross-section of current steps measured in three ^{252}Cf-irradiated JFET diodes reverse-biased at -12 V and current steps modeled with (II.17). The vacancies N'_{vac} and interstitials N'_{int} created by individual 106 MeV Cd and 80 MeV Nd ions were tallied for each of the depletion regions shown in Fig. IV.3, and these values were used to calculate the post-irradiation electron and hole minority carrier lifetimes in (II.6) and (II.7). The reductions in thermal activation energy for electrons $\delta E_{act,n}$ and holes $\delta E_{act,p}$ in each depletion region were calculated from the average electric field strength $\mathcal{E}$ present in that depletion region from the TCAD electric field simulation shown in Fig. IV.13. The values for $\delta E_{actn,p}$ were used to calculate the generation lifetimes $\tau_{g0}(\mathcal{E})$ and $\tau_g(\mathcal{E})$. The total increase in reverse current for one incident ion was calculated as the sum of ΔI_R in all depletion regions.

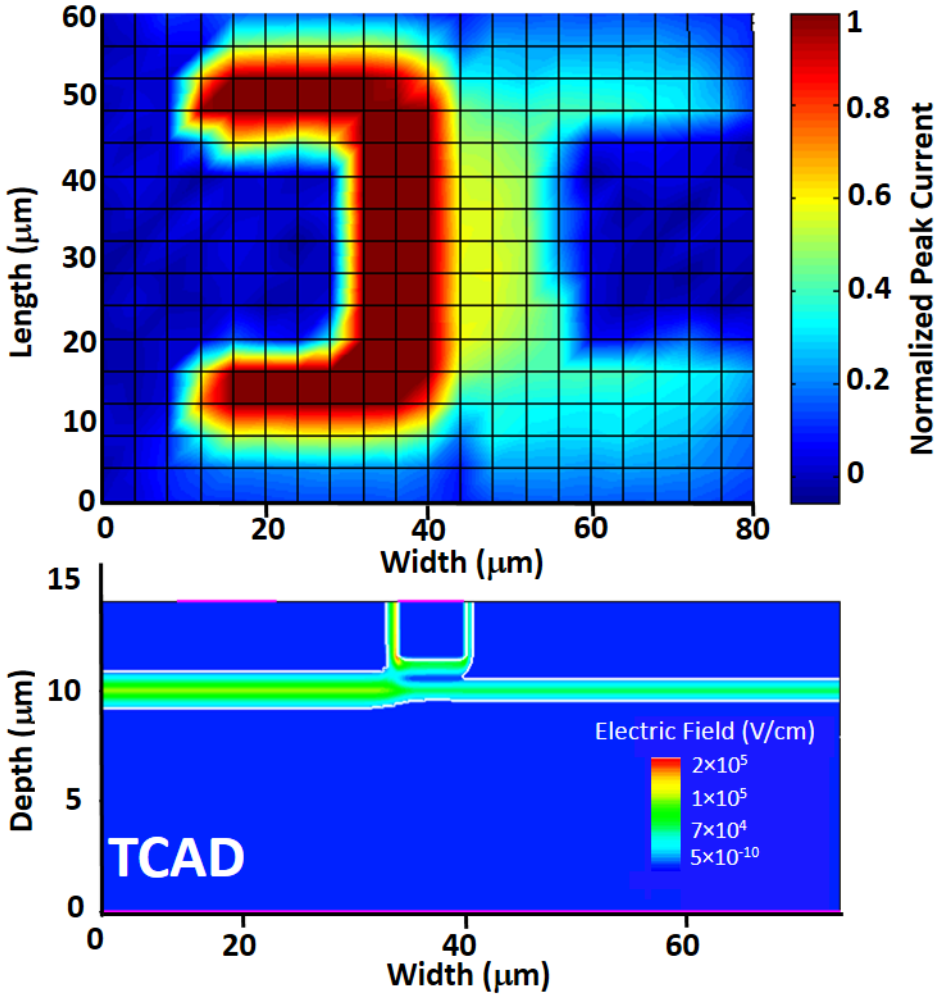

Figure IV.12: Peak current map generated with laser testing (top) and a 2-D TCAD electric field simulation (center) that indicate the geometry of depletion that are sensitive to charge generation in a reverse-biased JFET diode with drain floating, after Auden *et al.*, 2013.

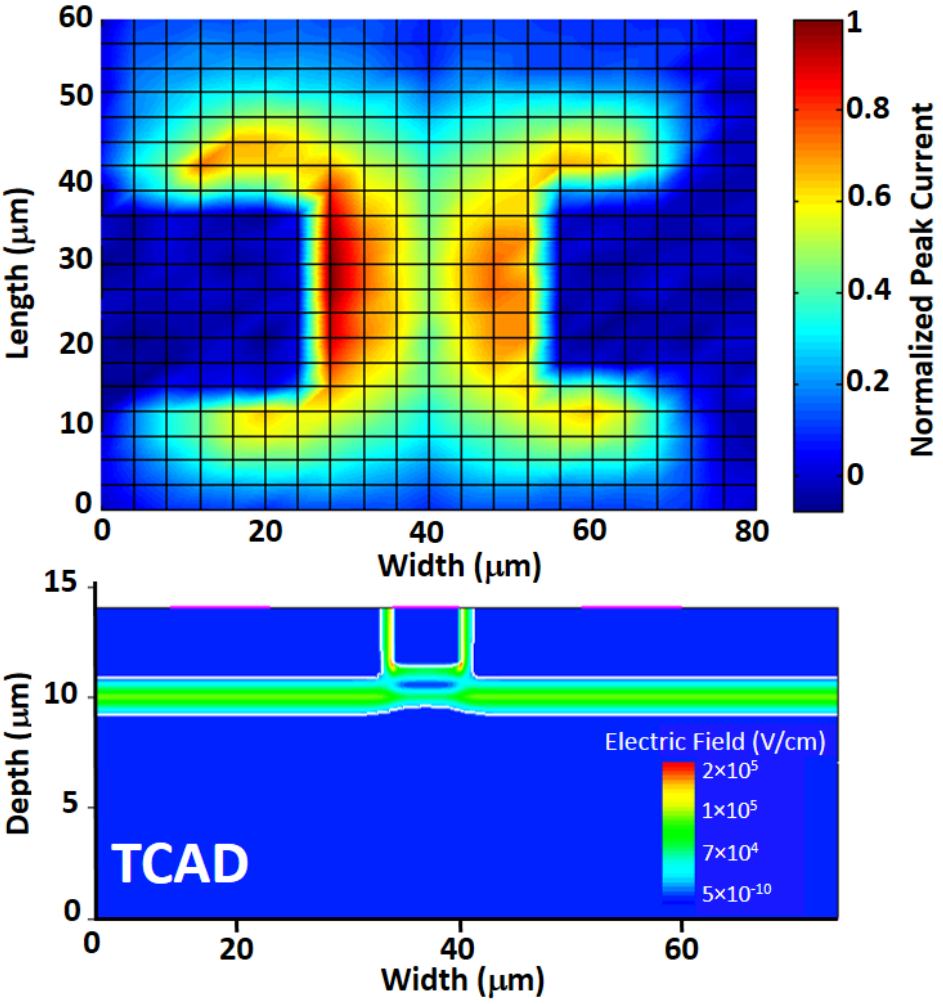

Figure IV.13: Peak current map generated with laser testing (top) and a 2-D TCAD electric field simulation (center) that indicate the geometry of depletion that are sensitive to charge generation in a reverse-biased JFET diode with drain grounded.

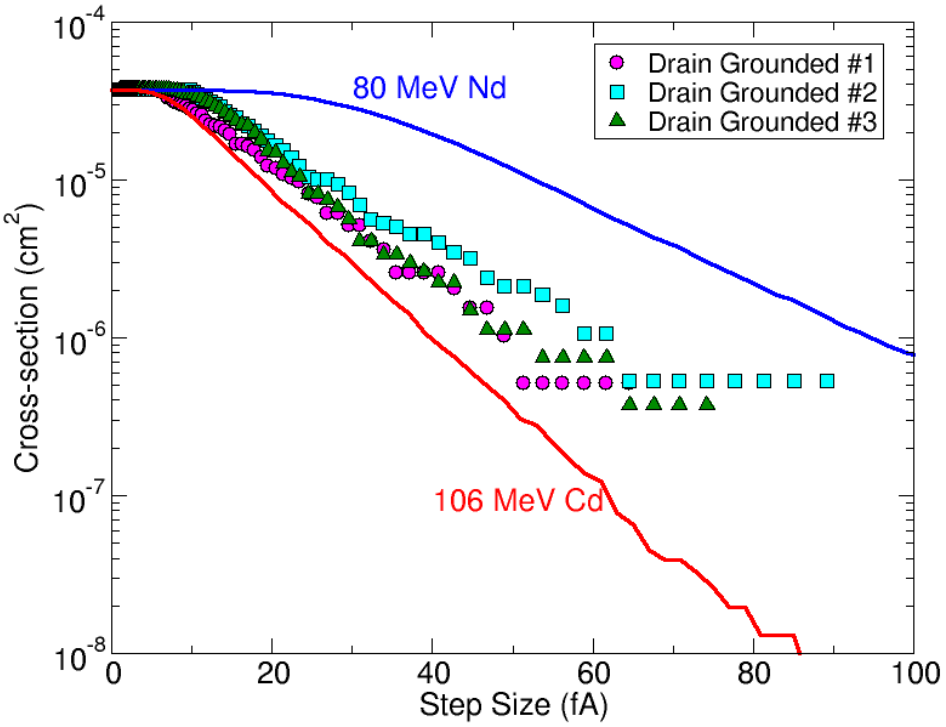

Figure IV.14: Integral cross-section of measured current step sizes for three ^{252}Cf-irradiated diodes with drain grounded and modeled current step sizes calculated from MRED simulations of 106 MeV Cd and 80 MeV Nd ions, after Auden *et al.*, 2013.

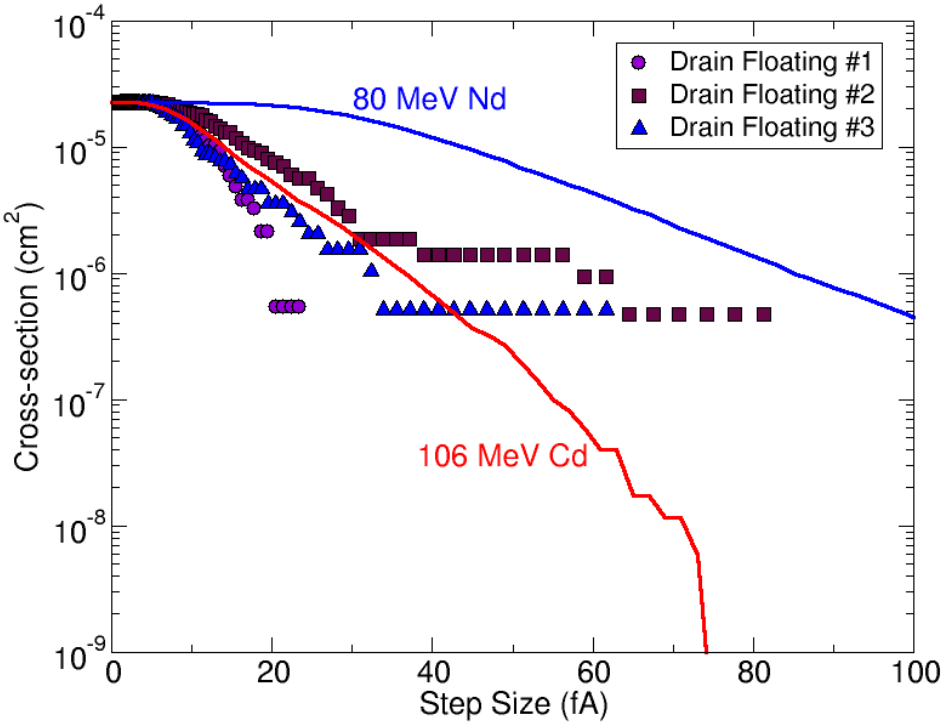

Figure IV.15: Integral cross-section of measured current step sizes for three ^{252}Cf-irradiated diodes with drain floating and modeled current step sizes calculated from MRED simulations of 106 MeV Cd and 80 MeV Nd ions.

The magnitude distribution of current steps is also calculated for the JFET diode with drain floating shown in Fig. IV.4. Fig. IV.15 shows an integral cross-section of current steps measured in three ^{252}Cf-irradiated JFET diodes reverse-biased at -12 V and current steps modeled with (II.17). The average electric field strengths shown in Fig. IV.12 for the gate / epitaxial depletion region, gate / channel depletion region, and epitaxial / substrate depletion region under the source and gate were used to calculate the Coulomb barrier reduction in the equation for generation lifetime.

Fig. IV.14 shows good agreement between measured and modeled current steps. The size distribution of current steps modeled from defects introduced by 106 MeV Cd and 80 MeV Nd provide upper and lower boundaries to the size distribution of current steps expected from ^{252}Cf fission fragments. The size distribution of measured steps appears to be more closely aligned with distribution of steps modeled from 106 MeV Cd ions than with

the steps modeled from 80 MeV Nd ions. One explanation is that the current steps modeled from both Cd and Nd ions are overestimated since the expressions for generation lifetimes $\tau_{g0}(\mathcal{E})$ and $\tau_g(\mathcal{E})$ use a reduction in thermal activation energy calculated for a 1-D Coulomb potential rather than a 3-D Coulomb potential [28]. In addition, deep level defects may be modeled more accurately with a screened Coulomb potential than a Coulomb potential [28].

Fig. IV.15 shows that MRED simulations of vacancies and interstitials, in tandem with TCAD electric field strength simulations, overestimate the size distribution of current steps observed in ^{252}Cf-irradiated diodes with the drain floating. Again, the overestimate could be attributed to the use of a 1-D Coulomb potential to model the reduced Coulomb barrier height. Since the disparity between measured and modeled steps is more pronounced in Fig. IV.15 than in Fig. IV.14, the MRED volumes representing the depletion regions in the diode with drain floating may have been too large. This would result in an overestimate of the number of damage-induced vacancies and interstitials that contribute to reverse current.

It must be stressed that the agreement between measured and modeled current steps is dependent on time and temperature. MRED simulations assume a temperature of 300 K, and all measured current steps are taken from reverse current time series of diodes irradiated at room temperature. Furthermore, MRED simulations do not take annealing or accumulated damage into account. The magnitudes of measured current steps reflect the discrete increase in reverse current that occured between 150 ms sampling periods. Relaxation of these current steps consistent with short-term annealing was observed in the 2 to 3 minute period following each current step [16], and this relaxation can be seen in Fig. III.22. Nevertheless, MRED simulations of atomic displacements provide a useful and novel method for calculating the maximum current step size observed ˜150 ms after single particle displacement damage.

CHAPTER V

Conclusions

Heavy ion-induced single particle displacement damage has been investigated in *n*-channel silicon JFET diodes. The size distribution of heavy ion-induced discrete increases in reverse current has been measured and modeled for reverse-biased ^{252}Cf-irradiated diodes.

The diodes used in this work were manufactured as *n*-channel JFETs with the gate acting as anode, the source acting as cathode, and the drain left floating. Since laser testing confirmed that only current generated in the gate / epitaxial depletion regions and in the portion of the epitaxial / substrate depletion region between the source and gate was collected at the source, ^{252}Cf irradiation was performed both on diodes with the drain floating as manufactured and with the drain grounded by bonding the drain pad to the source pad.

For ^{252}Cf-irradiated diodes biased at -12 V with the drain floating, discrete increases in reverse current were measured at 1.5 fA to 80 fA, where 1.5 fA represents the lower limit of current that can be measured with the current-to-voltage converter used in this work. For diodes biased at -12 V with the drain grounded, discrete increases in reverse current were measured at 1.5 fA to 100 fA under similar radiation conditions. All measured current steps coincided with ionization events indicative of fission fragments rather than alpha particles or secondary ionization from neutrons. Current steps exhibit a relaxation time of 3 to 5 minutes that is associated with the evolution of stable defects.

When an individual heavy ion creates displacement damage in the depletion region of a reverse-biased pn-junction, the resulting deep level vacancy and interstitial defects contribute to reverse current through Shockley-Read-Hall generation. If these defects operate inside an electric field of approximately 10^5 V/cm, less thermal energy is required for a midgap defect to emit an electron to the conduction band. The presence of the high electric field lower the defect's Coulomb barrier through the Poole Frenkel effect. At higher elec-

tric fields, the probability of multiple phonon-assisted tunneling is increased as well, but the electric fields present in the devices investigated in this work did not warrant the inclusion of multi-phonon tunneling in electric field enhancement equations. Both the Poole-Frenkel effect and multi-phonon tunneling increase the thermal emission rate of a defect. A defect operating in an electric field contributes more to reverse current than the same defect operating in electric fields less than 10^5 V/cm.

The model for the size distribution of current steps hinges upon damage-induced modification of the generation lifetime, τ_g, taking electric field enhancement of defects into account. When an incident particle creates new vacancy and interstitial defects in the depletion regions of a device, defect density N_t is increased. The pre-irradiation defect density is assumed to be the existing number of defects in a depletion region divided by the volume of the depletion region. Monte Carlo simulations of the primary knock-on atoms displaced and stopped within the device depeletion regions provide the number of new defects that can be added to the existing, pre-irradiation defects. Furthermore, both existing pre-irradiation defects and damage-induced new defects operate in electric fields inside the depletion region. The electric field enhancement for these defects can be obtained by modeling electric field strength with TCAD simulations and then calculating the reduction in a one-dimensional Coulomb barrier for that electric field. Defect energy levels are modified by the reduction in the Coulomb barrier so that the effective trap level for electrons moves closer to the conduction band while the effective trap level for holes moves closer to the valence band.

For a given incident ion, the discrete increase in Shockley-Read-Hall generation in a given depletion region is modeled as the difference in Shockley-Read-Hall generation before and after the generation lifetime is modified by the number of new defects created by the incident ion in that depletion region. The total current step associated with an incident ion is the sum over all depletion regions of the product of the electron charge, the Shockley-Read-Hall generation rate in that depletion region, and the volume of that depletion region.

Modeled current steps are calculated from Monte Carlo simulations of knock-on atoms displaced within volumes corresponding to JFET diode depletion regions. Reasonable parameters were chosen for defect capture cross-sections, defect energy levels, electric field enhancement factors, and the cutoff energy for atomic recoils. The size distributions of current steps measured in ^{252}Cf-irradiated diodes are in good agreement with the upper and lower limits of the size distribution of modeled current steps corresponding to light and heavy ^{252}Cf fission fragments (106 MeV Cd and 80 MeV Nd, respectively). Modeled current steps calculated from MRED simulations of 14.3 MeV O ions underpredict (by less than a factor of 2) the size distribution of current steps measured in Pelletron-irradiated JFET diodes.

The agreement between measured and modeled size distributions for the three combinations of bias and radiation environment suggest that current step size varies with the number of new defects created in device depletion regions by a given incident ion. In these simulations, the number of defects scales linearly with nonionizing energy deposition within device depletion regions. For both the Pelletron oxygen ions and the ^{252}Cf fission fragments, incident ions strike the diode surface at normal incidence The number of new defects created within one or more depletion regions depends on where the ion strikes the diode surface. If the incident ion traverses both the gate / epitaxial depletion region and the epitaxial / substrate depletion region, the number of defects created *that contribute to reverse current* will be much higher than the number of electrically active defects created if an ion traverses the epitaxial / substrate depletion region only.

The maximum size of current steps caused by single particle displacement damage is explained using Monte Carlo simulations of atomic displacements when electric field enhancement of defect emission is taken into account. Increases in reverse current caused by single particle displacement damage have been measured in ^{252}Cf-irradiated JFET diodes and modeled using Monte Carlo simulations of new vacancy and interstitial defects that operate in electric fields of ~10^5 V/cm. Electric field emission enhancement is calculated

by modeling midgap defects as 1-D Coulomb potentials and finding the reduction in thermal activation energy required to emit electrons and holes from the defect energy level. Electric field strength is calculated with TCAD simulations. Increased density of vacancy and interstitial defects is calculated from Monte Carlo simulations of atomic displacements using MRED simulations of 106 MeV Cd and 80 MeV Nd, typical light and heavy ^{252}Cf fission fragments.

When the expression for generation lifetime is modified to incorporate radiation-induced defect density and electric field enhancement of defect emission rates, the distribution of modeled current steps shows good agreement with current steps that are measured 150 ms after displacement damage occurred. This work extends the understanding of single particle displacement damage beyond the average damage event size calculated with NIEL. The distribution of radiation-induced discrete increases in reverse current is related to the distribution of energy-deposition events, once the effects of high electric fields are taken into account.

Appendices

Appendix A: Table of Symbols

Symbol	Units	Explanation
k	J K^{-1} or eV K^{-1}	Boltzmann's constant
n_i	carriers cm^{-3}	intrinsic carrier concentration
q	C	charge of an electron
r	cm	distance between an electron and a localized energy state
v_{th}	cm s^{-1}	thermal velocity of electrons
x_d	cm	depletion region width
x_i	cm	generation region width
A	cm^2	depletion region area
$D_{n,p}$	cm^2 s^{-1}	diffusion coefficients of electrons and holes
$\mathcal{E}$	V cm^{-1}	electric field strength
E_c	eV	conduction band energy level
E_{eh}	eV	energy required to create an electron-hole pair
E_i	eV	intrinsic Fermi level
E_t	eV	defect energy level
E_v	eV	valence band energy level
$E^0{}_{act,n}$	eV	zero-field activation energy for emission of electron from defect to conduction band
$E^0{}_{act,p}$	eV	zero-field activation energy for emission of electron from defect to valence band
$E_{act,n}$	eV	activation energy for emission of electron from defect to conduction band
$E_{act,p}$	eV	activation energy for emission of electron from defect to valence band
$\delta E_{actn,p}$	eV	electric field-induced change in defect activation energy for electron and hole emission
I	A	ideal diode current
I_R	A	reverse current across a diode
ΔI_R	A	discrete change in reverse current
I_{R0}	A	pre-irradiation reverse current
N	defects	number of defects in a depletion region
$N_{int,vac}$	defects	number of existing interstitial or vacancy defects in a depletion region
$N'_{int,vac}$	defects	number of new radiation-induced interstitial or vacancy defects in a depletion region
N_t	defects cm^{-3}	defect density
N'_t	defects cm^{-3}	post-irradiation defect density
$N_{A,D}$	atoms cm^{-3}	acceptor or donor doping level
$NIEL$	MeV cm^2 g^{-1}	nonionizing energy loss
T	K	temperature
U	carriers s^{-1} cm^{-3}	Shockley-Read-Hall recombination-generation rate
V_a	V	Voltage applied across diode
ε_{Si}	F cm^{-1}	permittivity of silicon
ϕ_i	V	built-in voltage of *pn*-junction
$\phi_{n,p}$	V	quasi-Fermi level for electrons or holes
σ	fA	standard deviation of reverse current
$\sigma_{n,p}$	cm^2	capture cross-section for electrons and holes
τ_g	s	generation lifetime
τ_{g0}	s	pre-irradiation generation lifetime
$\tau_{n0,p0}$	s	minority carrier lifetime of electrons, holes
$\tau'_{n0,p0}$	s	post-irradiation minority carrier lifetime of electrons, holes
θ	°	angle between r and the direction of the electric field
Ψ	V	electric potential inside junction

Table V.2: Symbols Used in this Work.

Appendix B: Design and Etching of a Printed Circuit Board

The reverse current measurement circuit described in III.2 was designed and etched by hand onto a printed circuit board (PCB) using the following process.

Materials:

- Copper clad board
- Small plastic container (area slightly larger than dimensions of copper clad board)
- Laser printer
- Sharpie marker
- Glossy magazine paper
- 200 ml muriatic acid
- 100 ml hydrogen peroxide
- Water wash bottle
- Acetone wash bottle
- Scouring pad
- Windex
- Paper towels
- Tweezers
- Safety gloves, goggles, apron
- Large glass bottle with screw cap (waste container)
- VEHS hazardous waste labels (call 615-322-2057)

First, the circuit's copper layout was designed using the FreePCB software, an open-source PCB layout editor. This simple current-to-voltage converter used an LMC6001 op amp, two 100 GΩ resistors, and a 4.7 pF capacitor. Fig. V.1 shows the circuit's copper layout. To reduce noise from circuit leakage, each of the op amp's pins, the resistor connecting the negative input terminal to ground, and the positive and negative power supply wires are inserted into gold discrete component jacks. The copper layout shows the solder pads for these component jacks, and all other components were soldered in air to further reduce circuit leakage. The circles in each of the design's four corners are for screw holes so that metal screws will connect the circuit's ground lines to the diecast aluminum box enclosing the circuit.

Next, the copper layout image was then transferred to a piece of copper clad board. The copper clad board was prepared by scrubbing the shiny side with a scouring pad and then cleaning the surface with acetone. The combiontoner from the laser printer The copper layout was horizontally flipped so that its mirror image could be printed with a laser printer onto glossy paper (a leaf of the Nuclear Science and Plasma newsletter). The printed mirror image of the copper layout was placed facedown on the prepared copper clad board, and a hot iron was applied for twenty minutes. The heat transferred the ink and laser toner from the paper's glossy surface to the copper clad board. The copper clad board was rinsed with water to remove the remaining glossy paper, resulting in a printed image of the circuit's copper layout on the copper clad board. The final circuit design was touched up with a Sharpie marker.

Finally, the printed copper clad board was submerged in a plastic container containing a solution of two parts muriatic acid to one part hydrogen peroxide. The container was gently agitated for five minutes as the exposed copper dissolved. The copper protected by the laser toner and Sharpie ink was not exposed to the etching solution. The printed circuit board was removed from the solution and rinsed with water. The laser toner and Sharpie ink were removed with acetone to expose the copper layout. Etching solution and rinse

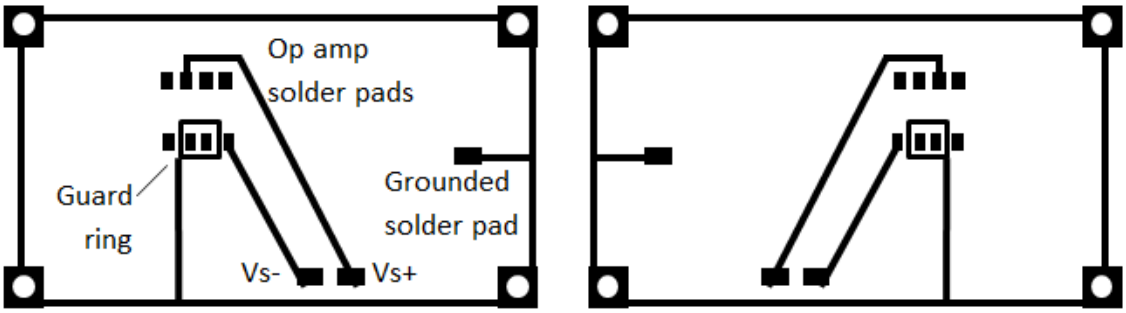

Figure V.1: Copper layout for reverse current measurement circuit. The layout on the left shows the circuit's labeled solder pads. The layout on the left is the mirror image ironed on to the copper clad board.

water should be decanted into a glass bottle with a screw top lid, labeled with a VEHS waste label, and removed by VEHS personnel for disposal.

The result of this design and etching process was a printed circuit board ready for screw holes to be drilled and discrete component jacks to be soldered to the copper solder pads.

Reference: "Toner Transfer and Muriatic Acid Etchant: Making PCBs at LVL1",

http://www.meatandnetworking.com/projects/toner-transfer-and-muriatic-acid-etchant-making-pcbs-at-lvl1/, accessed 14 December 2012

Appendix C: Chemical and Mechanical Package Decapsulation

This appendix outlines the chemical and mechanical decapsulation of packaged semiconductor devices. This procedure is intended to provide a cheap, fast, in-house procedure for reliable decapsulation that results in electrically functional devices ready for radiation testing.

Chemical Package Decapsulation

Chemical decapsulation is suitable for devices packaged in epoxy. The following technique will remove the epoxy directly over a chip while leaving the epoxy holding the package and pins in place. The result is an exposed chip in a functional package.

- Red fuming nitric acid (90% HNO_3) (Location: Stevenson 5637 hood)
- Glass dish
- VEHS or plastic tray (secondary container)
- Large glass bottle with screw cap (waste container)
- VEHS hazardous waste labels (call 615-322-2057)
- 2 plastic pipettes
- Tweezers
- Exacto-knife
- Acetone wash bottle
- Water wash bottle
- Long neoprene gloves worn over nitrile gloves
- Safety goggles

- Long-sleeved lab coat
- Plastic apron
- Street clothing: long-sleeved shirt, long pants, shoes of solid leather or rubber

Perform the chemical decapsulation procedure under a fume hood. Place a VEHS hazardous waste label on the waste container. Labels should be filled out with users name, contact information, and waste materials (Red fuming nitric acid, plastic / epoxy, water). The fume hoods glass shield is pulled down as far as possible without restricting movement.

Use the exacto-knife to etch a shallow trough into the devices surface epoxy. The trough should be the approximate shape and location of the silicon die. Use the tip of an emery board to sand down the trough. See Fig. V.2. Take time to make the trough as deep as possible; this will reduce the amount of HNO_3 needed to expose the silicon chip, better protecting the device and its pins.

Next, place device into glass dish. Use a pipette to place a small drop of HNO_3 (0.1 mL) into the etched trough. Allow the HNO_3 to dissolve epoxy for a few minutes. Gently agitate the dish with a gloved hand or chemical shaker to speed reaction time. Sluice the device with water and use a second pipette to transfer waste solution to waste container. Inspect troughs surface under a magnifying glass or microscope. Repeat the application of HNO_3, water sluice, and visual inspection until the shiny die surface is fully exposed. Rinse with acetone. View the chip surface under a microscope to see whether any small pieces of epoxy remain on the die surface, as in the device on the right of Fig. V.2. Repeat the application of HNO_3 and water sluice as needed until die surface is clean. If at any time the acid begins to bubble with a turquoise green color near the packages pins at any time, sluice with water immediately.

Rinse device with acetone once die is fully exposed. Use tweezers to remove device. Use second pipette to transport waste water to waster container. Use tweezers to transport any large chunks of epoxy to waste container. Use H_20 wash bottle to sluice device

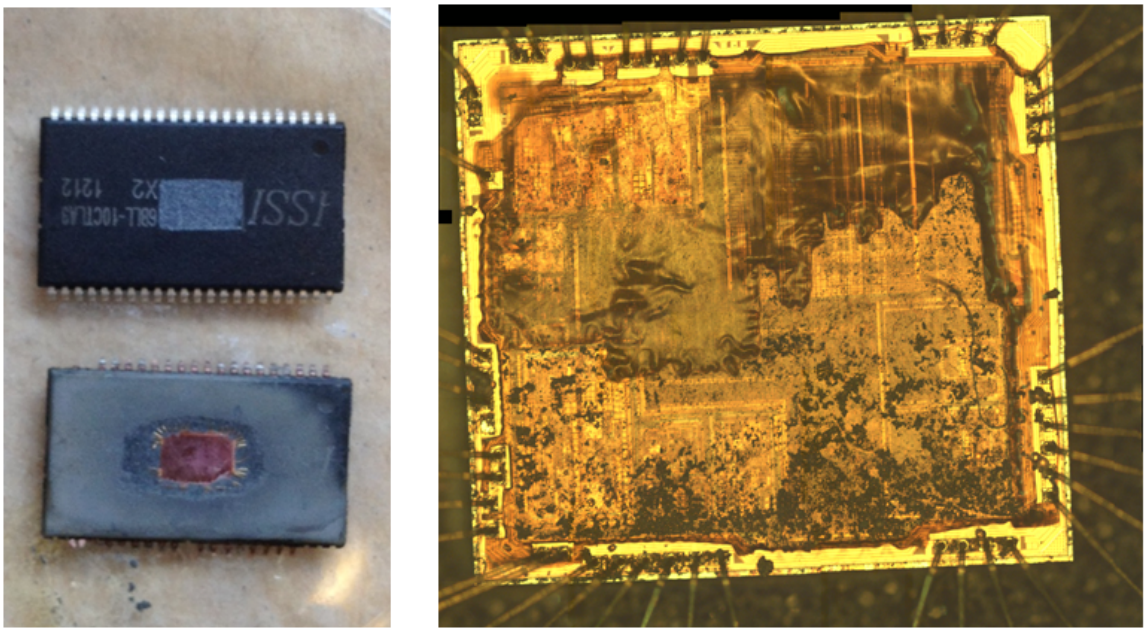

Figure V.2: Decapsulated chips. The image on the left shows two identical devices. The top device has had a trough etched in the epoxy with an Exacto-knife, and the bottom device shows a fully exposed chip. The image on the right shows a microscope view of a chemically decapsulated microcontroller with epoxy residue visible on the chip surface.

and inside of glass dish with water. Rinse both pipettes by transporting waste water to waste container. Tighten screw cap on waste container. When waste container is full or all decapsulations are finished, call VEHS at 615-322-2057 to remove waste container from hood.

Mechanical Package Decapsulation

Mechanical decapsulation is suitable for devices packaged in hermetically sealed metal cans, such as TO-3, TO-52, or TO-72 transistor outline packages. The lid of the metal can be opened and removed with a handheld can opener (such as the ThorLabs WR1 can opener shown in Fig. V.3) without damage to the device or pins.

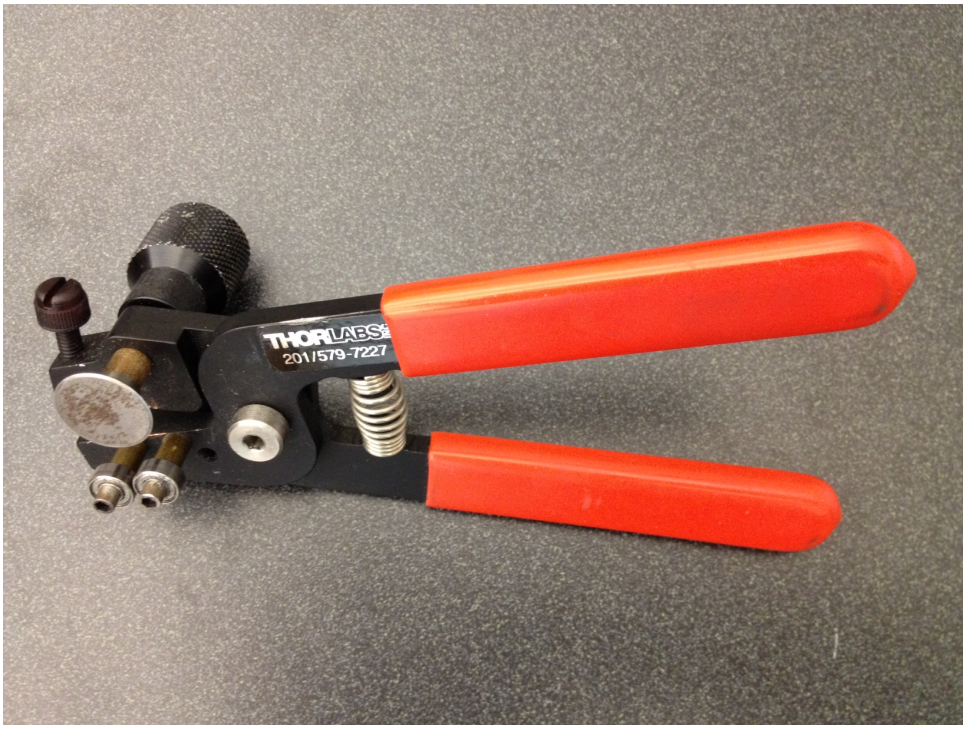

Figure V.3: A specialized tool known as a can opener used to mechanically decapsulate TO packaged devices.

Appendix D: Workflow of Experiment and Data Analysis

This appendix states the workflow of laboratory experiments and data analysis for future repeatability. The procedure described below assumes that the experiment will be performed in Featheringill 310 at Vanderbilt University.

LNA Circuit and Diode Preparation

A low noise amplification (LNA) current-to-voltage converter can be built using the circuit diagram in Fig. III.8.

1. A diecast aluminum box will serve as ground and will also provide electromagnetic shielding for the circuit. Drill 4 holes with diameter 0.512" (13.00 mm) in the side of the box. Mount one BNC connector in each hole. (Amphenol front mount bulkhead panel BNC jacks were used here.)

2. Drill 1 hole with diameter 0.512" (13.00 mm) in the lid of the box, and drill 2 smaller holes to either side. Cut out a small piece of PVC or tupperware plastic and punch a hole in it large enough to snugly fit the diode can. Screw the piece of plastic to the aluminum box lid using the 2 smaller drilled holes so that the punched hole is aligned with the bigger drilled hole. (This diode mounting strategy must be adapted if the diode is in a DIP package or D-type package rather than a can.)

3. Use the copper layout design and PCB etching technique described in Appendix B to construct a PCB with printed circuit lines.

4. Make an ultra-low noise op amp socket by a soldering gold discrete component jack upright on each of the 8 op solder pads, the V_{S+} and V_{S-} solder pads, and the grounded solder pad labelled in Fig. V.1.

5. Wire the following components in air (that is, don't let wires or components touch each other, the PCB, the side of the aluminum circuit box, or anything other than the specified connections - this reduces leakage current).

- Press the op amp into the socket. Solder op amp pins to the component jacks to ensure good connections.
- Solder one end of a 100 GΩ resistor to the negative input terminal of the op amp. Solder the other end of the resistor to the grounded solder pad.
- Solder a second 100 GΩ resistor between the positive input terminal and the output terminal of the op amp. Solder a 4.7 pF capacitor in parallel with this 100 GΩ resistor.
- Solder one end of a wire to the positive voltage supply terminal of the op amp. Solder the other end of the wire to the solder cup of the V_{S+} BNC connector.
- Solder one end of a wire to the negative voltage supply terminal of the op amp. Solder the other end of the wire to the solder cup of the V_{S-} BNC connector.
- Solder one end of a black wire to the positive input terminal of the op amp. Solder a gold discrete component jack to the other end of the wire. This component jack will hold the cathode pin of a diode.
- Solder a gold discrete component jack to one end of a white wire. This component jack will hold the anode pin of a diode. Solder the other end of the wire to the solder cup of the V_A BNC connector.
- Solder a wire to the ground terminal of each BNC jack. Solder the other end of each wire to the grounded solder pad.

6. Decapsulate the diode using the mechanical or chemical decapsulation procedure described in Appendix C.

7. Mount the decapped diode in the LNA circuit. The anode goes in the socket soldered to the white wire, and the cathode goes in the socket soldered to the black wire. Slide the diode can into the circular hole cut into the clear plastic window screwed to the lid of the LNA circuit box, and then screw the lid to the box.

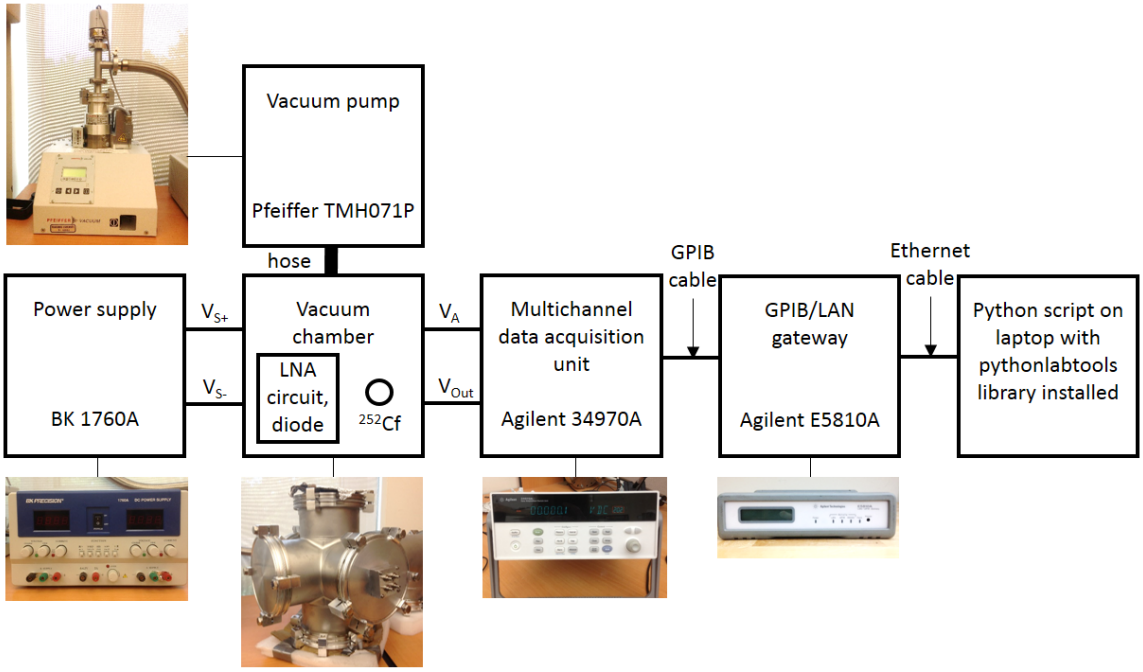

Figure V.4: Diagram of experimental setup showing equipment and connections.

Experiment Set-up and Irradiation

Fig. V.4 shows a diagram of the equipment used for *in situ* reverse current measurements of ^{252}Cf-irradiated diodes along with the connections between pieces of equipment.

1. Remove the electrical feedthrough flange from the vacuum chamber. The feedthrough has four male SMA connectors mounted on each side. Connect four cables between the male BNC connectors on the LNA circuit box to the four SMA adapers on the inside of the electrical feedthrough:

    - V_{S+}: positive voltage supply for op amp
    - V_{S-}: negative voltage supply for op amp
    - V_A: applied voltage for diode
    - V_{Out}: output voltage from LNA current-to-voltage converter circuit

2. Connect four cables between the male SMA connectors on the outside of the electrical feedthrough to the power supply and multichannel data acquisition unit:

- V_{S+}: BK 1760A power supply positive voltage on channel A (+6 V used here)
- V_{S-}: BK 1760A power supply negative voltage on channel B (-6 V used here)
- V_A: Analog output channel 104 on Agilent 34970A multichannel data acquisition unit. Set this channel to the desired reverse bias. (-12 V used here.)
- V_{Out}: Digital input channel 201 on Agilent 34970A multichannel data acquisition unit. Set this channel to measure DC volts in the desired range.

3. Connect the Agilent 34970A multichannel data acquisition unit to the Agilent E5810A GPIB / LAN gateway using a GPIB cable.

4. Connect the gateway to the laptop using an ethernet cable. Open a browser on the laptop. Type the IP address displayed on the gateway into the browser's address field. If a login window pops up, keep the default password and press Submit. On the equipment page, press "Find instruments" and select "gpib 0,9." Test the connection by pressing "IDN" - the Agilent 34970A should identify itself by printing its name and some connection details in the text area on the equipment page. Troubleshooting - check the IP address, the ethernet cable and connections, the GPIB cable, and that "gpib 0,9" is the instrument selected.

5. Connect the vacuum chamber to the Pfeiffer TMH 071 P turbomolecular vacuum pump with hose and clamps. Hose is rubber or PVC with steel casing. Turn the pump power on at the switch, and then start the pump by pressing the soft button once. The roughing pump will start first, and the turbo pump will start after a few minutes (it sounds like an airplane taking off). Monitor the vacuum level on channel . Trouble-shooting: if the vacuum level plateaus before reaching 10^{-5} mbar, check the system for leaks. Squirt isopropyl alcohol around the joins between feedthroughs or hose clamps and vacuum chamber while checking for spikes or dips in vacuum level. Do not overtighten nuts holding feedthroughs to chamber. If necessary, remove feedthroughs or hose and clean the gaskets. Check gaskets for rips or tears.

6. Place the LNA circuit box inside the vacuum chamber. Mount the ^{252}Cf source the desired distance from the diode's surface. (NOTE: ^{252}Cf emission products will begin striking the device surface now.) Do not use tape or adhesives to secure ^{252}Cf source, and do not pierce the source. Instead, construct a holder or box for the source with a window cut out for the source's active area, and secure the holder with screws or cable ties. Avoid using wood and cardboard inside the vacuum chamber since the moisture content of these materials will greatly increase the amount of time needed to pump down the vacuum chamber. Re-attach the electrical feedthrough to the vacuum chamber and tighten nuts.

7. Start the python script that reads time and output voltage. Data is written continuously to a file on the laptop. Command:

```
python ScriptName filename &
```

Finish Experiment and Analyze Data

1. Keep taking data until 1) the output voltage corresponds to the desired maximum leakage current (1 V = 10 pA), 2) the output voltage reaches 6 V (maximum range of LNA circuit), or 3) the desired amount of time has elapsed.

2. End the experiment with this procedure:

   - Stop data acquisition by pressing any key or, if the process run by the script was placed in the background with "&", kill the process. Open a terminal and type "ps aux" to list job ID's, find the python script's ID, and kill the process with "kill jobID".
   - Turn off the vacuum pump by pressing the soft button once. Vent the chamber by turning the wingnut located on the back of the pump.
   - Remove one of the feedthroughs or plain flanges on the vacuum chamber and remove the ^{252}Cf source. Replace the source in its packaging and return it to

the radiation source safe.

- Power down all equipment.

3. Convert the data read from the Agilent 34070A multichannel data acquisition unit to other data products for further analysis:

    - Reverse current time series:
    - Identification of current steps and pulses:

Links to Equipment Manuals

1. BK 1760A power supply: https:www.bkprecision.comdownloadsmanualsen1760A_manual.pdf
2. Agilent 34970A multichannel data acquisition unit: http:cp.literature.agilent.comlitwebpdf34972-90010.pdf
3. Pfeiffer TMH 071 P vacuum pump: http:/ /mmrc.caltech.eduVacuumPfeiffer%20TurboTMHTMU_071P.pdf
4. Agilent E5810A GPIB / LAN gateway: http:cp.literature.agilent.comlitwebpdfE5810-90001.pdf

Appendix E: Identification of Current Pulses and Steps

This appendix presents python code written by Elizabeth Auden that identifies current pulses and steps in reverse current time series of irradiated JFET diodes.

```
#FindSteps_CrossSection_PAD1.py
#Author: Elizabeth Auden (elizabeth.c.auden@vanderbilt.edu)
# 3 December 2012

############################################################
# NOTE: turned off multi-peak finder 11:24 06/07/12 ECA
#       to allow better detection of 10 fA first peaks
############################################################

import sys
sys.path.append('/usr/local/radeffects/libpython/mred-9xx')
sys.path.append('/usr/local/radeffects/old/packages/graceplot')
import math
import vumps
import os
import medfilt
import GracePlot

class myGrace(GracePlot.GracePlot):
    grace_command='gracebat'

def ReadDataFile(filename, delay):
   times = []
   voltages = []
   first_data_line = True
   initial_time = 0.
   for line in file(filename):
      line = line.split()
      if len(line) > 5:
         time = line[5]
         reading = line[6]
         if first_data_line == True:
            initial_time = float(time)
         if (float(time) - initial_time >= 0.0 + delay):
            times.append((float(time) - float(initial_time))/3600.)
            voltages.append(float(reading))
         first_data_line = False
   return voltages, times

# Median filter data
def MedianFilterVoltages(voltages, L):
   mf_voltages = medfilt.medfilt1(voltages,int(L))
   return mf_voltages

# Peak detection
# Algorithm:
#   1. threshold = 2*std dev
#   2. find discrete change in voltage amplitude > threshold
#   3. see if voltage change at t0+3*dt = initial change * ((e\^(-3dt/RC))\^-1) +/- std dev
#   4a. if yes, record discrete voltage change and time as detected impulse
#   4b. if yes, record discrete voltage change and time as false impulse

def GetNIons(voltages, times, stddev, peakThreshold):

   resistor = 1.e11
   capacitor = 4.7e-12
   rc = resistor * capacitor
   alpha_threshold = 4. * stddev
   threshold = peakThreshold
   logflag=False
```

```
nIons = 0
nPulses = 0

length_voltages=len(voltages)
i=1
while i < length_voltages-2:
  h = voltages[i] - voltages[i-1]
  if (h > threshold) and (voltages[i] >= 0.):
    # Find difference in time (in s) between current
    # reading's time and time 1 reading later
    t = (float(times[i+1]) - float(times[i]))*3600.
    expected_vout_decay = h*(math.e**(-t/rc))
    actual_decay = voltages[i+1]-voltages[i-1]
    upper_limit = max(1.25*expected_vout_decay, expected_vout_decay + stddev)
    lower_limit = min(0.75*expected_vout_decay, expected_vout_decay - stddev)
    anomaly = False
    if (actual_decay >= lower_limit) and (actual_decay <= upper_limit):
      nIons += 1
      nPulses += 1
    elif actual_decay < lower_limit:
      anomaly = True
    elif actual_decay > upper_limit:
      risingedge_h = voltages[i+1]-voltages[i-1]
      risingedge_t = (float(times[i+2]) - float(times[i+1]))*3600.
      risingedge_expected_vout_decay = risingedge_h*(math.e**(-risingedge_t/rc))
      risingedge_actual_decay = voltages[i+2]-voltages[i-1]
      risingedge_upper_limit = max(1.25*risingedge_expected_vout_decay, \
        risingedge_expected_vout_decay + stddev)
      risingedge_lower_limit = min(0.75*risingedge_expected_vout_decay, \
        risingedge_expected_vout_decay - stddev)
      if (risingedge_actual_decay >= risingedge_lower_limit) and \
        (risingedge_actual_decay <= risingedge_upper_limit):
        nIons += 1
        nPulses += 1
        # now treat h and i as if first point didn't exist
        h=risingedge_h
        i=i+1
    else:
      anomaly = True

  elif (h < threshold) and (voltages[i] >= 0.) and (h > alpha_threshold):
    # Find difference in time (in s) between current
    # reading's time and time 1 reading later
    t = (float(times[i+1]) - float(times[i]))*3600.
    expected_vout_decay = h*(math.e**(-t/rc))
    actual_decay = voltages[i+1]-voltages[i-1]
    upper_limit = max(1.25*expected_vout_decay, expected_vout_decay + stddev)
    lower_limit = min(0.75*expected_vout_decay, expected_vout_decay - stddev)
    anomaly = False
    if (actual_decay >= lower_limit) and (actual_decay <= upper_limit):
      nPulses += 1
    elif actual_decay < lower_limit:
      anomaly = True
    elif actual_decay > upper_limit:
      risingedge_h = voltages[i+1]-voltages[i-1]
      risingedge_t = (float(times[i+2]) - float(times[i+1]))*3600.
      risingedge_expected_vout_decay = risingedge_h*(math.e**(-risingedge_t/rc))
      risingedge_actual_decay = voltages[i+2]-voltages[i-1]
      risingedge_upper_limit = max(1.25*risingedge_expected_vout_decay, \
        risingedge_expected_vout_decay + stddev)
      risingedge_lower_limit = min(0.75*risingedge_expected_vout_decay, \
        risingedge_expected_vout_decay - stddev)
      if (risingedge_actual_decay >= risingedge_lower_limit) and \
        (risingedge_actual_decay <= risingedge_upper_limit):
        nPulses += 1
        # now treat h and i as if first point didn't exist
        h=risingedge_h
        i=i+1
```

```
        else:
          anomaly = True
      i=i+1
    #return peaks, peak_heights, peak_times, peak_hist, peak_indices
    return nIons, nPulses


# Step Detection
def FindSteps(voltages, mf_voltages, times, mf_stddev, L):
    stepInPrev500Pts = False
    stepInPrev500PtsCounter = 1
    points_to_average=500
    threshold=mf_stddev
    length_mfvoltages=len(mf_voltages)
    lowlimit=0.0001
    highlimit=0.01
    nbins=100
    logflag=True
    numSteps = 0
    step_times=[]
    steps=[]
    step_heights=[]
    step_hist = mred.getNewHistogram(hMin=lowlimit, hMax=highlimit, nBins=nbins, \
      logSpacing=logflag)
    annealed_step_times=[]
    annealed_steps=[]
    annealed_step_heights=[]
    annealed_step_hist = mred.getNewHistogram(hMin=lowlimit, hMax=highlimit, \
      nBins=nbins, logSpacing=logflag)
    stop_point = length_mfvoltages-points_to_average

    for i in range(points_to_average, stop_point):
      if stepInPrev500Pts == False:
        edge = mf_voltages[i] - mf_voltages[i-1]
        if edge > threshold:
          prev_avg=(sum(mf_voltages[i-points_to_average-1:i-1]))/float(points_to_average)
          next_avg=(sum(mf_voltages[i+1:i+points_to_average+1]))/float(points_to_average)
          step=next_avg-prev_avg

          if step > (threshold):
            step_times.append(times[i-1])
            step_hist.add(step)
            steps.append(step+prev_avg)
            step_heights.append(step)
            stepInPrev500Pts = True

            # Find average of next 500 points after 3 minutes, or 1200 points
            three_minutes_later_next_avg = \
              (sum(mf_voltages[i+1201:i+points_to_average+1201]))/float(points_to_average)
            annealed_step=three_minutes_later_next_avg-prev_avg
            annealed_step_times.append(times[i+1199])
            annealed_step_hist.add(annealed_step)
            annealed_steps.append(annealed_step+prev_avg)
            annealed_step_heights.append(annealed_step)
            numSteps += 1
      else:
        if stepInPrev500PtsCounter < 500:
          stepInPrev500PtsCounter += 1
          stepInPrev500Pts = True
        else:
          stepInPrev500PtsCounter = 1
          stepInPrev500Pts = False

    return numSteps, steps, step_heights, step_times, step_hist, annealed_steps, \
      annealed_step_heights, annealed_step_times annealed_step_hist

###################################
```

```
def MakeGracePlot(x_datasets,y_datasets,histogram=False,legends=None,
    xax_min=None, xax_max=None, xlog=True, xscaler=1, xlabel='',
    yax_min=None, yax_max=None, ylog=True, yscaler=1, ylabel='Weight', nbins=1024,
    lowlimit=0., highlimit=1., title='',grace_format_file=None, reverse_sum=False,
    width_normalize=False, outfile_stem='plot', jobid=None, jobname=None,
    logflag=False):

  try:

    datasets=[]
    ymin=1e308; ymax=0; xmin=1e308; xmax=0

    hnum=0
    dnum=0
    for y_dataset in y_datasets:
      if histogram==True:
         #reverse_sum = True
         h = y_dataset
         if reverse_sum:
             h=h.sumArrayReverse()
         elif width_normalize:
             h=h.scaleByBinWidth()

         xvals=[x*xscaler for x in h.x]
         yvals=[y*yscaler for y in h.y]
         yvals_plain=[y*1.0 for y in h.y]
         dyvals=[math.sqrt(y2)*yscaler for y2 in h.y2 ] #fixed from sqrt(y) 20080115 MHM
         xlog=True
         ylog=True

      else:
         xvals=[x for x in x_datasets[dnum]]
         yvals=[y for y in y_dataset]
         dyvals=[y+stddev for y in yvals ] #fixed from sqrt(y) 20080115 MHM
         xlog=False
         ylog=False

      if ylog:
         ymin=min(ymin, min([y for y in yvals if y!=0]))
      else:
         ymin=min(ymin, min(yvals))
      ymax=max(ymax, max(yvals))
      if (ymax == ymin) and (ymin == 1.0):
         ymin = 0.1
         ymax = 10.
      if xlog:
         xmin=min(xmin, min([x for x in xvals if x!=0]))
      else:
         xmin=min(xmin, min(xvals))
      xmax=max(xmax, max(xvals))

      # Do style info: filled circles, no lines, size=25, black, red, green, blue
      if dnum==0:
         mysymbol=1
         mysymbolsize=0.5
         myfillcolor=1
         mysymbollinewidth=0.5
         myfillpattern=1
         mysymbolcolor=1
         mylinetype=0
         mylinewidth=1
         mylinecolor=1
         mylegend=legends[0]
      elif dnum==1:
         mysymbol=1
         mysymbolsize=0.5
         mysymbolcolor=2
         mysymbollinewidth=0.5
```

```
      myfillpattern=1
      myfillcolor=2
      mylinetype=0
      mylinewidth=1
      mylinecolor=15
      mylegend=legends[1]
   elif dnum==2:
      mysymbol=1
      mysymbolsize=0.5
      mysymbolcolor=3
      mysymbollinewidth=0.5
      myfillpattern=1
      myfillcolor=3
      mylinetype=0
      mylinewidth=1
      mylinecolor=3
      mylegend=legends[1]
   elif dnum==2:
      mysymbol=1
      mysymbolsize=1.0
      mysymbollinewidth=2
      myfillpattern=0
      myfillcolor=1
      mysymbolcolor=15
      mylinetype=0
      mylinewidth=0
      mylinecolor=0
      mylegend=legends[2]
   elif dnum==3:
      mysymbol=1
      mysymbolsize=1.0
      myfillpattern=0
      mysymbolcolor=4
      mysymbollinewidth=2
      myfillcolor=1
      mylinetype=0
      mylinewidth=0
      mylinecolor=0
      mylegend=legends[3]


   l1=GracePlot.Line(type=mylinetype,linewidth=mylinewidth,color=mylinecolor)
   e1=GracePlot.Errorbar(onoff='off',riserclip='on', risercliplength=0.1)
   s1=GracePlot.Symbol(errorbar=e1,skip=0,symbol=mysymbol,color=mysymbolcolor,\
     fillcolor=myfillcolor,size=mysymbolsize, fillpattern=myfillpattern, \
     linewidth=mysymbollinewidth)
   d1=GracePlot.Data(x=xvals, y=yvals, dy=dyvals, type='xydy', symbol=s1, line=l1, \
     legend=mylegend)
   datasets.append(d1)
   dnum=dnum+1

graceSession=myGrace(width=5.5, height=3.75)
g=graceSession[0]
g.plot(datasets)
for axname, ax_min, ax_max, val_min, val_max, logaxis, axfunc, axlabel in (
    ('y', yax_min, yax_max, ymin, ymax, ylog, g.yaxis, ylabel),
    ('x', xax_min, xax_max, xmin, xmax, xlog, g.xaxis, xlabel)):
    if logaxis:
        if ax_max is None:
            #make ymax rounded to nearest decade up
            ax_max=math.pow(10, math.ceil(math.log10(val_max*.999999)))
        if ax_min is None:
            if val_min==0.0:
                ax_min=1e-8*ax_max
            else:
                #make ymax rounded to nearest decade down
                ax_min=math.pow(10, math.floor(math.log10(val_min*1.00001)))
        scale='logarithmic'
```

```
            ticks=GracePlot.Tick(major=10, minorticks=9)
        else:
            if ax_max is None or ax_min is None:
                #ax_min=0.0
                ax_min=lowlimit
                ax_max=val_max
            scale='normal'
            ticks=GracePlot.Tick()
        #grace requires keywords xmin, xmax or ymin, ymax
        axlimits={axname+'min': ax_min, axname+'max': ax_max}
        axfunc(label=GracePlot.Label(axlabel, font=4, charsize=1.48), tick=ticks, \
          scale=scale, **axlimits)
    g.legend(font=4,charsize=1.3)
    g.title(title)
    graceSession.send_commands('saveall "%s.agr"' % outfile_stem,'exit')
    return ""

  except:
    #meltdown, return the traceback to the caller
    import cStringIO
    stdout=sys.stdout
    out=cStringIO.StringIO()
    sys.stdout=out
    import traceback
    traceback.print_exc()
    sys.stdout=stdout

    return out.getvalue()


###################################

def usage():
    return

if __name__ == "__main__":

   filename=''
   stddev=0
   L=0

   # Check for correct syntax
   if len(sys.argv) < 5:
     print "Syntax: FindSteps_CrossSection.py datfile stddev L peakThreshold"
     sys.exit()
   else:
     filename=sys.argv[2]
     stddev=float(sys.argv[3])
     L=float(sys.argv[4])
     peakThreshold=float(sys.argv[5])

   basename, extension = os.path.splitext(filename)
   print "Data file: ", filename, ", stddev: ", stddev, ", L: ", L

   # Read data file
   print "In ReadDataFile"
   # Add delay in case first n seconds of dataset should be ignored (for instance,
   # ion gauge still on or ion rate not properly adjusted). Uncomment one option.
   #delay=600.0 # Delay of 10 minutes
   delay=0.0 # Delay of 0 minutes
   voltages, times = ReadDataFile(filename, delay)

   # Median filter data
   print "In MedianFilterVoltages"
   mf_voltages = MedianFilterVoltages(voltages, L)
   lengthMFV = len(mf_voltages)

   mf_stddev=0.00015
```

```
print "MF stddev: ", mf_stddev

# Count number of ions from current pulses
print "In GetNIons"
nIons = 0
nIons, nPulses = GetNIons(voltages, times, stddev, peakThreshold)

# Step detection
print "In FindSteps"
numSteps, steps, step_heights, step_times, step_hist, annealed_steps, \
  annealed_step_heights, annealed_step_times, annealed_step_hist = \
  FindSteps(voltages, mf_voltages, times, mf_stddev, L)
# area = 2250.e-8 #area of epitaxy / substrate depl reg (cm^2) under source and gate
area = 3500.e-8 #area of epitaxy / substrate depl reg (cm^2) under source, gate, and drain
fluence = float(numSteps) / area
yscaler = 1.0/fluence
legends=[]
legends.append("Steps")

output_stem = basename + "_StepCrossSection"
xlabel="D I Reverse (fA)"
ylabel="Cross Section (cm\^-2)"
nbins=100
lowlimit=1.
highlimit=100.
logflag = True
# Convert peak size from V to fA (multiply by 10000)
fA_conversion = 10000.
current_step_hist = mred.getNewHistogram(hMin=lowlimit, hMax=highlimit, \
  nBins=nbins, logSpacing=logflag)
for x in step_hist.x:
   current_step_hist.add(x*fA_conversion)

hlist=[]
hlist.append(step_hist)
MakeGracePlot(times, hlist, histogram=True,legends=legends, xscaler=fA_conversion, \
  yscaler=yscaler, xlabel=xlabel,ylabel=ylabel,outfile_stem=output_stem, reverse_sum=True)

print "Damage factor: ", str(fA_conversion*((mf_voltages[len(mf_voltages) - 1] \
  - mf_voltages[0]))/nIons)
print "nIons: ", nIons
print "Max step size: ", max(step_heights),
print "Max annealed step size: ", max(annealed_step_heights)
print "Done with FindSteps_CrossSection.py"
```

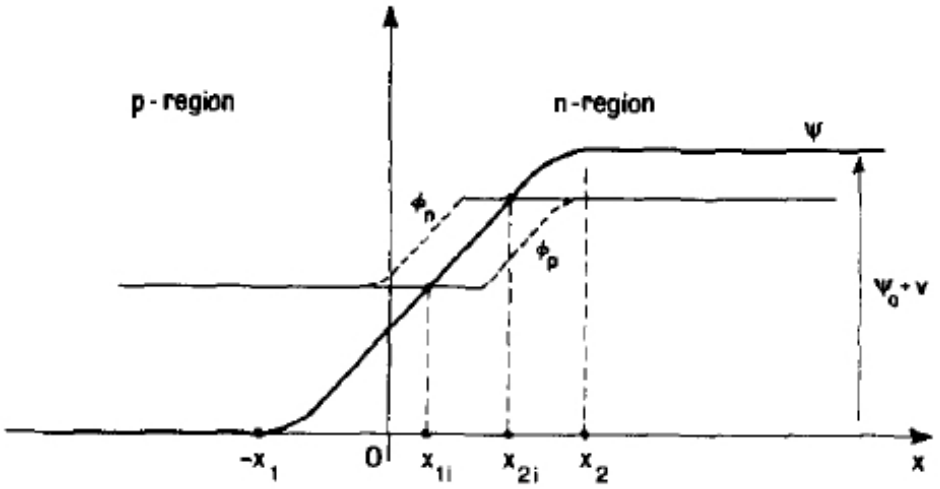

Figure V.5: The generation region width x_i and depletion region width x_d with respect to quasi-Fermi levels ϕ_n and ϕ_p and the electric potential Ψ (after Calzolari and Graffi, 1972).

Appendix F: Derivation of Generation Width Equation

In 1972, Calzolari and Graffi described the generation region as a subvolume within a *pn*-junction depletion region in which thermal carrier generation is the dominant restorative force rather than thermal recombination [35]. This condition arises when the product of electron and hole densities is less than ${n_i}^2$, so the generation region is bounded by the points at which the quasi-Fermi levels ϕ_n and ϕ_p intersect the electric potential $\Psi(x)$.

The authors note that the expression for generation width changes with doping conditions. If the *p*-type side of the metallurgical junction is heavily doped, both the electron and hole quasi-Fermi levels may intersect the electric potential on the *n*-type side of the junction, as shown in Fig. V.5 . The reverse holds true for a heavily doped *n*-type side; both quasi-Fermi levels may intersect the electric potential on the *p*-type side. If the *p* and *n* doping levels are equal (or if both sides are lightly doped), the hole quasi-Fermi level will interest the electric potential on the *p*-type side, and the electron quasi-Fermi level will interest the electric potential on the *n*-type side.

This appendix derives the generation width equation for three doping conditions in an abrupt *pn*-junction:

- $N_A >> N_D$
- $N_A << N_D$
- $N_A == N_D$.

We start by defining expressions for the electric potential, the boundaries of the depletion region, the depletion region width, the hole and electron quasi-Fermi levels, and the locations at which the quasi-Fermi levels intersect the electric potential. The metallurgical junction is assumed to be at $x = 0$. In the notation of Calzolari and Graffi, the depletion region boundary on the *p*-type side of the junction is located at $-x_1$ (or $-x_p$ in the notation

used in [34]) [35]. The n-type side depletion region boundary is located at x_2 (equivalent to x_n in [34]). The locations of these boundary points are expressed with respect to the depletion region width x_d [35]:

$$-x_1 = -\frac{N_D}{N_A + N_D} x_d \tag{V.1}$$

$$x_2 = \frac{N_A}{N_A + N_D} x_d \tag{V.2}$$

where x_d is expressed as with respect to doping levels N_A and N_D, the built-in junction voltage Ψ_0, and the applied voltage V_A [35]:

$$x_d = |-x_1| + |x_2| = \sqrt{\frac{2\varepsilon_{Si}}{q} \frac{N_A + N_D}{N_A N_D} (\Psi_0 + V_A)}. \tag{V.3}$$

Calzolari and Graffi set the electric potential Ψ equal to 0 at the edge of the depletion region on the p-type side of the junction so that electrical potential can be defined on the n-type side of the junction with respect to the built-in junction potential and the magnitude of applied reverse bias [35]:

$$\Psi(-x_1) = 0 \tag{V.4}$$

$$\Psi(x_2) = \Psi_0 + V_A \tag{V.5}$$

On the p-type side of the junction, the electric potential within the depletion region can be defined with respect to $\Psi(-x_1)$. Similarly, the electric potential within the depletion region on the n-type side of the junction can be defined with respect to $\Psi(x_2)$ [35]:

$$\Psi(x) = \frac{qN_A}{2\varepsilon_{Si}} (x + x_1)^2, -x_1 \leq x \leq 0 \tag{V.6}$$

$$\Psi(x) = \Psi_0 + V_A - \frac{qN_D}{2\varepsilon_{Si}} (x_2 - x)^2, 0 \leq x \leq x_2 \tag{V.7}$$

The hole quasi-Fermi level ϕ_p intersects the electric potential Ψ at location x_{1i}, and the electron quasi-Fermi level ϕ_n intersects the electric potential at location x_{2i} [35]. The quasi-Fermi levels (and the electric potential at the location intersected by the quasi-Fermi levels) are expressed in [35] as

$$\phi_p = \Psi(x_{1i}) = \frac{kT}{q} ln \frac{N_A}{n_i} \tag{V.8}$$

$$\phi_n = \Psi(x_{2i}) = \Psi_0 + V_A - \frac{kT}{q} ln \frac{N_D}{n_i} \tag{V.9}$$

The next three sections use the expressions for electrical potential within the depletion region to derive the generation width x_i for three doping conditions as

$$x_i = |x_{1i}| + |x_{2i}| \tag{V.10}$$

Case 1: $N_A >> N_D$

When the *p*-type doping is much higher than the *n*-type doping, both the electron and hole quasi-Fermi levels will intersect the electric potential on the lightly doped *n*-type side of the metallurgical junction. Fig. V.5 shows that under these doping conditions, x_{1i} and x_{2i} are both positive with respect to the junction. (V.9) is used to find the electric potential at x_{1i} and x_{2i}.

(a) Solve for x_{1i}: find the electrical potential $\Psi(x_{1i})$ with respect to the electric potential at x_2 as defined in (V.7), and set this equal to the hole quasi-Fermi potential defined by (V.8).

$$\Psi(x_{1i}) = \Psi_0 + V_A - \frac{qN_D}{2\varepsilon_{Si}}(x_2 - x_{1i})^2 = \frac{kT}{q} ln \frac{N_A}{n_i} \tag{V.11}$$

The built-in junction voltage Ψ_0 can be expressed in terms of doping levels [34]:

$$\Psi_0 = \frac{kT}{q} ln \frac{N_A N_D}{{n_i}^2} = \frac{kT}{q} ln \frac{N_A}{n_i} + \frac{kT}{q} ln \frac{N_D}{n_i}. \tag{V.12}$$

Using the expression for Ψ_0 given in (V.12), solve (V.11) for x_{1i} in terms of doping levels and reverse bias.

$$\left(\frac{kT}{q} ln \frac{N_D}{n_i} + \frac{kT}{q} ln \frac{N_A}{n_i} \right) + V_A - \frac{kT}{q} ln \frac{N_A}{n_i} = \frac{qN_D}{2\varepsilon_{Si}}(x_2 - x_{1i})^2 \tag{V.13}$$

$$\frac{2\varepsilon_{Si}}{qN_D} \left(\frac{kT}{q} ln \frac{N_D}{n_i} + V_A \right) = (x_2 - x_{1i})^2 \tag{V.14}$$

$$x_{1i} = x_2 - \sqrt{\frac{2\varepsilon_{Si}}{qN_D} \left(\frac{kT}{q} ln \frac{N_D}{n_i} + V_A \right)} \tag{V.15}$$

$$x_{1i} = \frac{N_A x_d}{N_A + N_D} - \sqrt{\frac{2\varepsilon_{Si}}{qN_D} \left(\frac{kT}{q} ln \frac{N_D}{n_i} + V_A \right)} \tag{V.16}$$

(b) Solve for x_{2i}: similarly, find the electrical potential $\Psi(x_{2i})$ with respect to the electric potential at x_2 as defined in (V.7), and set this equal to the electron quasi-Fermi potential defined by (V.9).

$$\Psi(x_{2i}) = \Psi_0 + V_A - \frac{qN_D}{2\varepsilon_{Si}}(x_2 - x_{2i})^2 = \Psi_0 + V_A - \frac{kT}{q} ln \frac{N_D}{n_i} \tag{V.17}$$

Solve for x_{2i} in terms of doping levels and reverse bias.

$$(x_2 - x_{2i})^2 = \frac{2\varepsilon_{Si}}{qN_D} \left(\frac{kT}{q} ln \frac{N_D}{n_i} \right) \tag{V.18}$$

$$x_{2i} = x_2 - \sqrt{\frac{2\varepsilon_{Si}}{qN_D}\left(\frac{kT}{q}ln\frac{N_D}{n_i}\right)} \tag{V.19}$$

$$x_{2i} = \frac{N_A x_d}{N_A + N_D} - \sqrt{\frac{2\varepsilon_{Si}}{qN_D}\left(\frac{kT}{q}ln\frac{N_D}{n_i}\right)} \tag{V.20}$$

(c) Solve for $x_i = |x_{1i}| + |x_{2i}|$:

$$x_i = |x_{1i}| + |x_{2i}| = \left|\frac{N_A x_d}{N_A + N_D} - \sqrt{\frac{2\varepsilon_{Si}}{qN_D}\left(\frac{kT}{q}ln\frac{N_D}{n_i} + V_A\right)}\right| + \left|\frac{N_A x_d}{N_A + N_D} - \sqrt{\frac{2\varepsilon_{Si}}{qN_D}\left(\frac{kT}{q}ln\frac{N_D}{n_i}\right)}\right| \tag{V.21}$$

$$x_i = \left|\frac{2N_A x_d}{N_A + N_D} - \sqrt{\frac{2\varepsilon_{Si}}{qN_D}}\left(\sqrt{\frac{kT}{q}ln\frac{N_D}{n_i} + V_A} + \sqrt{\frac{kT}{q}ln\frac{N_D}{n_i}}\right)\right| \tag{V.22}$$

Case 2: $N_A << N_D$

If the *n*-type doping is much higher than the *p*-type doping, both the electron and hole quasi-Fermi levels will intersect the electric potential on the lightly doped *p*-type side of the metallurgical junction. Under these conditions, x_{1i} and x_{2i} are both negative with respect to the junction. (V.8) is used to find the electric potential at x_{1i} and x_{2i}.

(a) Solve for x_{1i}: find the electrical potential $\Psi(-x_{1i})$ with respect to the electric potential at $-x_1$ as defined in (V.6), and set this equal to the hole quasi-Fermi potential defined by (V.8).

$$\Psi(x_{1i}) = \frac{qN_A}{2\varepsilon_{Si}}(x_{1i} + x_1)^2 = \frac{kT}{q}ln\frac{N_A}{n_i} \tag{V.23}$$

$$(x_{1i} + x_1)^2 = \frac{2\varepsilon_{Si}}{qN_A}\frac{kT}{q}ln\frac{N_A}{n_i} \tag{V.24}$$

$$x_{1i} = \sqrt{\frac{2\varepsilon_{Si}}{qN_A}\frac{kT}{q}ln\frac{N_A}{n_i}} - x_1 \tag{V.25}$$

$$x_{1i} = \sqrt{\frac{2\varepsilon_{Si}}{qN_A}\frac{kT}{q}ln\frac{N_A}{n_i}} - \frac{N_D x_d}{N_A + N_D} \tag{V.26}$$

(b) Solve for x_{2i}: Find the electrical potential $\Psi(x_{2i})$ with respect to the electric potential at $-x_1$ as defined in (V.6), and set this equal to the electron quasi-Fermi potential defined by (V.9).

$$\Psi(x_{2i}) = \frac{qN_A}{2\varepsilon_{Si}}(x_{2i} + x_1)^2 = \Psi_0 + V_A - \frac{kT}{q}ln\frac{N_D}{n_i} \tag{V.27}$$

As with Case 1, substitute the expression for Ψ_0 defined in terms of doping levels to solve for x_{2i}.

$$(x_{2i}+x_1)^2 = \frac{2\varepsilon_{Si}}{qN_A}\left(\left(\frac{kT}{q}ln\frac{N_D}{n_i}+\frac{kT}{q}ln\frac{N_A}{n_i}\right)+V_A-\frac{kT}{q}ln\frac{N_D}{n_i}\right) \tag{V.28}$$

$$x_{2i} = \sqrt{\frac{2\varepsilon_{Si}}{qN_A}\left(\frac{kT}{q}ln\frac{N_A}{n_i}+V_A\right)}-x_1 \tag{V.29}$$

$$x_{2i} = \sqrt{\frac{2\varepsilon_{Si}}{qN_A}\left(\frac{kT}{q}ln\frac{N_A}{n_i}+V_A\right)}-\frac{N_D x_d}{N_A+N_D} \tag{V.30}$$

(c) Solve for $x_i = |x_{1i}| + |x_{2i}|$:

$$x_i = \left|\sqrt{\frac{2\varepsilon_{Si}}{qN_A}\frac{kT}{q}ln\frac{N_A}{n_i}}-\frac{N_D x_d}{N_A+N_D}\right|+\left|\sqrt{\frac{2\varepsilon_{Si}}{qN_A}\left(\frac{kT}{q}ln\frac{N_A}{n_i}+V_A\right)}-\frac{N_D x_d}{N_A+N_D}\right| \tag{V.31}$$

$$x_i = \left|\sqrt{\frac{2\varepsilon_{Si}}{qN_A}}\left(\sqrt{\frac{kT}{q}ln\frac{N_A}{n_i}}+\sqrt{\left(\frac{kT}{q}ln\frac{N_A}{n_i}+V_A\right)}\right)-\frac{2N_D x_d}{N_A+N_D}\right| \tag{V.32}$$

Case 3: $N_A == N_D$

The final derivation of x_i can be used when the *p*-type and *n*-type doping levels are equal or if one side is doped only slightly more heavily than the other side. This derivation is used whenever the hole quasi-Fermi level intersects the electric potential on the *p*-type side of the metallurgical junction and the electron quasi-Fermi potential intersects the electric potential on the *n*-type side. Under these conditions, x_{1i} is negative and x_{2i} is positive with respect to the junction. (V.8) is used to find the electric potential at x_{1i}. (V.9) is used to find the electric potential at x_{2i}.

(a) Solve for x_{1i}: find the electrical potential $\Psi(-x_{1i})$ with respect to the electric potential at $-x_1$ as defined in (V.6), and set this equal to the hole quasi-Fermi potential defined by (V.8).

$$\Psi(x_{1i}) = \frac{qN_A}{2\varepsilon_{Si}}(x_{1i}+x_1)^2 = \frac{kT}{q}ln\frac{N_A}{n_i} \tag{V.33}$$

$$(x_{1i}+x_1)^2 = \frac{2\varepsilon_{Si}}{qN_A}\frac{kT}{q}ln\frac{N_A}{n_i} \tag{V.34}$$

$$x_{1i} = \sqrt{\frac{2\varepsilon_{Si}}{qN_A}\frac{kT}{q}ln\frac{N_A}{n_i}}-x_1 \tag{V.35}$$

$$x_{1i} = \sqrt{\frac{2\varepsilon_{Si}}{qN_A}\frac{kT}{q}ln\frac{N_A}{n_i}}-\frac{N_D x_d}{N_A+N_D} \tag{V.36}$$

(b) Solve for x_{2i}: Find the electrical potential $\Psi(x_{2i})$ with respect to the electric potential at x_2 as defined in (V.7). Set this equal to the electron quasi-Fermi potential defined by (V.9).

$$\Psi(x_{2i}) = \Psi_0 + V_A - \frac{qN_D}{2\varepsilon_{Si}}(x_2 - x_{2i})^2 = \Psi_0 + V_A - \frac{kT}{q} ln \frac{N_D}{n_i} \tag{V.37}$$

$$(x_2 - x_{2i})^2 = \frac{2\varepsilon_{Si}}{qN_D} \frac{kT}{q} ln \frac{N_D}{n_i} \tag{V.38}$$

$$x_{2i} = x_2 - \sqrt{\frac{2\varepsilon_{Si}}{qN_D} \frac{kT}{q} ln \frac{N_D}{n_i}} \tag{V.39}$$

$$x_{2i} = \frac{N_A x_d}{N_A + N_D} - \sqrt{\frac{2\varepsilon_{Si}}{qN_D} \frac{kT}{q} ln \frac{N_D}{n_i}} \tag{V.40}$$

(c) Solve for $x_i = |x_{1i}| + |x_{2i}|$:

$$x_i = \left| \sqrt{\frac{2\varepsilon_{Si}}{qN_A} \frac{kT}{q} ln \frac{N_A}{n_i}} - \frac{N_D x_d}{N_A + N_D} \right| + \left| \frac{N_A x_d}{N_A + N_D} - \sqrt{\frac{2\varepsilon_{Si}}{qN_D} \frac{kT}{q} ln \frac{N_D}{n_i}} \right| \tag{V.41}$$

$$x_i = x_d - \left[\sqrt{\frac{2\varepsilon_{Si} kT}{q^2}} \left(\sqrt{\frac{1}{N_A} ln \frac{N_A}{n_i}} + \sqrt{\frac{1}{N_D} ln \frac{N_D}{n_i}} \right) \right] \tag{V.42}$$

The generic expression for x_i given by (V.41) is applicable when the hole quasi-Fermi level intersects the electric potential on the *p*-type side of the junction and the intersection between the electron quasi-Fermi and the electric potential is on the *n*-type side. If the doping levels are equal (as is the case for the epitaxial / substrate depletion region described in Chapter III of this work), the generation width equation may be further reduced by substituting N_A for N_D.

$$x_i = \left| \sqrt{\frac{2\varepsilon_{Si}}{qN_A} \frac{kT}{q} ln \frac{N_A}{n_i}} - \frac{N_A x_d}{N_A + N_A} \right| + \left| \frac{N_A x_d}{N_A + N_A} - \sqrt{\frac{2\varepsilon_{Si}}{qN_A} \frac{kT}{q} ln \frac{N_A}{n_i}} \right| \tag{V.43}$$

$$x_i = \left| x_d - \sqrt{\frac{8\varepsilon_{Si}}{qN_A} \frac{kT}{q} ln \frac{N_A}{n_i}} \right| \tag{V.44}$$

BIBLIOGRAPHY

[1] J. L. Barth, C. S. Dyer, and G. Stassinopoulos, "Space, atmospheric, and terrestrial radiaiton environments," *IEEE Trans. Nucl. Sci.*, vol. 50, pp. 466–482, Jun 2003.

[2] J. R. Srour, C. J. Marshall, and P. W. Marshall, "Review of displacement damage effects in silicon devices," *IEEE Trans. Nucl. Sci.*, vol. 50, pp. 653–670, Dec 2003.

[3] C. J. Dale, P. W. Marshall, E. A. Burke, G. P. Summers, and G. E. Bender, "The generation lifetime damage factor and its variance in silicon," *IEEE Trans. Nucl. Sci.*, vol. 36, pp. 1872–1881, Dec 1989.

[4] J. R. Srour and D. H. Lo, "Universal damage factor for radiation-induced dark current in silicon devices," *IEEE Trans. Nucl. Sci.*, vol. 47, pp. 2451–2459, Dec 2000.

[5] E. A. Burke, "Energy dependence of proton-induced displacement damage in silicon," *IEEE Trans. Nucl. Sci.*, vol. NS-33, pp. 1276–1281, Dec 1986.

[6] G. P. Summers, E. A. Burke, P. Shapiro, S. R. Messenger, and R. J. Walters, "Damage correlations in semiconductors exposed to gamma, electron, and proton radiations," *IEEE Trans. Nucl. Sci.*, vol. 40, pp. 1372 – 1379, Dec 1993.

[7] M. J. Beck, R. Hatcher, R. D. Schrimpf, D. M. Fleetwood, and S. T. Pantelides, "Quantum mechanical description of displacement damage formation," *IEEE Trans. Nucl. Sci.*, vol. 54, pp. 1906–1912, Dec 2007.

[8] E. A. Burke and G. P. Summers, "Extreme damage events produced by single particles," *IEEE Trans. Nucl. Sci.*, vol. NS-34, pp. 1575–1579, Dec 1987.

[9] J. R. Srour and R. A. Hartmann, "Enhanced displacement damage effectiveness in irradiated silicon devices," *IEEE Trans. Nucl. Sci.*, vol. 36, pp. 1825–1830, Dec 1989.

[10] P. W. Marshall, C. J. Dale, E. A. Burke, G. P. Summers, and G. E. Bender, "Displacement damage extremes in silicon depletion regions," *IEEE Trans. Nucl. Sci.*, vol. 36, pp. 1831–1839, Dec 1989.

[11] J. R. Srour and R. A. Hartmann, "Effects of single neutron interactions in silicon integrated circuits," *IEEE Trans. Nucl. Sci.*, vol. NS-32, pp. 4195–4200, Dec 1985.

[12] J. Bogaerts, B. Dierickx, and R. Mertens, "Enhanced dark current generation in proton-irradiated CMOS active pixel sensors," *IEEE Trans. Nucl. Sci.*, vol. 49, pp. 1513–1521, Jun 2002.

[13] R. Gereth, R. H. Haitz, and F. M. Smits, "Effects of single neutron-induced displacement clusters in special silicon diodes," *J. App. Phys.*, vol. 36, pp. 3884 – 3894, Dec 1965.

[14] L. D. Edmonds and L. Z. Scheick, "Physical mechanisms of ion-induced stuck bits in the hyundai 16x4 SDRAM," *IEEE Trans. Nucl. Sci.*, vol. 55, pp. 3265–3271, Dec 2008.

[15] S. Kuboyama, A. Maru, H. Shindou, N. Ikeda, T. Hirao, H. Abe, and T. Tamura, "Single-event damages caused by heavy ions observed in AlGaN/GaN hemts," *IEEE Trans. Nucl. Sci.*, vol. 58, pp. 2734–2738, Dec 2011.

[16] E. C. Auden, R. A. Weller, M. H. Mendenhall, R. A. Reed, R. D. Schrimpf, N. C. Hooten, and M. P. King, "Single particle displacement damage in silicon," *IEEE Trans. Nucl. Sci.*, vol. 59, pp. 3054 – 3061, Dec 2012.

[17] J. Frenkel, "On pre-breakdown phenomena in insulators and electronic semiconductors," *Physical Review*, vol. 54, pp. 647–648, 1938.

[18] R. G. Rhodes, *Imperfections and Active Centers in Semiconductors*. The Macmillan Company, 1964.

[19] C. J. Marshall and P. W. Marshall, "Proton effects and test issues for satellite designers: Displacement effects," *1999 NSREC Short Course, Section IVB*, 1999.

[20] G. D. Watkins and J. W. Corbett, "Defects in irradiated silicon: electron paramagnetic resonance and electron-nuclear double resonance of the Si-E center," *Phys. Rev.*, vol. 134, pp. A1359 – A1377, 1964.

[21] A. O. Evwaraye, "Annealing of irradiation induced defects in arsenic doped silicon," *J. Appl. Phys.*, vol. 48, pp. 1840–1844, May 1977.

[22] G. D. Watkins and J. W. Corbett, "Defects in irradiated silicon. I. Electron spin resonance of the Si-A center," *Phys. Rev.*, vol. 121, pp. 1001 – 1014, 1961.

[23] P. W. Marshall, C. J. Dale, E. A. Burke, G. P. Summers, and G. E. Bender, "Proton-induced displacement damage distributions and extremes in silicon microvolumes," *IEEE Trans. Nucl. Sci.*, vol. 37, pp. 1776–1783, Dec 1990.

[24] S. J. Watts, J. Matheson, I. H. Hopkins-Bond, A. Holmes-Siedle, A. Mohammadzadeh, and R. Pace, "A new model for generation-recombination in silicon depletion regions after neutron irradiation," *IEEE Trans. Nucl. Sci.*, vol. 43, pp. 2587 –2594, Dec 1996.

[25] K. Gill, G. Hall, and B. MacEvoy, "Bulk damage effects in irradiated silicon detectors due to clustered divacancies," *J. Appl. Phys.*, vol. 82, pp. 126 – 136, Apr 1997.

[26] J. R. Srour and J. W. Palko, "A framework for understanding displacement damage mechanisms in irradiated silicon devices," *IEEE Trans. Nucl. Sci.*, vol. 53, pp. 3610 – 3620, Dec 2006.

[27] G. Vincent, A. Chantre, and D. Bois, "Electric field effect on the thermal emission of traps in semiconductor junctions," *J. App. Phys.*, vol. 50, pp. 5484–5487, Aug 1979.

[28] P. A. Martin, G. Streetman, and K. Hess, "Electric field enhanced emission from non-coulombic traps in semiconductors," *J. App. Phys.*, vol. 52, pp. 7409–7415, Dec 1981.

[29] W. Shockley and W. T. Read, "Statistics of the recombinations of holes and electrons," *Phys. Rev.*, vol. 87, pp. 835 – 842, 1952.

[30] R. N. Hall, "Electron-hole recombination in germanium," *Phys. Rev.*, vol. 87, pp. 387 – 387, 1952.

[31] D. K. Schroder, "The concept of generation and recombination lifetimes in semiconductors," *IEEE Trans. Electron Devices*, vol. 29, pp. 1336–1338, Aug 1982.

[32] S. R. Messenger, E. A. Burke, G. P. Summers, M. A. Xapsos, R. J. Walters, E. M. Jackson, and B. D. Weaver, "Nonionizing energy (NIEL) for heavy ions," *IEEE Trans. Nucl. Sci.*, vol. 46, pp. 1595 – 1602, Dec 1999.

[33] E. C. Auden, R. A. Weller, R. D. Schrimpf, M. H. Mendenhall, R. A. Reed, N. C. Hooten, , W. G. Bennett, and M. P. King, "Effects of high electric fields on the magnitudes of current steps produced by single particle displacement damage," *IEEE Trans. Nucl. Sci.*, vol. 60, Dec 2013.

[34] R. S. Muller, T. I. Kamins, and M. Chan, *Device Electronics for Integrated Circuits*, 3rd ed. John Wiley and Sons (Asia), 2003.

[35] P. U. Calzolari and S. Graffi, "A theoretical investigation on the generation current in silicon p-n junctions under reverse bias," *Solid State Electronics*, vol. 15, pp. 1003–1011, 1972.

[36] I. Lazanu and S. Lazanu, "The role of primary point defects in the degradation of silicon detectors due to hadron and lepton irradiation," *Physics Scriptica*, vol. 74, pp. 201–207, 2006.

[37] M.-A. Trauwaert, J. Vanhellmont, E. Simoen, C. Claeys, B. Johlander, L. Adams, and P. Clauws, "Study of electrically active lattice defects in ^{252}Cf and proton irradiated silicon diodes," *IEEE Trans. Nucl. Sci.*, vol. 37, pp. 1747 – 1753, Dec 1992.

[38] G. D. Watkins, "Defects in irradiated silicon:EPR and electron-nuclear double resonance of interstitial boon," *Phys. Rev. B*, vol. 12, pp. 5824 – 5839, 1975.

[39] W. Keller, G. Pensl, and M. Schulz, "Experimental study of the Poole-Frenkel effect on the Si:Tl acceptor," *Physica B+C*, vol. 116, pp. 244–251, Feb 1983.

[40] A. S. Grove, *Physics and Technology of Semiconductor Devices*. John Wiley and Sons, Inc., 1967.

[41] C.-T. Sah, R. N. Noyce, and W. Shockley, "Carrier generation and recombination in p-n junctions and p-n junction characteristics," *Proc. of the IRE*, vol. 45, pp. 1228 – 1243, 1957.

[42] P. E. Dodd and L. W. Massengill, "Basic mechanisms and modeling of single-event upset in digital microelectronics," *IEEE Trans. Nucl. Sci.*, vol. 50, pp. 583 – 602, Jun 2003.

[43] Trendsetter, "PAD1:diode JFET LowLeak N-CH TO-72 3L," *http://www.trendsetter.com/product-p/pad1.htm*, Retrieved 21 June 2012.

[44] B. Rogers, "Personal communication," Mar 2013.

[45] D. McMorrow, W. T. Lotshaw, J. S. Melinger, S. Buchner, and R. L. Pease, "Sub-bandgap laser-induced single event effects: Carrier generation via two-photon absorption," *IEEE Trans. Nucl. Sci.*, vol. 49, pp. 3002 –3008, Dec 2002.

[46] P. Horowitz and W. Hill, *The Art of Elecronics*. Cambridge University Press, 1980.

[47] National Semiconductor, "Application note 31: Op amp circuit collection," *http://www.ti.com/lit/an/snla140a/snla140a.pdf*, Retrieved 28 Jan. 2002.

[48] Texas Instruments, "LMC6001," *http://www.ti.com/lit/ds/snos694f/snos694f.pdf*, Nov 2009.

[49] R. A. Pease, "What's all this femtoampere stuff, anyhow?" *Electronic Design*, Sep 1993.

[50] C. Bussolati, A. Fiorentini, and G. Fabri, "Energy for electron-hole pair generation in silicon by electrons and α particles," *Physical Review*, vol. 136, pp. 1756 – 1758, Dec 1964.

[51] B. M. Aleksandrov, M. A. Bak, V. G. Bogdanov, S. S. Bugorkov, L. V. Drapchinskii, Z. I. Solov'eve, and A. V. Sorokina, "On the spontaneous fission half-life of Cf^{252}," *Atomic Energy*, vol. 28, pp. 462 – 463, 1970.

[52] H. W. Schmitt, W. E. Kiker, and C. W. Williams, "Precision measurements of correlated energies and velocities of ^{252}Cf fission fragments," *Physical Review*, vol. 137, pp. 837 – 847, Feb 1965.

[53] A. H. Johnston and B. W. Hughlock, "Latchup in CMOS from single particles," *IEEE Trans. Nucl. Sci.*, vol. 37, pp. 1886 – 1893, Dec 1990.

[54] R. C. Martin, J. B. Knauer, and P. A. Balo, "Production, distribution, and applications of californium-^{252} neutron sources," *Applied Radiation and Isotopes*, vol. 53, pp. 785 – 792, 2000.

[55] J. E. Strain and G. W. Leddicottee, "The preparation, properties, and uses of americium-241 alpha-, gamma- and neutron sources," *ORNL-3335, Oak Ridge National Laboratory*, Aug 1962.

[56] J. R. Srour and O. L. Curtis, Jr., "Short-term annealing in silicon devices following pulsed 14-MeV neutron irradiation," *IEEE Trans. Nucl. Sci.*, vol. 19, pp. 362 – 370, Dec 1972.

[57] S. R. Messenger, E. A. Burke, G. P. Summers, M. A. Xapsos, R. J. Walters, E. M. Jackson, and B. D. Weaver, "Errata to nonionizing energy (NIEL) for heavy ions," *IEEE Trans. Nucl. Sci.*, vol. 50, p. 2494, Dec 2003.

[58] J. Lindhard, V. Nielsen, M. Scharff, and P. Thomsen, "Integral equations governing radiation effects (notes on atomic collisions, iii)," *Mat. Fys. Medd. Dan. Vid. Selsk.*, vol. 33, p. 1, 1963.

[59] R. A. Weller, M. H. Mendenhall, and D. M. Fleetwood, "A screened coulomb scattering module for displacement damage computations in Geant4," *IEEE Trans. Nucl. Sci.*, vol. 51, pp. 3669 – 3678, Dec 2004.

[60] R. A. Weller, M. H. Mendenhall, R. A. Reed, R. D. Schrimpf, K. M. Warren, B. D. Sierawski, and L. W. Massengill, "Monte Carlo simulation of single event effects," *IEEE Trans. Nucl. Sci.*, vol. 57, pp. 1726 – 1746, Aug 2010.

[61] S. Agostinelli, et al., "Geant4a simulation toolkit," *Nucl. Instrum. Methods Phys. Rev. A*, vol. 506, pp. 250 – 303, 2003.

[62] W. W. T. Crane, G. H. Higgens, and H. R. Bowman, "Average number of neutrons per fission for several heavy-element nuclides," *Physical Review*, vol. 101, pp. 1804 – 1805, Mar 1956.

[63] K. M. Warren, R. A. Weller, M. H. Mendenhall, D. A. Reed, Ball, C. L. Howe, B. D. Olson, M. L. Alles, L. W. Massengill, R. D. Schrimpf, N. F. Haddad, S. E. Doyle, D. McMorrow, J. S. Melinger, and W. T. Lotshaw, "The contribution of nuclear reactions to heavy ion single event upset cross-section measurements in a high-density SEU hardened SRAM," *IEEE Trans. Nucl. Sci.*, vol. 52, pp. 2125 – 2131, Dec 2005.

[64] J. W. Corbett and G. D. Watkins, "Production of divacancies and vacancies by electron irradiation of silicon," *Phys. Rev.*, vol. 138, pp. A555–A560, Apr 1965.

[65] J. J. Loferski and P. Rappaport, "Radiation damage in Ge and Si detected by carrier lifetime changes: damage thresholds," *Phys. Rev.*, vol. 111, pp. 432–439, Jul 1958.

[66] T. Diaz de la Rubia and G. H. Gilmer, "Structural transformations and defect production in ion implanted silicon: a molecular dynamics simulation study," *Phys. Rev. Lett.*, vol. 74, pp. 2507–2510, Mar 1995.

[67] M. J. Norgett, M. T. Robinson, and I. M. Torrens, "A proposed method of calculating displacement dose rates," *Nuc. Eng. Des.*, vol. 33, pp. 50–54, 1975.

[68] J. Janesick, T. Elltiott, and F. Pool, "Radiation damage in scientific charge-coupled devices," *IEEE Trans. Nucl. Sci.*, vol. 36, pp. 572–578, Dec 1989.